



**The University of Tennessee
Space Institute**
Tullahoma, Tennessee 37388

FINAL REPORT

for

**AN INNOVATIVE DEMONSTRATION OF
HIGH POWER DENSITY IN A COMPACT
MHD GENERATOR**

CONTRACT NO. DE-AC22-87PC79678

SUBMITTED TO:

**UNITED STATES DEPARTMENT OF ENERGY
PITTSBURGH ENERGY TECHNOLOGY CENTER
P.O. BOX 10940**

PREPARED BY:

**H. J. SCHMIDT
J. T. LINEBERRY
J. N. CHAPMAN**

SUBMITTED BY:

**THE UNIVERSITY OF TENNESSEE SPACE INSTITUTE
TULLAHOMA, TENNESSEE 37388-8897
(615) 455-0631**

DISTRIBUTION STATEMENT A
Approved for public release
Distribution Unlimited

PLEASE RETURN TO:

**BMD TECHNICAL INFORMATION CENTER
BALLISTIC MISSILE DEFENSE ORGANIZATION
7100 DEFENSE PENTAGON
WASHINGTON D.C. 20301-7100**

JUNE 1990

U 4456

19980309 163

Accession Number: 4456

Publication Date: Jun 01, 1990

Title: Innovative Demonstration of High Power Density in a Compact MHD Generator

Personal Author: Schmidt, J.J.; Lineberry, J.T.; Chapman, J.N.

Corporate Author Or Publisher: University of Tennessee Space Institute, Tullahoma, Tennessee 37388-88

Report Prepared for: US Department of Energy, Pittsburgh Energy Technology Center, P.O.Box 10940

Descriptors, Keywords: Fuel Selection Magnet Generator Combustor Oxygen System Faraday Channel Igniter MHD

Pages: 00110

Cataloged Date: Apr 19, 1993

Contract Number: DE-AC22-87PC79678

Document Type: HC

Number of Copies In Library: 000001

Record ID: 26689

FINAL REPORT

for

**AN INNOVATIVE DEMONSTRATION OF
HIGH POWER DENSITY IN A COMPACT
MHD GENERATOR**

CONTRACT NO. DE-AC22-87PC79678

SUBMITTED TO:

**UNITED STATES DEPARTMENT OF ENERGY
PITTSBURGH ENERGY TECHNOLOGY CENTER
P.O. BOX 10940**

PREPARED BY:

**H. J. SCHMIDT
J. T. LINEBERRY
J. N. CHAPMAN**

SUBMITTED BY:

**THE UNIVERSITY OF TENNESSEE SPACE INSTITUTE
TULLAHOMA, TENNESSEE 37388-8897
(615) 455-0631**

JUNE 1990

Table of Contents

1.0	Introduction	1
2.0	Theoretical Background	4
2.1	Fuel Selection	5
2.2	Seed Material Selection	14
2.3	Magnet Constraints	16
2.4	Generator Performance	20
3.0	Component Design	28
3.1	Combustor Design	28
3.2	Oxygen System	34
3.3	Faraday Channel	37
3.4	Diagonal Wall Channel	39
3.5	Load Bank	42
4.0	Test Results	47
4.1	Oxygen System	47
4.2	Igniter Test	57
4.3	Combustor Tests	60
4.3.1	Combustor Test - Run #7	60
4.3.2	Combustor Test - Run #10	65
4.3.3	Combustor Test - Run #20	68
4.3.4	Combustor Test - Run #24	70
4.3.5	Generator Test - Run #28	70
4.3.6	Generator Test - Run #32	75
4.3.7	Generator Test - Run #35	75
4.3.8	Combustion Data	80
4.3.9	Heat Transfer Analysis	89
4.4	Magnet Checkout	91
4.5	Generator Tests	93
4.5.1	Generator Test #24	94
4.5.2	Generator Test #28	96
4.5.3	Generator Test #32	99
4.5.4	Generator Test #35	99
5.0	Conclusions	109
6.0	Recommendations	110
7.0	References	111

List of Tables

I.	Specific Enthalpy for Typical Fuels	7
II.	MHD Generator Design Features and Operating Point	22
III.	Theoretical MHD Generator Performance	23
IV.	Nominal Load Requirements	42
V.	Load Bank Material Properties	44
VI.	Oxygen System Data for all Combustor Tests	54
VII.	Combustor Testing Summary	82
VIII.	Magnet Field Strengths	93
IX.	Summary of Generator Performance	104

List of Figures

1.	Nozzle design nomogram for a three inch diameter exit based on calculations with condensed species removed	10
2.	Nozzle design nomogram for a three inch diameter exit based on calculations with all species considered	13
3.	Plasma conductivity variation with seeding percentage of potassium and cesium at various combustion conditions	15
4.	CFFF 3.2 Tesla magnet bore volume and magnetic field distribution	17
5.	Sketch of magnet with flow train showing accessibility of combustor	19
6.	Effect of generator interaction with operating point - power density, massflow and generator length	21
7.	Calculated plasma and electrical parameter distributions for the nominal 30° DCW generator channel	24
8.	Calculated load and power characteristics for the nominal 30° wall angle DCW generator channel	25
9.	Preliminary assembly drawing of the hybrid combustor	29
10.	Photograph of the redesigned igniter assembly	33
11.	Schematic of the gaseous oxygen system for combustor and generator testing in the CFFF facility	36
12.	Assembly drawing of the Faraday configuration generator channel	38
13.	Photograph of the Faraday channel	40
14.	Assembly drawings of the DCW generator channel	41
15.	Photograph of the completed DCW generator channel	43
16.	Schematic of the load bank design for generator testing	46
17.	Simplified schematic of the oxygen system used through Run #20	48
18.	Typical oxygen system flow data for combustor Run #10	51

19.	Simplified schematic of the oxygen system used	55
20.	Comparison of oxygen line bleed down times before and after the downstream shut off valve was installed	56
21.	Oxygen system performance during a nominal 4.0 second duration run . . .	58
22.	Photograph of igniter prior to free air firing test	59
23.	Photograph of flame pattern during free air test of igniter	59
24.	Photograph of floor mounted combustor configuration for combustor tests #7, 10 and 20	61
25.	Photograph of flow train configured for powered generator channel testing	62
26.	Oxygen feedline pressure during combustor Run #7	64
27.	Oxygen flow rate during combustor Run #7	64
28.	Combustor pressure during combustor Run #7	64
29.	Photograph of the damaged oxygen injection manifold after first firing	66
30.	Photograph showing damage to igniter. View is of the combustor end of the igniter looking outward	66
31.	Photograph of center fuel grain section after first combustor firing	67
32.	Fuel grain sections after Run #20 showing uniformity of wear in grain sections 1 through 4 going from left to right in the photograph	69
33.	Photograph showing insulation damage resulting from pressurizing blow by at the pressure relief port	69
34.	Photograph of combustor burn through at joint between first and second fuel grain sections during Run #24	71
35.	Photograph of fuel grain burn through at the joint with the outer fiberglass casing removed	72
36.	Photograph of the fuel grain with the outer fiberglass casing removed which shows additional voids which did not result in penetration of the casing . . .	72
37.	Photographs of fuel grain longitudinal cracking after combustor test #24 . . .	73

38.	Sketches of various fuel grain joints used	74
39.	Oxygen mass flow rate during extended duration Run #35	77
40.	Combustor pressure during extended duration Run #35. Note use of redundant transducers one of which read only intermittently particularly at the start of the test	77
41.	Photograph of the igniter nozzle after extended duration test #35. The graphite insulating disk is removed in the photograph	78
42.	Photograph of the fuel grain pockets in the first grain section following Run #35	78
43.	Typical combustor pressure data showing event times	81
44.	Combustor external temperatures following a nominal 2.0 second run	85
45.	Combustor external temperatures following the extended duration Run #35	86
46.	Photograph showing sharply peaked fuel grain spokes following Run #35 ..	87
47.	Nozzle soak temperatures following a firing (test Run #10)	88
48.	Comparison of measured with theoretical temperature transients at the nozzle exit location	90
49.	Calibration of the CFFF magnet giving field strength as a function of excitation current	92
50.	Measurement of the Faraday channel impedance during generator test #24	95
51.	Power characteristics of the Faraday generator channel during generator test #28	97-98
52.	Power characteristics of the DCW generator channel during generator test #32	100
53.	Power characteristics of the DCW generator channel during extended duration Run #35	101
54.	Run #35 current histogram	103
55.	Run #35 voltage histogram	103

56.	Run #35 power histogram	103
57.	Run #35 load resistance histogram	103
58.	Theoretical effect of excess fuel consumption on plasma conductivity	105
59.	Faraday channel outer surface temperatures following a nominal 1.5 second firing	107
60.	DCW generator channel outer surface temperatures following a nominal 4.0 second firing	108

1.0 INTRODUCTION

Magnetohydrodynamic (MHD) energy conversion is a candidate technology for satisfying the pulse power requirements for advanced weapon and discrimination systems for the Strategic Defense Initiative. However, to be competitive with alternative pulse power concepts utilizing nuclear or stored energy schemes the characteristic power per unit weight and volume of the MHD system requires improvement in performance well beyond the levels demonstrated in the past.

In this regard, there are two primary performance parameters of concern: the power density and the specific energy. The power density is the ratio of the electrical energy output to the internal volume of the generator channel. The MHD process is a volumetric process and the power density is therefore a direct measure of the compactness of the system. As such, it controls the size and weight of a MHD power generating system for a given power output. The greater the characteristic power density, the smaller and lighter the channel, magnet, combustor and flow train will be. The second parameter, the specific energy, is the ratio of the electrical energy output to consumable energy used for its production. In the case of a chemically driven MHD system, the specific energy is a direct measure of the conversion efficiency from the latent chemical energy to electrical energy. In pulse power MHD systems with short operating durations the specific energy is the controlling parameter for the weight and volume of the stored reactants used to power the system. The two parameters are conceptually interrelated, and for a given mission scenario maximization of both, in general, are required for optimization of the system. However, for short operating durations the power density is the dominant parameter; whereas, for long durations, the specific energy is the dominant parameter.

The present program was conducted by The University of Tennessee Space Institute (UTSI). It was by its nature a high risk experimental program to demonstrate the feasibility of high power density operation in a laboratory scale combustion driven MHD generator. Maximization of specific energy was not a consideration for the present program, but the results have implications in this regard by virtue of high energy fuel used.

To achieve high power density and implied commensurate low system volume and weight, it was necessary to use an energetic fuel. This was even more crucial in the program described for two reasons. First, losses in an MHD generator scale with the area of the device while power scales with the volume. Since volume increases faster than area, large generators tend to be more thermally efficient than their equivalent smaller counterparts. In a laboratory scale device the use of a high energy fuel can partially compensate for the higher anticipated losses. Secondly, the experimental phase of the present program was limited to using an existing moderate field strength magnet with a nominal field strength of 3.2 Tesla. To a first order, the power density is proportional to the product of plasma electrical conductivity with the square of the applied magnetic field strength. To compensate for the moderate field strength a highly energetic fuel, that is, one with a high heat release during combustion, was required to provide a high plasma temperature and, in turn, a high plasma electrical conductivity.

For the present program the high energy fuel of choice was a mixture of powdered aluminum and carbon seeded with potassium carbonate and burned with gaseous oxygen. The solid fuel was burned in a hybrid combustion scheme wherein the fuel was cast within a cylindrical combustor in analogy with a solid propellant rocket motor. The inherent simplicity of the solid rocket motor with regard to thermal protection, shelf life, safety, etc. are retained in the hybrid combustor. However, in contrast to the rocket motor, by externally supplying the oxygen in the hybrid combustor, the combustor is stoppable and restartable. Using the selected fuel imposed considerable technical risk to the project. Not only is there a paucity of information, knowledge, or experience in the combustion of the fuel-oxidizer combination, but no practical precedent for its use in the hybrid combustor existed before the present program. These risks, considerable as they were with an unproven combustion scheme, were balanced by minimizing the cost of the flow train components and overall experiment. The flow train components were designed for short duration testing using heat sinking design concepts with unconventional construction techniques. Indeed, a subordinate element of the program was to demonstrate that minimal cost "throw away" components are a viable alternative to more expensive, disassemblable components designed with active thermal management. In the program cost management, effort was expended to utilize to the extent possible existing

facility utilities, hardware, instrumentation and equipment. This additionally required designing the experiment to be compatible with an existing magnet which in turn resulted in the combustor itself being partially within magnet bore. This in turn was another area of technical risk as adherence to conventional design standards would suggest that only the active region of the generator channel should be in the magnet bore.

Finally, cost considerations in conjunction with virtually all of the experiment being located within the magnetic field limited the experimental instrumentation complement. The instrumentation was limited first to that necessary for safety of operation and second to the minimal amount commensurate with the goal. Thus experimental data is limited to gross channel output current and voltage, magnetic field strength, fuel and oxidizer flow rates, flow train external temperatures and combustor pressure. The measured quantities were sufficient to verify power produced and safe operation but were insufficient to provide details such as voltage and current distributions or voltage drops within the generator channel. Similarly, while instantaneous oxidizer flow rates were measured, only average fuel consumption based on pre and post test component weights and dimensions was possible.

The program comprised a nominal two year effort which is summarized in the following sections of this final report. In Section 2.0, the theoretical background including the fuel and seed selection are presented and discussed in further detail. In Section 3.0, the constraints and experiment design are considered along with detailed descriptions of the hardware including the flow train, load bank and oxygen system. Test results obtained on the oxygen system alone, as well as on the entire flow train during hot firings in both power producing and non-power producing tests, are presented and discussed in Section 4.0 Finally in Section 5.0 the conclusions and findings from the program are presented and discussed.

2.0 THEORETICAL BACKGROUND

The completed program was guided by several criteria which were sought to be satisfied during all phases from conceptual design through final testing. In summary, these criteria were:

- Maximize MHD power density,**
- Minimize combustion pressure,**
- Maintain simplified mechanical design,**
- Maximize system integrity/reliability,**
- Minimize fabrication and operating costs,**
- and, Maximize to the extent possible the utilization of
existing equipment.**

The first item is simply a statement of the program objective. Note that it did not imply power maximization, but rather maximization of power per unit volume. In keeping with this objective, emphasis was placed in achieving high power in a small generator with little regard being paid to optimizing the generator for total power or fullness of utilization of the available magnetic field.

The remaining five items in the above list of criteria are all related to minimizing the cost. To meet these criteria the conceptual design of a hybrid combustor and a heat sinked flow train was developed. The hybrid combustor is comprised of a fuel grain cast within the combustor with a gaseous oxygen oxidizer supplied externally to the combustor. Advantages of the design are its inherent simplicity, in that no fuel metering or control is necessary, it is stoppable and restartable, and the fuel grain itself serves as a thermal shield. Disadvantages are that run time is limited and with no known prior experience with this fuel in this type of combustion system, initial risks were involved. The burning characteristics were initially unknown, even its physical characteristics, such as its cast density and the relation of casting density to burning rate, were only crudely estimable at the outset. In fact, the program results provide information on some of the unknown fuel characteristics. Simplicity of the design was of high priority and some of the features adopted to maintain simplicity are:

- A reusable combustor which can be repacked with fuel for multiple firings.
- A nozzle designed with an outer structural shell and interchangeable, variable internal graphite inserts for multiple testing and variable operation.
- Two-terminal generator configurations to minimize the complexity of the electrical network.
- Utilization of graphite material for plasma exposed internal surfaces (electrodes and nozzle) to provide heat sinking and ablative shielding.
- Simple internal flow lofting, i.e., a circular flow cross-section and straight internal walls.
- Use of a common diffuser and downstream quench system with disregard to optimization of diffuser performance.
- Minimization of instrumentation, i.e., measurement of only parameters required to monitor global performance and insure safety.

2.1 Fuel Selection

The power density in an MHD generator is the electrical power output per unit of internal volume of the generator. As such, it is a fundamental parameter which governs the aggregate MHD system size and weight for a given power output level. The maximization of the power density, which is the goal of the present effort, is therefore a first step in the evolution of compact high power MHD power systems.

To a first order, the maximum Faraday power density in an MHD generator is proportional to the product of the plasma conductivity with the squares of the plasma velocity and imposed magnetic field strength. That is

$$\text{power density} \sim \sigma u^2 B^2 \quad (1)$$

where σ is the conductivity, u is the plasma velocity and B is the field strength. In this proportionality, it is convenient to further subdivide the expression into the terms B^2 and

the product $\frac{\sigma u^2}{4}$ where the latter is termed the power density parameter. The power density parameter, which can also be thought of as the power density for a field of 1 Tesla, is a plasma characteristic. In general, not only does it vary with the chemical composition of the plasma but also with the thermodynamic state of a given composition. In particular, the power density parameter is a function of the plasma temperature and exhibits an optimal value. The plasma conductivity is an exponentially increasing function with temperature while plasma velocity is a decreasing square root function with temperature. The fuel selection for high power density involves two considerations. First, the fuel must be energetic to produce high temperatures and plasma conductivity; and second, when expanded from the combustor state, the plasma should maintain a high value of the power density parameter.

The heat release of a selection of possible fuels is given in Table I. Absent from the table are cyanogen, a liquid, and tetracyanoethylene, a solid which are also energetic fuels which have been used in previous high energy MHD investigations. These were never considered primarily since their inherent toxicity would incur exorbitant costs with the special handling required. Except for the aviation kerosene all the fuels in Table I are solids. The first three fuels are actually explosives. Nitrocellulose and nitroglycerine form the basis for double base solid propellant rockets. Note that the heat of combustion of these explosives is of the same order of magnitude as the other fuels listed. It is the rate of combustion which distinguishes explosives from the other fuel combinations rather than the heat release.

All of the carbon based combinations, carbon, coke and coal in order of increasing hydrogen content have similar heats of combustion in the range from 8 to 9 MJ/kg. Aluminum has approximately twice the value of carbon. Aluminum in an oxygen combustion system has the disadvantage that some of its oxides are in condensed phases. For an MHD system the plasma requires gas phase products of combustion. To use all aluminum in a practical application would require an oxidizer such as nitrogen tetroxide, a liquid, which would liberate gaseous nitrogen as a product of combustion in addition to the condensed solids.

To get the high performance required the present program was predicated on using a mixture of carbon and aluminum burned in oxygen as the fuel of choice. In this case

the plasma gaseous products of combustion are derived from the carbon fuel. The heat of combustion, however, is weighted according to the relative magnitude of the carbon and aluminum density. In a loose analogy the combustion of a 50% aluminized carbon fuel can be thought of as a combustion of carbon with a 50% increase in the heat release.

TABLE I. SPECIFIC ENTHALPY FOR TYPICAL FUELS

	FUEL/OXIDIZER	STOICHIOMETRY	HEAT OF COMBUSTION (MJ/KG)
Solid Fuels	Nitrocellulose		10.60
	Nitroglycerine		6.30
	Octol		5.30
Liquid Fuel	JP4/O2	1.0	10.83
Powdered Fuels	Coal/O2	1.0	9.07
		0.9	8.84
		0.8	8.59
	Coke/O2	1.0	8.01
	C/O2	1.0	8.93
		0.9	8.67
		0.8	8.36
	Al/O2	1.0	16.32
Combined Powdered Fuel	C, Al (50%)/O2	1.0	12.63

The aluminum oxides will be in condensed phases at the pressures and temperatures of interest and will not significantly contribute to the plasma collision processes upon

which the plasma conductivity and MHD interaction are based. The carbon portion of the fuel will yield gaseous species CO and CO₂ which will comprise the major volumetric components of the plasma. The plasma requires seeding with an easily ionized alkali salt to provide high conductivity. The absence of hydrogen in the plasma products is also conducive to high plasma conductivity since water has a high collision cross-section and the negative hydroxyl ion can deplete free electrons from the plasma.

While attractive from theoretical considerations, there is little known experimental data or practical experience in using this fuel combination. The only known application of the aluminum-carbon-oxygen plasma generation system in a high performance MHD system has been in the Soviet Union^{1,2}. The Soviet investigators used a conventional combustor in which the seeded aluminum-carbon fuel was injected as a powder. For the present work, a hybrid combustion system in which fuel is cast in a grain within the combustor was used on the basis of the simplicity and absence of a solid seeding system. Such a system has many of the simplicities of a solid propellant rocket engine. However, by introducing the oxidizer separately, gaseous oxygen in this case, the ability to stop and restart is possible and as such this system is inherently safe and simple. In addition, the fuel grain also serves as a thermal shield as it is consumed allowing for a simple thermal control system.

Calculations were performed to assess the suitability of the selected fuel for the MHD applications. These calculations considered: relative aluminum to carbon content, seed weight percentage and type, combustor pressure, stoichiometry, and binder content. Results and discussions of these calculations are fully described in the semi-annual report³ and for brevity are only summarized here. The calculations showed that plasma conductivity monotonically increases with increasing aluminum content up to the 50 percent maximum content considered and it decreases with increasing combustion pressure. The calculations also showed that the plasma conductivity also increased with equivalence ratio and seed rate and attained maximum conductivity at values of the equivalence ratio and potassium seeding percentage of approximately 1.5 and 5% by weight respectively. For higher values of equivalence ratio or seeding rate the plasma conductivity would correspondingly be reduced from the maximum value. The calculations also showed that binder content, which can be up to 20% of the fuel composition by weight, must also be taken into account.

As previously pointed out the conductivity in the combustor while serving as a figure of merit is subordinated to the power density parameter in the generator. The potential to produce electrical power in the expanded plasma states is of primary importance. During the expansion, the plasma temperature and pressure drop while its velocity increases. While the plasma conductivity increases with decreasing pressure at constant temperature, the temperature dependence is strong and dominant so that the conductivity in general decreases as the plasma expands.

The evolution of the power density parameter during the expansion process through the nozzle can conveniently be described on a nomograph as depicted in Figure 1. The figure is actually a nozzle design nomograph and contains a considerable condensation of information which requires detailed explanation. The figure is a depiction of nozzle expansion processes for a predetermined and constant nozzle exit area (i.e. generator entrance area) and variable throat area. (For the present experimental system, the dimensional constraints of an existing magnet bore effectively imposes a constraint on the maximum internal diameter of a generator which is three (3) inches.) Figure 1 is therefore, based on a fixed nozzle exit area diameter of three (3) inches. Consider first, the dotted lines in Figure 1. These are combustion pressure isolines which provide a graphical solution for the mass flow rate (ordinate) as a function of the nozzle throat diameter (abscissa). Thus, for a given throat size the mass flow rate as a function of combustor pressure is readily determined. Conversely, for a constant mass flow rate the functional relation between the combustion pressure and throat size is similarly depicted.

Since the plot is based on a fixed nozzle exit area, the variable throat implies a variable area ratio or equivalently an expansion to a variable flow Mach number at the nozzle exit. The resulting nozzle exit Mach number (generator inlet Mach number) is given by the scale at the top of the figure. Thus, when the throat diameter is three (3) inches (the same as the exit diameter) the flow Mach number is one (1); and as the throat diameter diminishes the exit Mach number (and area ratio) increases accordingly. The Mach number relation depends on the plasma specific heat ratio which may have a slight pressure dependence during expansion as a consequence of thermochemical species variations. The Mach number scale is correct for a combustion pressure of 50 atm. but will be approximately correct for all other cases depicted.

Figure 1 presents not only the mass flow relation for the nozzle but by virtue of the

MHD Generator Entrance Map

Combustion of Al:C (1:1) with Binder, K_2CO_3 (5% K) in Gaseous O_2

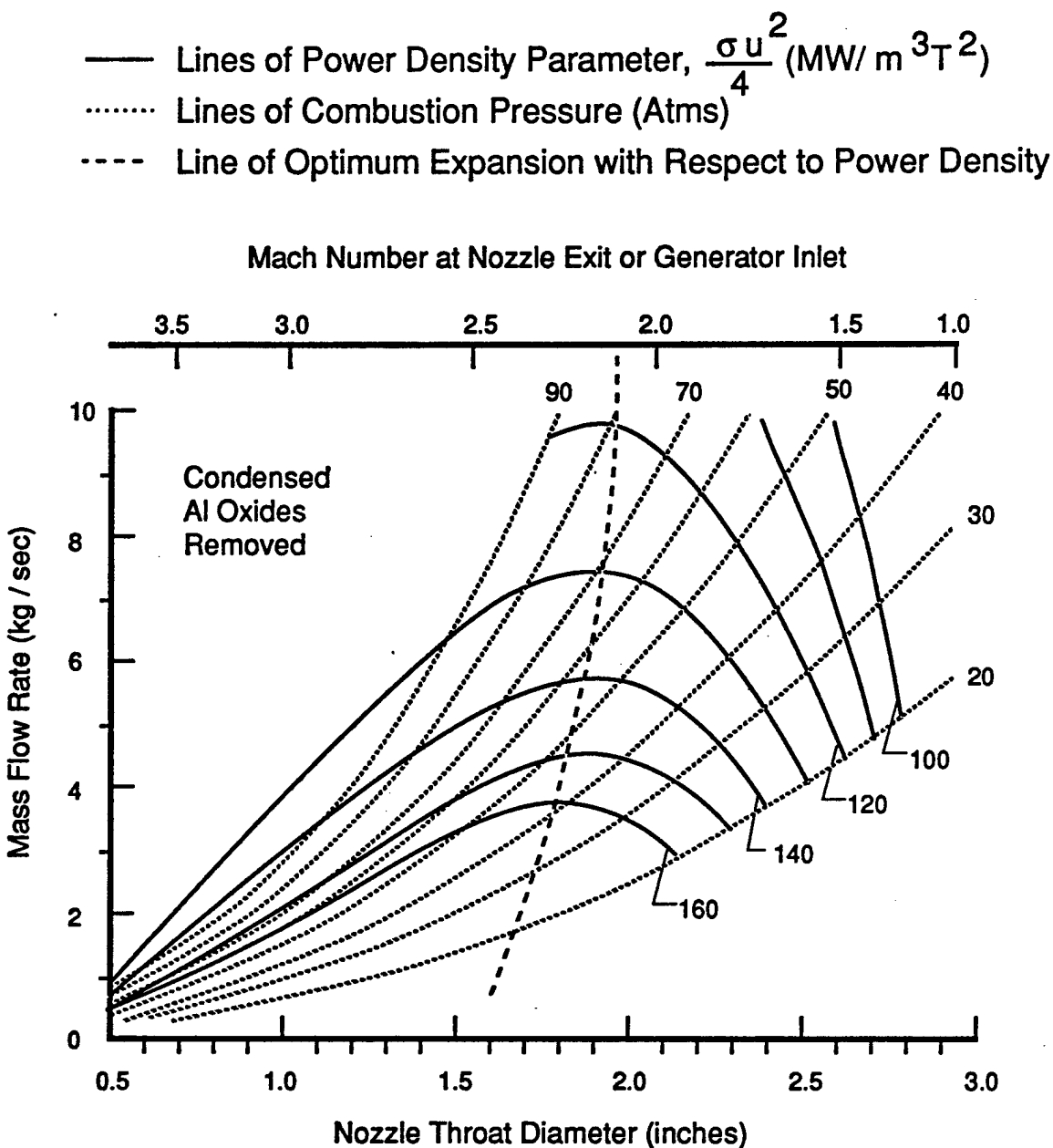


Figure 1. Nozzle Design Nomogram for a Three (3) Inch Diameter Exit Based on Calculations with all Condensed Species Removed.

fixed exit area, also infers an exit thermodynamic state for each combination of throat size, mass flow, and combustion pressure. Since the power density parameter is derivable from the plasma state variables, it can also be plotted on the figure. The solid lines in Figure 1 are isolines of the power density parameter and as indicated they are convex downward and exhibit peak or optimal values. As an illustration, consider a hypothetical case of a constant mass flow of 4 kg/sec. In Figure 1, the power density parameter value of 140 results at a combustor pressure of 90 atm with a 1.2 inch diameter throat and at a pressure of 22 atm with a 2.3 inch diameter throat. The maximum value of 150 MW/m³ occurs at a pressure of approximately 45 atm, and a throat diameter of approximately 1.75 inches which is the peak of the 150 MW/m³ power density parameter isoline. This illustrates the optimization of the expansion process with regard to the power density. The optimal points lie on the peaks of the power density isolines, and the focus of these peaks is superimposed as a broken line in Figure 1. To the left of the optimal line the velocity squared term increases faster than the conductivity decreases as the maximum power density value is approached. The converse behavior occurs to the right of the optimal line. From this figure, it can be concluded as a generality that irrespective of the mass flow or combustion pressure, and optimal generator entrance Mach number should be in the range 2.25 to 2.5 for this fuel combination.

In addition, one can also infer the effects of expected nozzle throat erosion from the figure. Under the assumption that the fuel surface recession rate is independent of combustion pressure, the mass flow will remain constant. However, erosion at the nozzle throat will increase its effective diameter and result in a lowering of the combustor pressure. If the initial design point for the nozzle is to the left of the focus of peak values, the power density should increase as the throat enlarges or if it were at or to the right of the optimal, the power density should decrease as the throat enlarges.

Figure 1 is not a universal nomogram in that it is predicated on a particular combustion system of a particular seeding rate subject to ideal computational assumptions. First, let us consider the conductivity model. Figure 1 is based on a 5% by weight potassium seed. Other seed percentages or cesium could be expected to change the plasma conductivity. As a crude estimate, such a perturbation can be taken to be uniform in that the values of power density parameter would change, but the form of the relations

depicted in Figure 1 would not drastically change.

The conductivity of plasma containing aluminum species itself is not well understood. At high pressure and high temperatures significant fractions of AlO_2 and AlO -ions which deplete the free electron concentration can be present. A proper accounting for these effects is uncertain, particularly in the case of the AlO ion. Crawford and Lineberry⁴ have indicated that up to a 50% reduction in conductivity can result by inclusion of this ion in comparison to its neglect in Al:C combustion schemes. The widely used JANAF tables for electrophysical property data of chemical species are inconsistent with regard to AlO . With a lack of consistent data and more significantly, a lack of experimental confirmation of the physical effects or presence of significant AlO ion formation, all calculations performed did not consider any possible effects of the AlO ionic species on the electrical transport properties. As such, the calculations may be regarded as optimistic in this regard.

A second important aspect of the Al:C fuel is the treatment of the aluminum oxides in the expansion and MHD processes. The principal oxide Al_2O_3 will be in a condensed state at the pressures and temperatures of interest in the nozzle and generator. The calculations are based on the NASA 273 thermochemical equilibrium code. In equilibrium calculations, the underlying assumption is that the latent heat of condensation is available to the gaseous species present during the expansion process. In the present case where residence times are short, this may not be valid. The results presented in Figure 1 have been modified in that condensed species have been eliminated from the expansion. That is, the combustor flame temperature was calculated with all species present. Only the gaseous species, however, were considered during the expansion process.

In contrast, the nozzle design nomogram for calculations including the condensed species is given in Figure 2 for the same fuel composition as in Figure 1. In comparing the figures, the inclusion of the condensed species results in markedly increased values for the power density parameter. The two figures represent extremes insofar as the modeling is concerned, and Figure 2 is the more conservative case upon which the design calculations should more appropriately be based.

MHD Generator Entrance Map

Combustion of Al:C (1:1) with Binder, K_2CO_3 (5% K) in Gaseous O_2

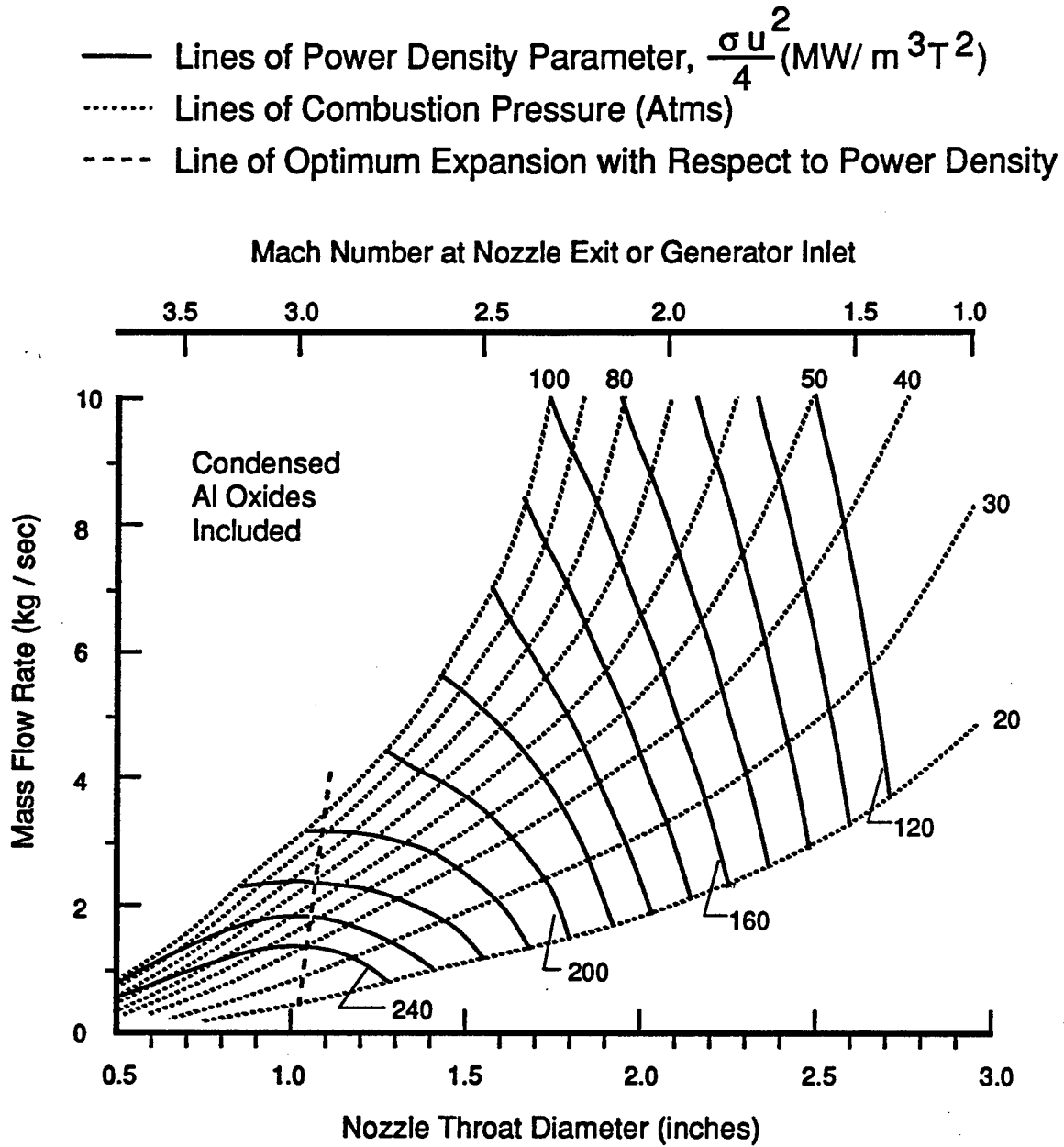


Figure 2. Nozzle Design Nomogram for a Three (3) Inch Diameter Exit Based on Calculations with all Species Considered.

2.2 Seed Material Selection

With regard to the seed material, cesium by virtue of its lower ionization potential would result in higher plasma conductivity than potassium on a molecule for molecule basis. Figure 3 presents calculated plasma conductivity at the combustor conditions for potassium and cesium carbonate seed materials for various weight percentages of seeding. As indicated in the figure, higher theoretical conductivity levels result with the cesium. On the weight basis, the conductivity maximizes for 12% and 5% for the cesium and potassium respectively. However, note that since the molecular weight of the cesium carbonate is 2.35 times that of potassium carbonate the maximum conductivity occurs at approximately the same molar fraction. Cesium is considerably more expensive than potassium partially due to its lower abundance in nature. Therefore, potassium was selected for the present investigation as it is more readily available and would be the more practical choice in a widespread use. Clearly cesium would be of utility in maximizing conductivity, and it may be beneficial to do so in an extension to the present or similar program. For example, in the present program a nominal 3.2 Tesla magnet was used. From the previous discussion, the power density will vary as the product of the conductivity and the square of the field strength. Thus, as a crude estimate one could expect the power density with a 14% cesium seed percentage of a 3.2T field to be equivalent to that of a 5% potassium seed level with a 3.7T field. In a practical device it again may be more beneficial to increase the field rather than the striving for the maximum conductivity. The point is, that with the choice of a highly energetic fuel, sufficient conductivity results for a practical application with the more available and cheaper potassium seed. The present investigation should therefore not be looked on as a maximum effort to achieve a high power density by maximizing the plasma conductivity. Rather, it should be more appropriately viewed as using a "low quality" seed with an energetic fuel as contrasted with using a "high quality" seed with a less energetic fuel. On the basis of the calculated results, a nominal fuel composition was selected as a 50% mixture by weight of aluminum with carbon, with up to 20% by weight epoxy binder and seeded with 5% by weight potassium in the form of potassium carbonate. The desired stoichiometry of combustion was 0.77 (equivalence ratio = 1.30).

- ① $P_{comb} = 20$ Atms, Al:C (1 :1), 13% Binder, Heat Loss = 5% Qth
- ② $P_{comb} = 50$ Atms, Al:C (1:1), 20% Binder, Adiabatic Flame

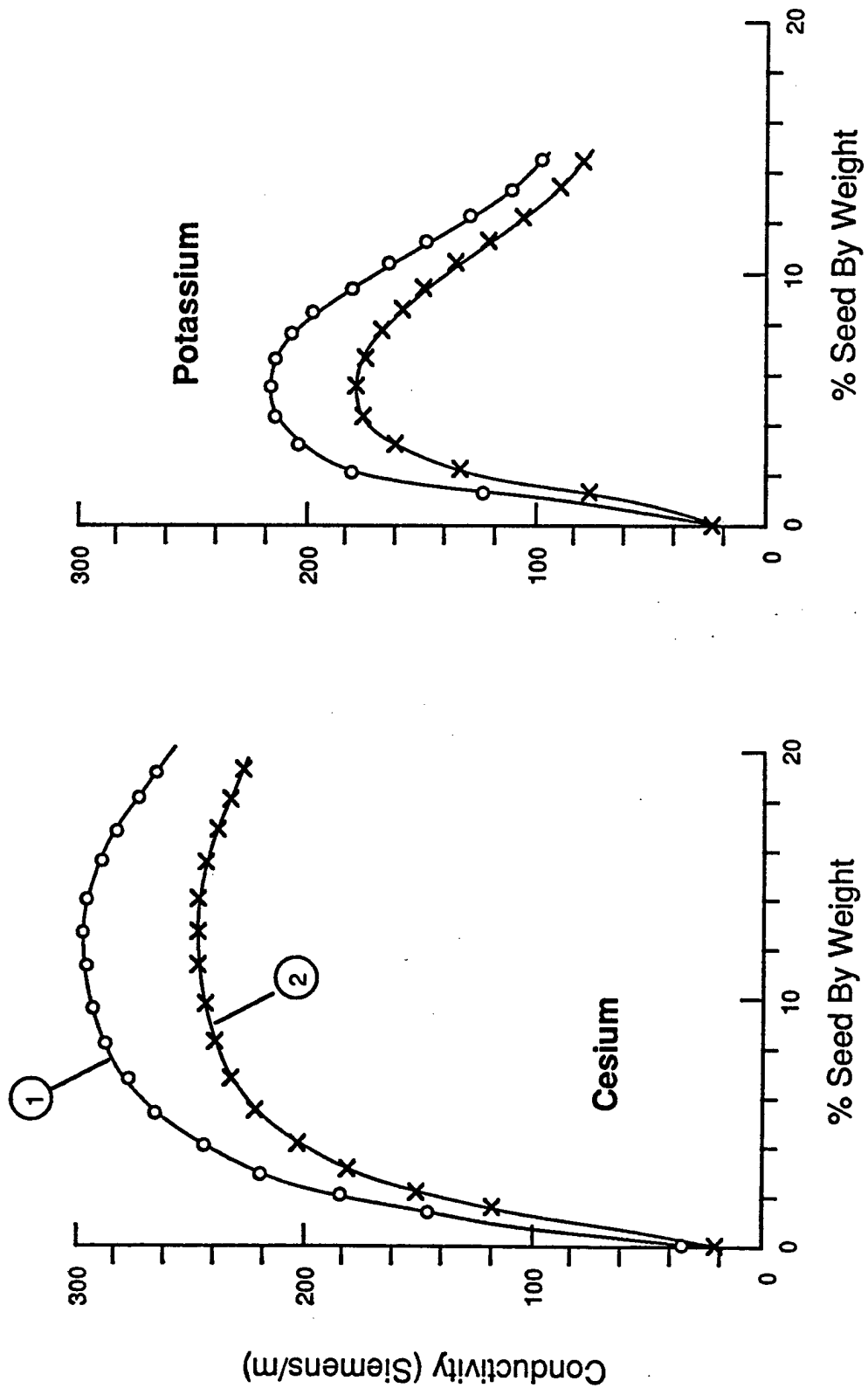


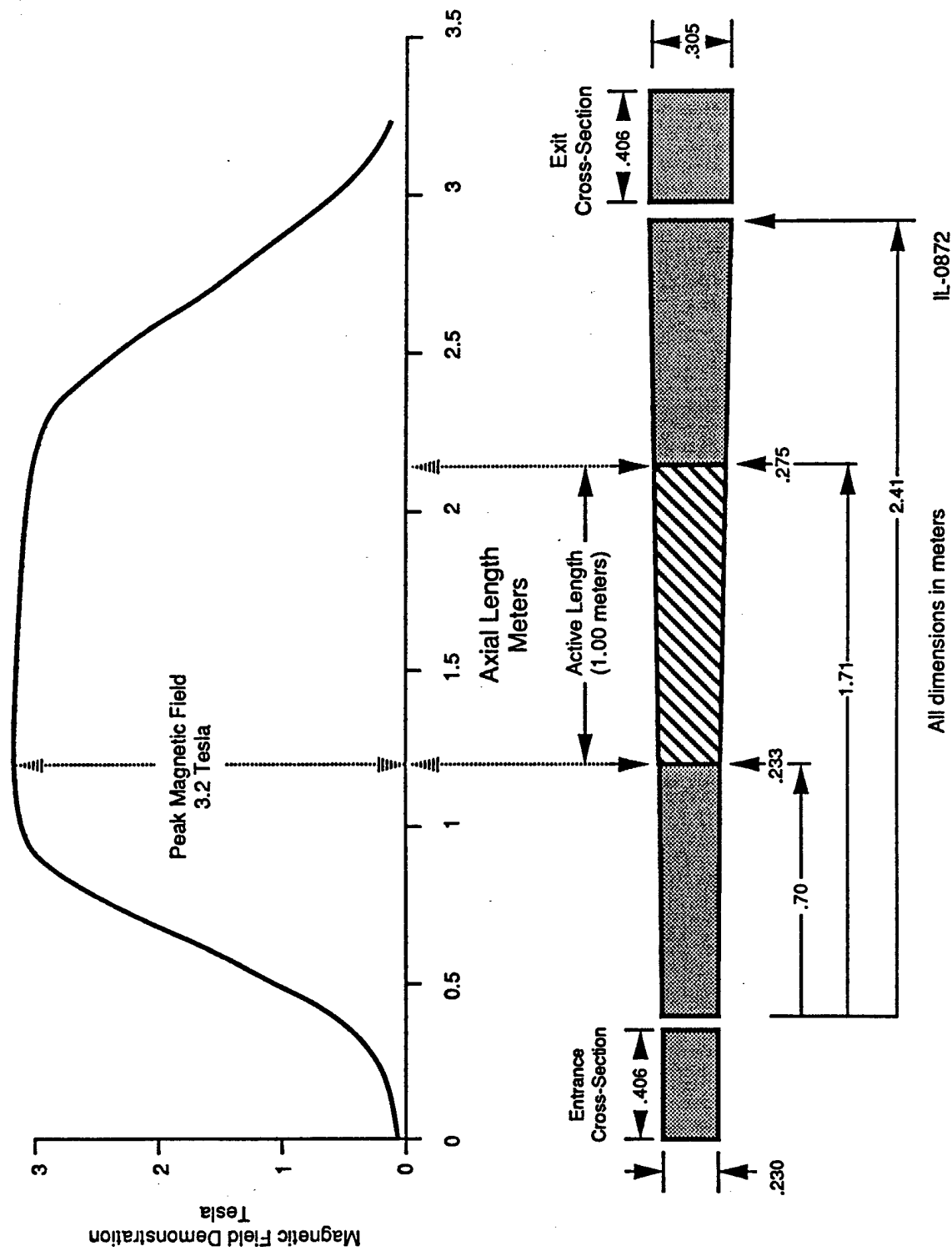
Figure 3. Plasma Conductivity Variation with Seeding Percentage of Potassium and Cesium at Various Combustion Conditions

2.3 Magnet Constraints

While the fuel selection and plasma calculations could be divorced to a large extent from the details of the experiment, it was necessary to size the experiment before detailed calculations for the MHD generator channel could be performed. In this regard, the cost savings predicated on using an existing magnet imposed geometric and dimensional constraints on the hardware which required accommodation from the onset. This is in marked contrast to conventional MHD design practice. In a conventional design sequence, the guiding criteria for the generator channel are couched in terms of plasma mass flow and electrical conductivity available as well as power output sought. Subsequent for the final channel configuration, the magnet is constructed to match the required field strength and interaction length. In the present experiment the procedure was to accommodate a high interaction generator channel within an existing magnetic field envelope more suitable for a low interaction channel.

Figure 4 shows the magnetic field distribution and bore dimensions for the existing Coal Fired Flow Facility (CFFF) magnet at UTSI which was available for the experiment. The magnet bore is 2.4 meters in length and has a rectangular cross-section. The magnet bore diverges in the horizontal plane (B field direction) from 23 cm at the entrance to 30.5 cm at the exit. The vertical bore dimension is constant at 40.6 cm.

The nominal magnetic field distribution peaks at 3.2 Tesla and is relatively flat for only a distance approximately 1 to 1.5 meters. In order to maximize power density, which is proportional to the square of the field strength, it is desirable to have a uniform high strength field. A region approximately one (1) meter in length, shown in Figure 4, was suitable for the experiment. The generator must be able to fit within this volume. Maximum utilization of this volume would be afforded by a generator with a rectangular cross-section similar to the MHD generator channels previously tested in this magnet. On the other hand, rectangular channels are relatively expensive in comparison to cylindrical channels. In addition, high pressure combustors in general are universally constructed with a cylindrical geometry from considerations of structural integrity and thermal efficiency. Mating a cylindrical combustor to a rectangular channel would require a nozzle which, in the case of a supersonic exit velocity, accomplishes the cross-sectional shape transition upstream of the throat in the subsonic flow region. Such nozzles are



IL-0872

All dimensions in meters

Figure 4. CFFF 3.2 Tesla Magnet Bore Volume and Magnetic Field Distribution

costly, difficult to fabricate and can promote corner interference and subsequent flow nonuniformity. By selecting a circular geometry for the combustor and channel, a simplified system resulted. In this case, the cost for this simplicity was that the maximum outside diameter of the channel had to be less than the smaller bore dimension or approximately nine (9) inches. The nominal outer diameter of the generator was taken to be eight (8) inches which permitted a 1/2 inch thick glass laminate thermal protective shield to separate the channel from the magnet structure. The thermal shield was necessary to protect the magnet in the event of a plasma leak in the flow train either at a gasketed flange or wall failure. After accounting for the component flange connection, pressure vessel wall thickness and internal heat shield thickness, the useable internal channel diameter was nominally taken to be three (3) inches.

To minimize thermal losses from the plasma, it is also desirable to have the combustor close coupled to the generator channel with a short nozzle. The same geometric constraints therefore apply to the portion of the combustor-nozzle combination which is located in the shaded region upstream of the useable active length depicted in Figure 4.

The combustor and nozzle operate in a significant magnetic field strength environment. This again was contrary to conventional design practice, since the MHD interaction is also present in these components. That is, they are in essence analogous to a short circuited MHD generator, and the plasma contains parasitic eddy currents induced by the fringe field. The effect of these eddy currents is to impose a pressure drop and Joule heating on the plasma. In the combustor where the velocity is low, the losses are low in accordance with the power density being functionally dependent upon the square of the plasma velocity. However, since the nozzle is designed to produce an optimal power density parameter at its exit, the losses also peak here. Thus, these considerations provided an electrodynamic basis for the necessity of a short nozzle and close coupling the combustor to the generator as well.

From a volumetric and accessibility stand point, the geometric constraints of the magnet on the combustor are less severe than in the case of the channel. The magnet is an iron core saddle coil configuration. The geometry shown in Figure 5 is appropriate for the bore within the iron pole pieces. Outside of the iron return frame, the saddle coil

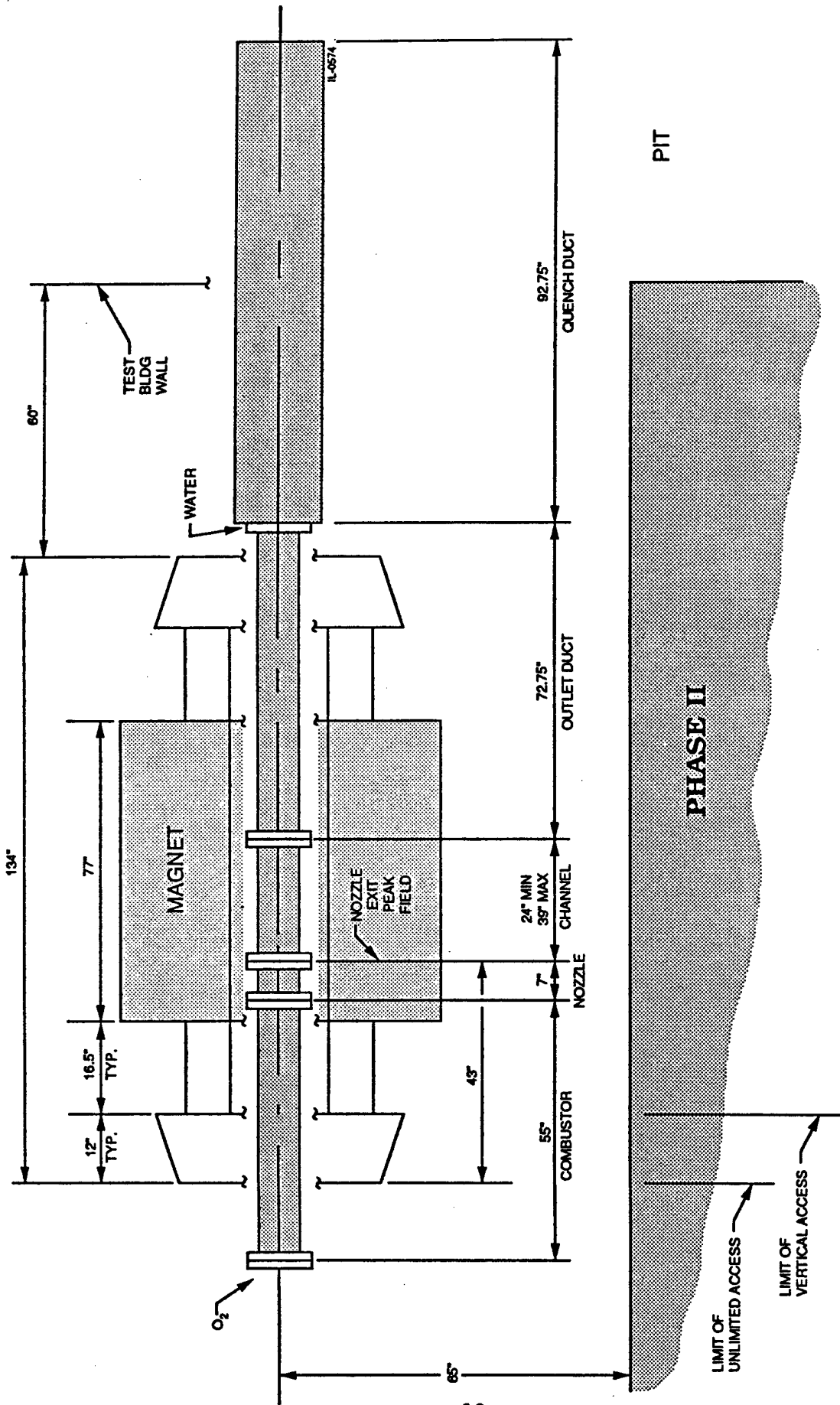


Figure 5. Sketch of Magnet with Flow Train Showing Accessibility of Combustor

crossover limits vertical and horizontal accessibility as shown in Figure 5. The coil force containment members restrict horizontal accessibility but not vertical accessibility. There is unlimited accessibility beyond the force containment members.

2.4 Generator Performance

Detailed parametric studies of generator performance were performed as a significant part of experiment design and were reported fully in a semi-annual report³.

These studies considered parametric variations of combustor pressure, inlet Mach number, and electrode diagonalization angle. A summary of the findings of these parametric studies are:

1. Combustion pressure strongly influences generator length which increases with increasing combustor pressure. The mean level of power density achievable for a given generator design is only mildly sensitive to the combustor pressure. This is shown in Figure 6. However, the MHD interaction is a strong function of the combustor pressure and it is for this reason that generator length increases with increasing pressure.
2. The generator inlet Mach number has a strong influence upon the power density level that can be achieved.
3. In a two terminal diagonal conducting wall configuration (DCW) optimal performance is obtained for shallow wall angles on the order of 30°.

Based on these studies the nominal operating point was selected to be that of a combustor pressure of 40 atmospheres and a channel inlet Mach number of 2.5. Other conditions of interest are summarized in Table II for the nominal operating point. As indicated in Table II the desired combustion stoichiometry is 0.77 (fuel rich). This is made on the basis of maximizing the power density, but is pertinent for heat sink design as well. The fuel rich combustion implies that the plasma will be depleted in oxygen or oxidizing chemical species. This in turn would suggest that graphite can be used as a flow train

Bfield = 3.2 Tesla
Inlet Mach Number = 2.5
Wall Angle = 30 deg
Inlet Diameter = 3.0 in

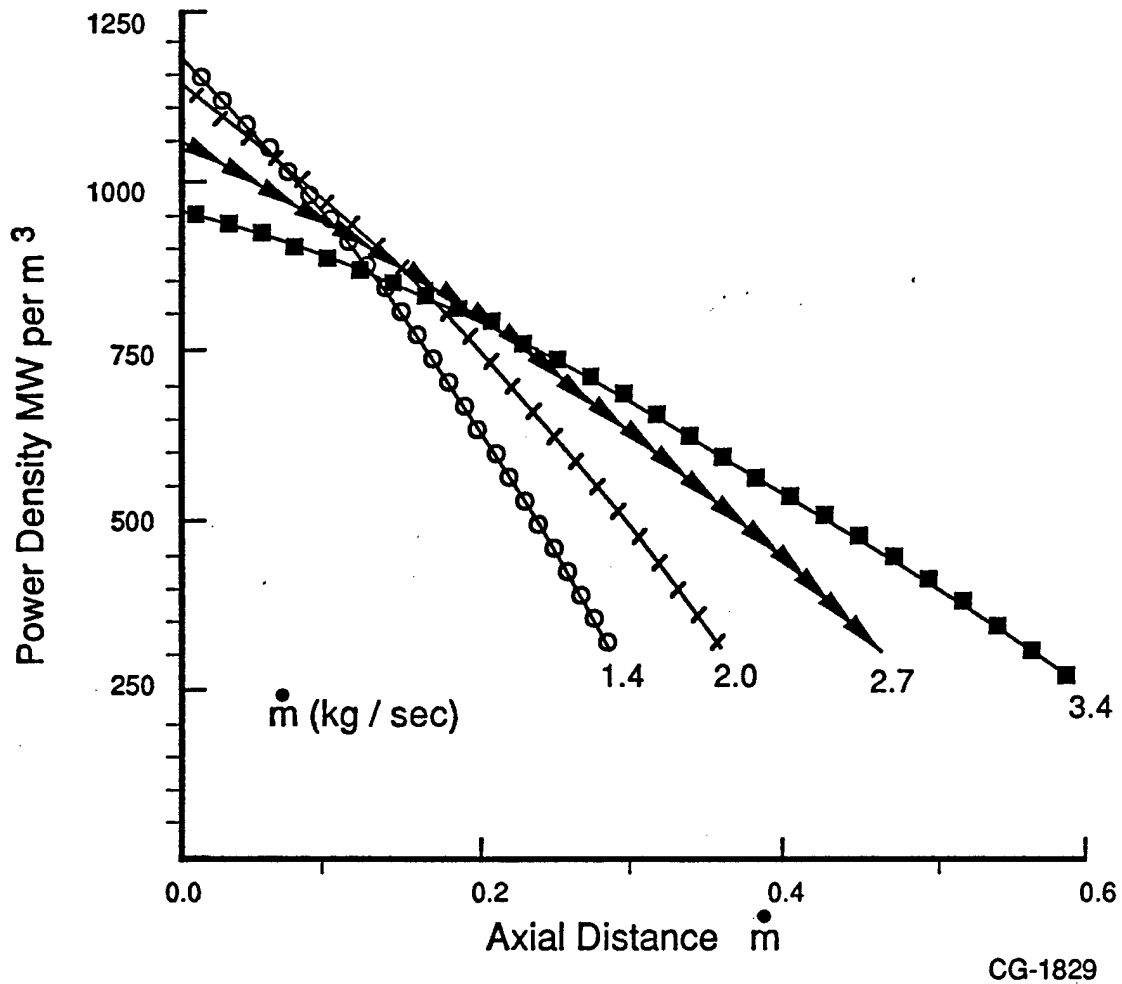


Figure 6. Effect of Generator Interaction with Operating Point - Power Density, Mass Flow and and Supersonic Generator Length.

TABLE II. MHD GENERATOR DESIGN FEATURES AND OPERATING POINT

Combustion: Fuel.....	Al:C (50:50)
Oxidizer.....	O ₂ (gas)
Stoichiometry.....	0.77
Mass Flow Rate.....	2.8 kg/sec
Combustion Pressure.....	40 Atms
Combustor/Nozzle Heat Loss.....	2% Q _i Input
Nozzle Throat Diameter.....	0.076 m
Nozzle Area Expansion (A/A*).....	3.80
Nozzle Length.....	0.20 m
Generator Length.....	0.46 m
Generator Wall Divergence.....	2.03°
Generator Mean L/D.....	5.1
Diagonalization Angle.....	30°
Peak Magnetic Field.....	3.2 Tesla
Generator Inlet Mach Number.....	2.5
Generator Inlet Pressure.....	2.15 Atms
Generator Inlet Temperature.....	3246 K
Generator Inlet Conductivity.....	104 S/m
Generator Inlet Velocity.....	2478 m/sec

heat sinking medium with a minimal surface recession accompanying its ablation in the reducing environment.

The predicted generator design performance calculations are summarized in Table III and Figures 7 and 8. The design calculations are based on a one dimensional generator flow model which does not consider the influence of the boundary layer in the plasmadynamics calculation. However, this computer model does include a direct accounting for the thermal boundary layer in its modeling of the generator electrical performance.

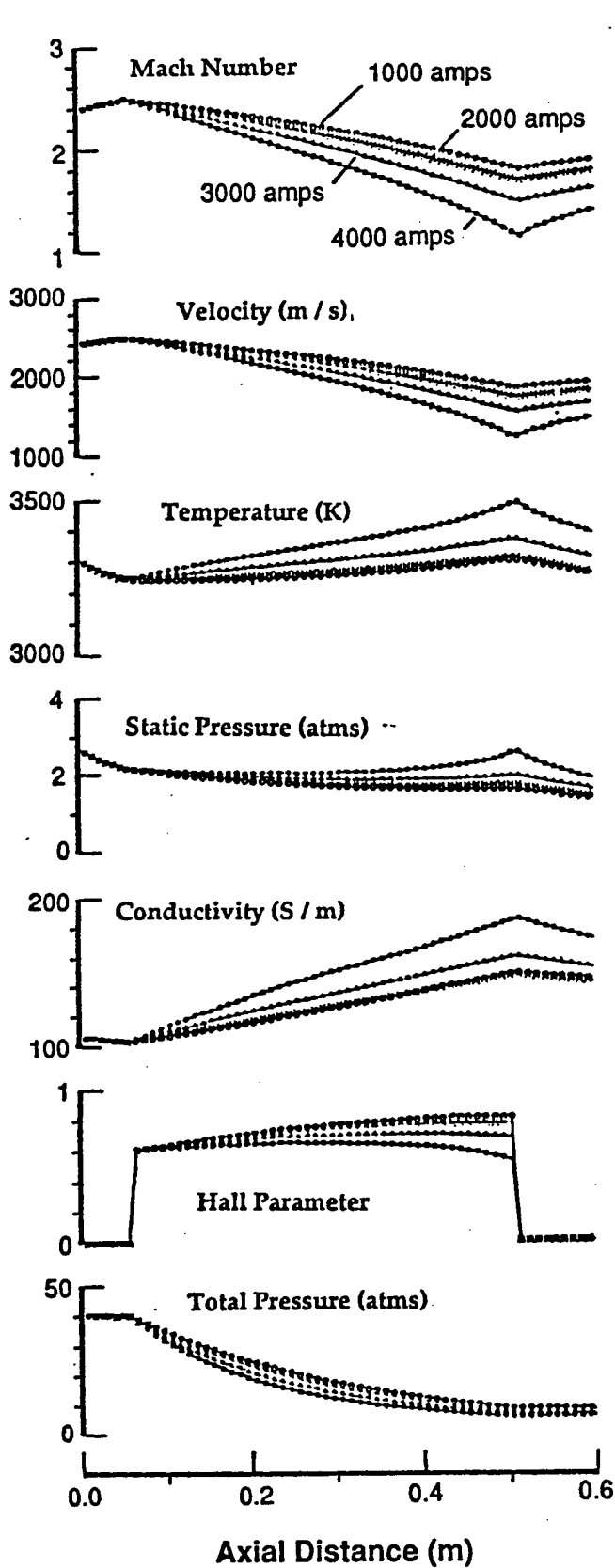
TABLE III. THEORETICAL MHD GENERATOR PERFORMANCE

(Maximum Power Operation)

Total Mass Flow Rate.....	2.8 kg/sec
Thermal Input.....	9.074 MW
Combustion Pressure.....	40 Atms
Combustion Temperature.....	4318 K
Generator Length.....	0.457 m
Generator Mean Flow Area.....	58.6 cm ²
Generator Volume.....	3076.9 cm ³
Diagonalization Angle.....	30°
Internal Surface Area.....	0.23 m ²
Average Heat Flux.....	380 Wts/cm ²
Load Current.....	2440 Amps
Load Voltage.....	751 Volts
MHD Power.....	1.83 MW
Specific Power Output.....	0.66 MJ/kg
Interaction Parameter (Ip)*.....	0.99
Power Density.....	600.6 Mw/m ³
Enthalpy Extraction.....	19.0%
Generator Efficiency.....	78.6%
Electrical Efficiency.....	38.6%
Mean Static Temperature.....	3.1 Atm
Mean Velocity.....	2101 m/sec
Mean Mach Number.....	1.90
Mean Conductivity.....	127 Mho/m
Mean Hall Parameter.....	0.7
Open Circuit Voltage.....	1574 Volts
Short Circuit Current.....	5350 Amps
Internal Impedance.....	0.31 Ohms
Joule Heat Dissipation.....	1.48 MW
MHD Push Power.....	-4.79 MW

*MHD Interaction Parameter Based Upon Pressure, $I_p = \int_0^t \frac{\bar{J}_x \bar{B}}{p} dx$

Plasmadynamics



Electrical Parameters

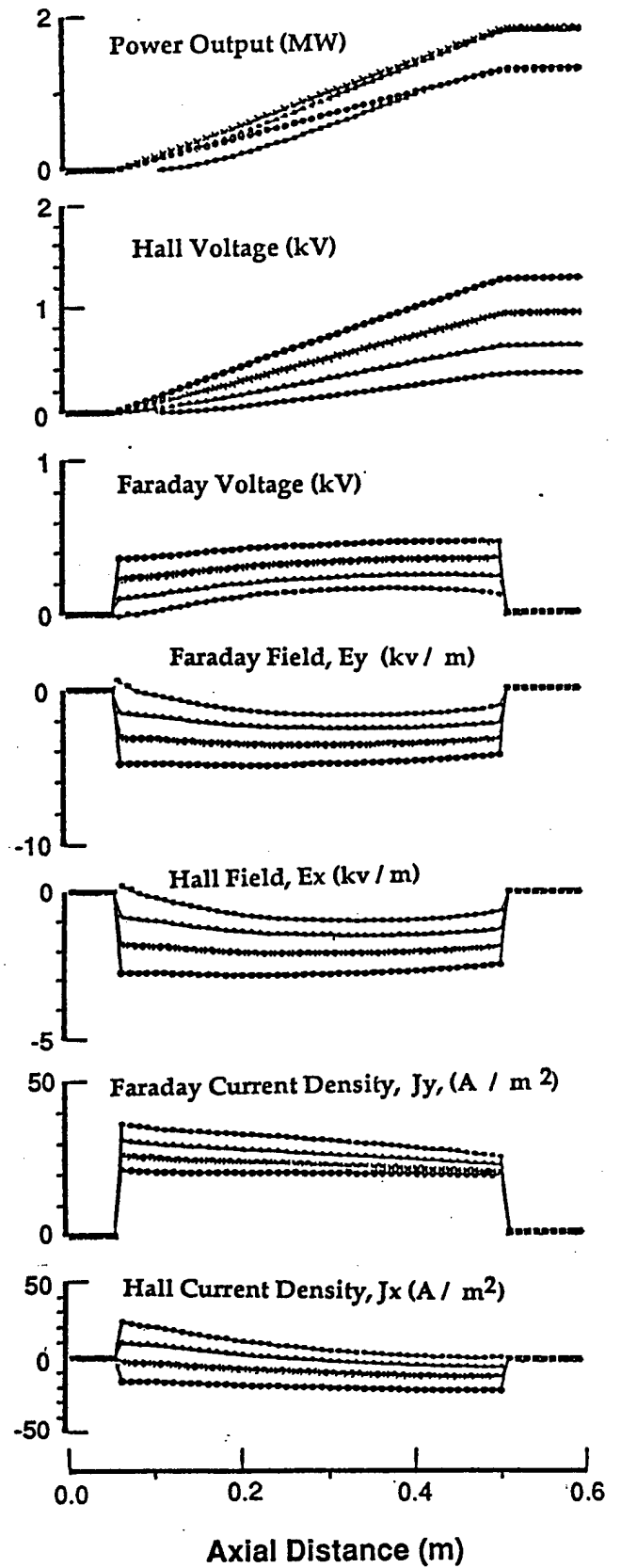
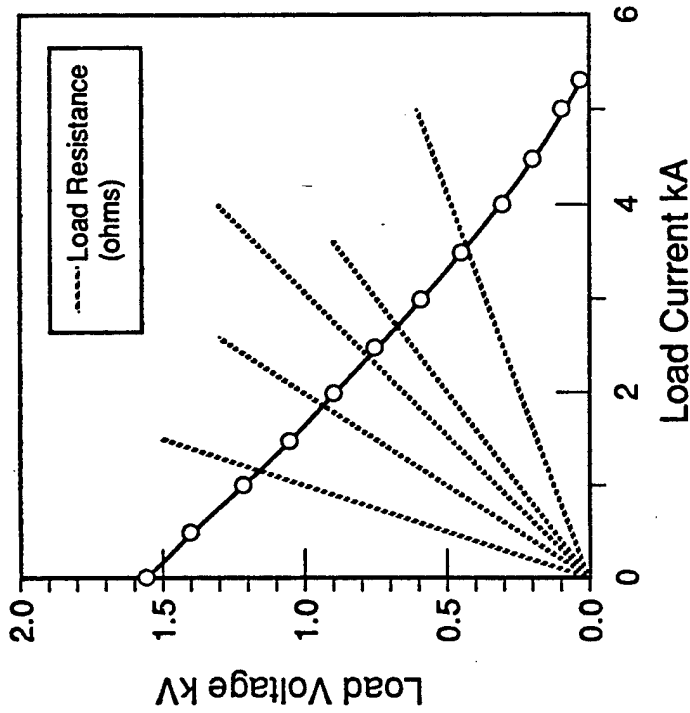


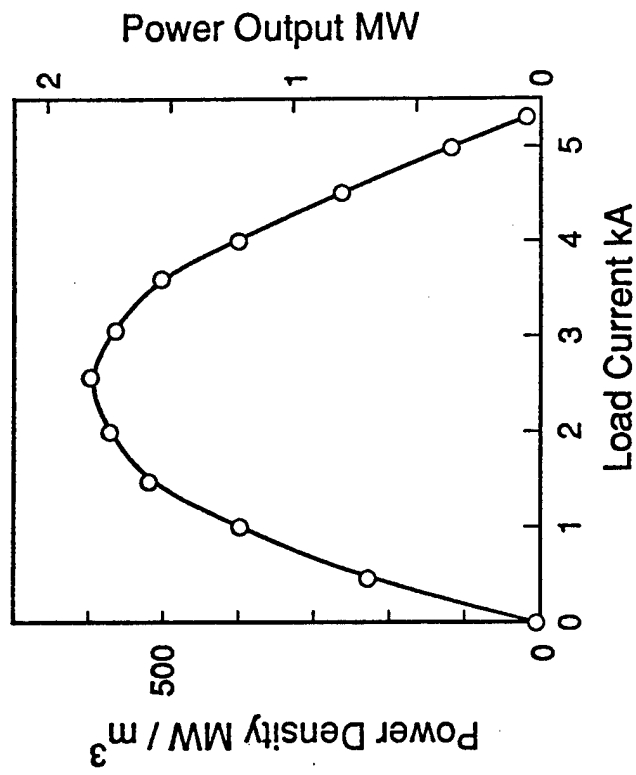
Figure 7. Calculated Plasma and Electrical Parameter Distributions for the Nominal 30' DCW Generator.

CG-1827

MHD Generator Loadline



a) Load Line



b) Power Characteristics

Figure 8. Calculated Load and Power Characteristics for the Nominal 30° Wall Angle DCW Generator Channel.

CG-1828

Specifically, the dynamic and thermal boundary layer growth is computed along the generator length assuming a fully developed turbulent flow over a rough wall. This calculation is uncoupled from the governing flow equations, that is, the flow equations are purely one dimensional in form. The local conductivity profile is computed after the fact from the thermal boundary layer and this profile is numerically integrated across the boundary layer to determine the overall boundary layer impedance. The local voltage drop is determined as the potential drop across the boundary layer and this drop is in turn used in determining the normalized voltage drop factor, Δ , which is used in the MHD electrical model.

Follow-up calculations of the conceptual studies were made using the UTSI version of the VNAP program. This program was used to compute the plasmadynamics specifically to determine an appropriate nozzle loft. The VNAP results computed the flow through the generator length and these gas dynamic calculations were used to estimate the growth of the boundary layer based upon a complete axisymmetric calculation of the radial flowfield. Growth of the generator dynamic boundary layer along its short length (18 inches) is quite insignificant as a consequence of the low length to diameter ratio. The generator loft that was specified for the final design included accounting for the slight growth in boundary layer through an increase the wall expansion above that determined in 1-D calculation. No calculations were performed for the test conditions using the available test data. The test data taken was not sufficient to provide a meaningful comparison of theoretical calculations provided by the model. For example, the tests were always performed with transient wall temperature while the model employs a steady state assumption which could never be achieved in testing.

Table III indicates that the nominal power prediction of 1.8 megawatts with a power density of 600 MW/m^3 for maximum power operation of the diagonal frame channel. Other design parameters of interest are given in the table including the MHD push power which is the power expended in moving the plasma against the Lorentz force in the channel volume. In Figure 7 the calculated plasmadynamic and electrodynamic parameters are presented as axial distributions for four levels of load current. The plasmadynamic characteristics are typically indicative of a decelerating flow in which the deceleration is proportional to the load current. That is, the velocity, Mach number, and

total pressures decrease as the load current increases, while the temperature, static pressure, and conductivity increase. For a load current of 4 K amps the plasma flow approaches a choking condition at the channel exit. For all load currents the static pressure at the channel exit is greater than atmospheric, and the total pressure is in excess of five atmospheres. Diffusion and pressure recovery processes were not required to prevent flow separation in the generator or exhaust ducting.

The loadline and power characteristics at the nominal generator design case are shown in Figure 8. The loadline is nearly linear throughout most of its extent with a shallow slope. The loadline is not straight, but rather curvature as evidenced at the terminal ends. At the open circuit end, the reduced Joule heating is less effective in offsetting the temperature and conductivity reductions accompanying the plasma expansion. The loadline slope and internal generator impedance are as a consequence slightly increased. At the short circuit condition the opposite situation occurs. Lines of constant load resistance are superimposed on the loadline for reference.

3.0 COMPONENT DESIGN

For the experimental phase, which was the principal part of the program, it was necessary to fabricate the required flow train components. These included the combustor-nozzle combination, the generator channels and the exhaust duct work. At the outset it was envisioned that the existing magnet, load dump and facility utilities would be available for use in the program. As a direct consequence of the calculations described previously in Section 2.0, it was apparent that the existing facility oxygen system, which had only a 195 psi delivery capability, would not be sufficient for the combustion pressure required. This necessitated assembly of a separate, bottle based oxygen system. In addition, the existing stainless steel, water cooled load bank was found to have insufficient capacity to be usable with the two low impedance generator channels to be tested. This, in turn, necessitated the construction of a load bank which by reconfiguring served as the load for both of the generators tested. In this section the mechanical design of the various hardware components are presented and discussed.

3.1 Combustor Design

The nominal combustor design is shown in Figure 9. The combustor is comprised of three metal pieces: the barrel, the injector face, and the nozzle. The barrel is an eight (8) inch diameter Type 304 stainless steel seamless tube having a 1/4 inch wall thickness and 54 inches in length. The injector end flange is welded exterior to the barrel while the downstream flange is interior to satisfy the magnet bore dimensional constraint. The combustor is to nominally operate at a combustion pressure of 600 psi and is supplied with gaseous oxygen at 1200 psi. The hoop stresses in the stainless steel barrel are 4500 and 9000 psi for these two pressures, respectively. The ultimate tensile strength of the stainless steel is 89000 and 50000 psi at 100 and 1200°F, respectively. The yield stresses for stainless are 28000 and 18000 psi for the same temperatures, respectively. The steel barrel has at least a safety factor of two with regards to the hoop stress.

The fuel grain has a nominal outer diameter of six (6) inches and is encased in a laminated glass shell of 1/8 inch wall thickness. The encased fuel grain is in turn separate from the stainless steel barrel by a 1/2 inch thick insulator. As shown in the

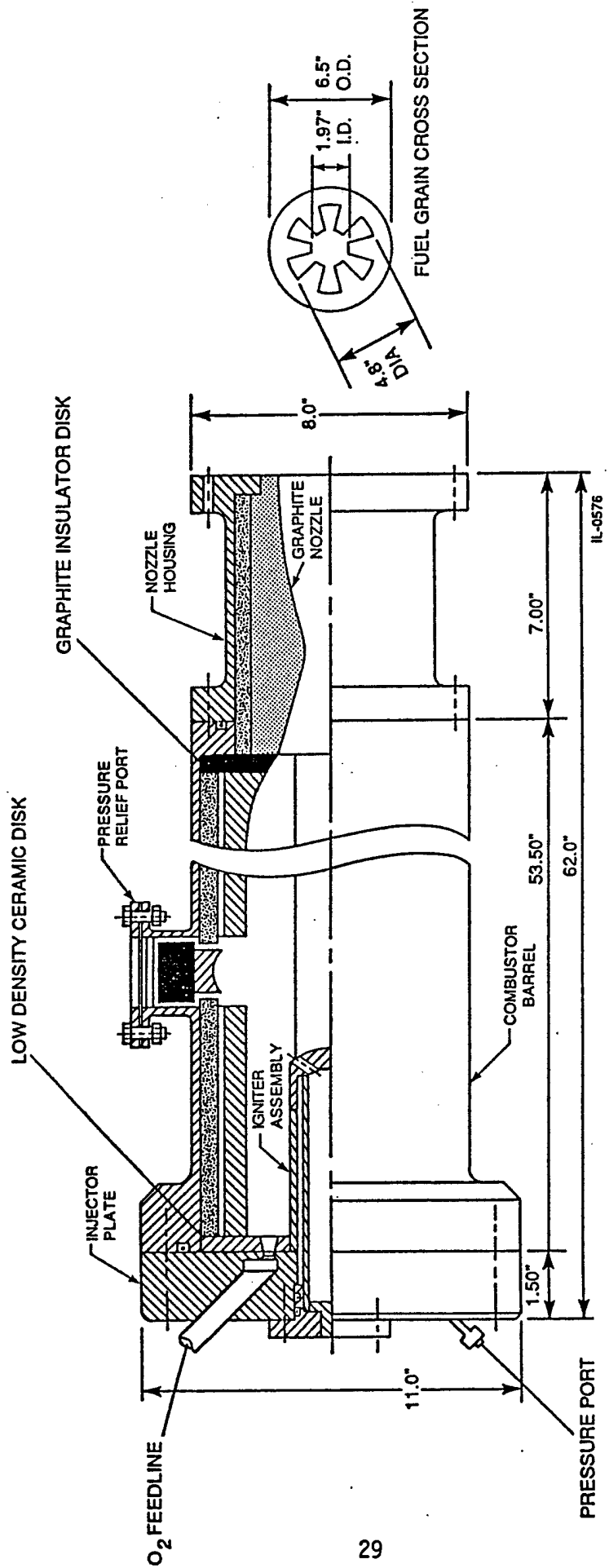


Figure 9. Preliminary Assembly Drawing of the Hybrid Combustor.

inset in Figure 9, the internal shape of the fuel grain is that of a six spoked wagon wheel configuration with the inner and outer radial dimensions of the spokes being approximately 1 and 2-3/8 inches, respectively. The fuel grain is of a uniform cross-sectional shape for most of its length except near the ends. Near the nozzle end of the combustor, the outer grain spoke radius is reduced to 1-1/2 inches to mate with the nozzle contour. At the igniter end, the grain is cylindrical with an inner radius of 2-3/8 inches and no spokes for an axial distance of 6.5 inches. The total combined internal area of the fuel grain is initially 9.5 ft.²

While the diameter of the combustor is set primarily by the magnet bore width, its length, or more appropriately its length to diameter (L/D) ratio, is set by the required fuel consumption rate. For the desired nominal total flow rate of 2.8 kg/sec at an equivalence ratio of 1.3 (stoichiometry = 0.77) the Al/C fuel mixture consumption is 1.18 kg/sec. The fuel surface area, density, and characteristic regression rate must be combined to yield this desired result. However, there was no known experience with this fuel, and neither its density or regression rate were known. The regression rate was estimated to be 0.09 cm per second based on experience with all aluminum based grains. The density was estimated to be 1.55 gm/cc based on a theoretical maximum density of 2.42 gm/cc for a 50-50 mixture of aluminum and carbon, an 80% of theoretical packing efficiency, and a 20% allowance for the binder. The 9.5 ft² of exposed area was thus estimated to yield a design value of 1.23 kg/sec of fuel loss which would provide some allowance for the regressive burning characteristics of the fuel grain cross sectional geometry and incomplete burning surface utilization. Theoretical calculations indicated that maximization of power density was not particularly sensitive to excursions in stoichiometry about the design value of 0.77. From the standpoint of using graphite ablative materials for internal thermal shielding it was also advantageous to insure that the plasma was always reducing as would result from sub-stoichiometric combustion.

The fuel grains were made in four sections by casting the epoxy bound fuel mixture in a standard fiberglass pipe with a styrofoam core to provide the wagon wheel cross sectional shape. The styrofoam core was dissolved with acetone after the epoxy fuel grain binder cured. Each of the fuel grain sections was 13.125" in length. Various joint

geometries were used to connect the joints and are more fully discussed in section 4.3.

A pressure relief port was provided for in the combustor barrel as shown in Figure 9 but located approximately midway along the length of the combustor. When installed in the magnet the pressure relief port was positioned vertically between the coil force containment structures shown in Figure 5. The pressure relief port was comprised of a tube welded to the combustor barrel communicating with an opening through the fuel grain to the central combustor cavity in the center of the fuel grain. The relief port is covered by a thin aluminum sheet behind which a 3/8 inch high steel shear piston is positioned. The shear piston carries a double "O" ring seal. The steel shear piston in turn is positioned over a much higher insulating phenolic piston. In the event of an over pressure the shear piston would punch a circular blank from the aluminum sheet and the punched blank, shear piston, and phenolic piston would be expelled leaving an open port to the combustor's main cavity. The thickness of the aluminum shear disk determined the actual relief pressure and a .032 inch thickness with a burst pressure rating of 1200psi was used.

The oxygen injector is essentially in the form of a one (1) inch thick blind flange at the front of the combustor. In its center it has an opening for the igniter assembly and within its combustor side face an oxygen manifold is located. This manifold was constructed by milling a circular slot followed by welding a cover over it and drilling six injector holes in the cover. The manifold has a single outside supply connection which is not shown in the figure. The six oxygen injector holes are positioned to inject the oxygen along the fuel grain cavities between the spokes. Initially, a low density ceramic thermal insulator disk was positioned between the fuel grain and injector plate. During the first test this disk failed and incurred a failure of the injector flange as well. The new injector flange was made heavier with a 1 1/2 inch thickness and a graphite disk was used for the insulator plate. These were used without incident for the remainder of the program. The insulator plate is pinned to maintain its position so that it does not rotate and block the injector holes.

The igniter was initially designed as shown in Figure 9. It was comprised of a stainless steel body, a fuel lined phenolic barrel and a graphite nozzle with six orifices.

The nozzle cap, and phenolic barrel are attached to a central stainless steel, perforated tube by a single screw. The igniter is designed to be removable from the outside of the combustor and is shown in Figure 9. In use, a three step ignition process is involved. A group of pellets comprised of a mixture of boron and potassium nitrate is loaded in perforated central tube along with an electric match. The match leads are brought to the outside through a pressure tight elastomer compression fitting. When fired, the match ignites the pellets which in turn ignites the propellant lining the inside of the phenolic barrel. These resulting combustion products exit the six nozzle orifices directed into the six interspoke fuel grain cavities and with oxygen present the fuel grain ignites. The pellets burn in a time of milliseconds and it is the main charge in the phenolic barrel that provides approximately 2 seconds of hot flame for the main fuel grain ignition.

Initial testing of the combustor resulted in repeated loss of the phenolic tube and nozzle end of the igniter during combustor firing. While only inconsequential to the combustor operation, the loss of igniter nozzle posed a hazard to the combustor nozzle from the potential of impact damage. As a consequence, the igniter assembly was redesigned to extend less into the combustor main cavity as shown in Figure 10. Only the nozzle of the igniter is exposed in the combustor in the redesigned configuration. This design was used successfully for the remainder of the program.

The aft end of the combustor is comprised of the nozzle closure which is simply a graphite nozzle surrounded by a ceramic insulator and encased in a double flanged stainless steel shell. The nozzle is replaceable since it is expected to erode significantly. The erosion may be both from thermochemical ablation and mechanical removal of material. The former is surface diffusion limited combustion of the graphite, much the same manner as the fuel grain burns. The difference between the nozzle graphite and the fuel grain is that the graphite is a much denser carbon matrix which is not held together with a thermally degradable binder. As a consequence, the fuel grain simply has a faster surface recession rate than the graphite in the nozzle. The condensed aluminum oxide species may mechanically erode the graphite in the nozzle through impact. This is dominant material removal mechanism often noted in rocket and re-entry environments.

On the one hand, the nozzle length should be short to close couple the combustor to the generator and minimize thermal and electrodynamic losses. On the other hand,

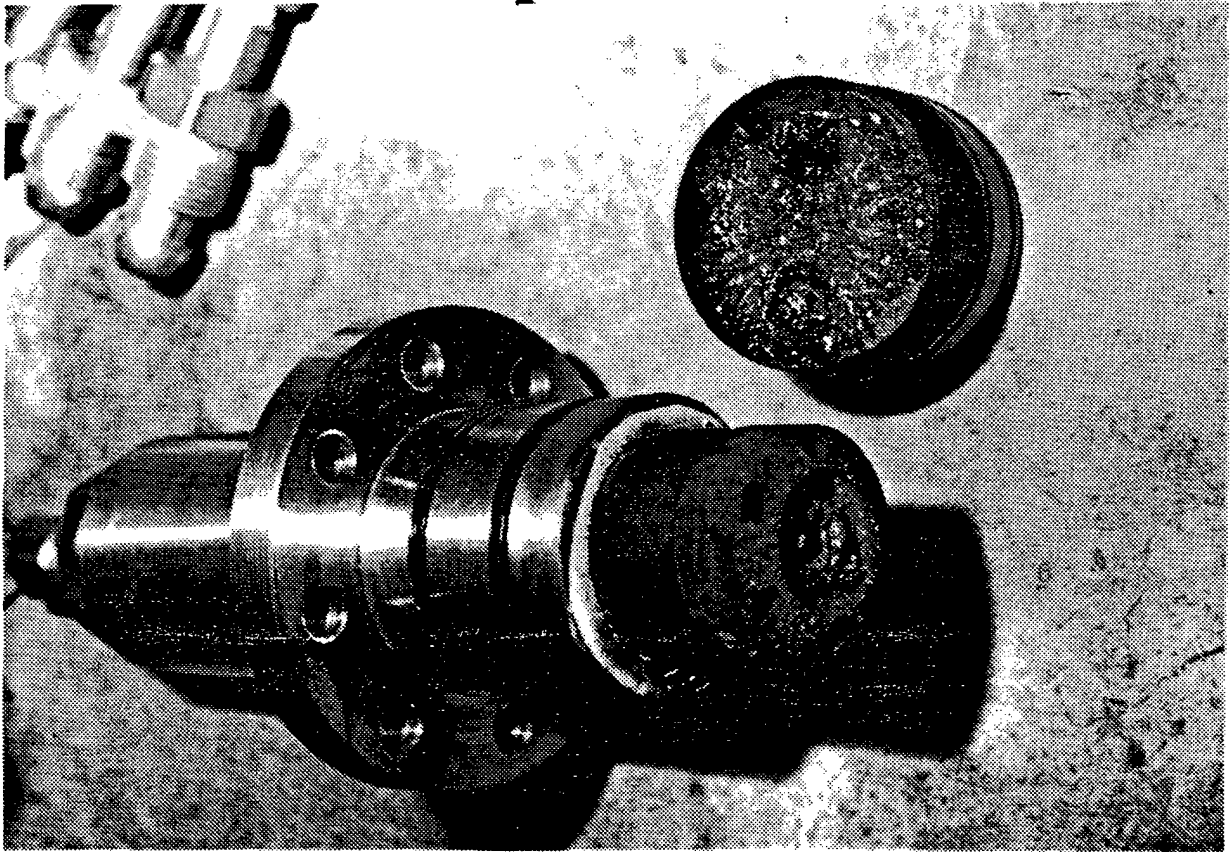


Figure 10. Photograph of the Redesigned Igniter Assembly After Use

the throat region which will be exposed to the most severe thermochemical and erosive environment should have as large of a radius of curvature as possible for its length in order to maximize its durability in this environment. The nozzle is designed to expand the plasma from the combustor conditions to a Mach number of 2.5 at its exit. The area ratio for this expansion is approximately 4.0 and for a specified exit diameter of 3.0 inches, the throat diameter required is approximately 1.5 inches.

Downstream of the throat the plasma flow is accelerating supersonically. The nozzle contour in this region must be aerodynamically contoured to avoid oblique shock formation or flow separation. The transition from the nozzle exit to the generator entrance should be smooth with no misalignment steps or angular discontinuities.

The nozzle design is shown in Figure 9. The nozzle is eight (8) inches in overall length with the subsonic portion to the throat being 3.0 inches in length. The 5.0 inch length supersonic region downstream of the throat was contoured in accordance with inviscid method of characteristic calculations.

While not shown in the figure, the combustor has one chamber pressure port and three thermocouples in the nozzle as part of its internal instrumentation. The combustor pressure port is located in the injector plate. The three nozzle thermocouples are located on the outer surface of the graphite nozzle block (inside the steel shell and refractory) and axially located at the entrance, throat, and exit stations. During testing additional surface mounted thermocouples on the outer combustor shell were also routinely used. The internal instrumentation was kept to a minimum to minimize penetrations of the shell which can be potential plasma leaks. For the chamber pressure and nozzle thermocouples only two penetrations of the pressure vessel were required.

The combustor, nozzle and fuel grains were supplied by Redevco, Inc. of West Valley, Utah under subcontract to UTSI.

3.2 Oxygen System

While the CFFF facility has a large capacity of gaseous nitrogen, oxygen, and compressed air supplies as part of its utility complement, the supply pressures were insufficient for satisfying the requirement of the present program, other than for purge and calibration requirements. In addition, the air systems (particularly the high pressure air

system) are not oil free and therefore could not even be used to calibrate system components intended for oxygen conveyance.

A separate high pressure gaseous oxygen system was required for the combustor testing. The oxygen supply was comprised of a manifolded group of "K" bottles as shown in Figure 11. These bottles are nominally charged to 2200psi and contain 250 scf or approximately 21 pounds of gas. The combustor supply pressure is required to be approximately 1200 psi to maintain choked injection orifices at the design combustion pressure of 600 psi. Ten bottles were used to achieve the desired flow rate and delivery pressure values as discussed in section 4.1.

The piping schematic in Figure 11 shows the various valves and controls for the oxygen system. A manual line valve along with manual valves on each of the bottles are used to change out individual bottles at the manifold and to isolate the downstream line when necessary. The single control valve shown in Figure 12 is of a fail closed design which is pneumatically opened against a spring such that loss of electrical control or actuating air the spring will mechanically close it.

Nitrogen purge is tied to the oxygen supply with a pneumatically operated valve. Since the oxygen pressure is substantially higher than the available nitrogen pressure, a check valve is used to prevent back flow into the facility nitrogen supply. The check valve also provides for an automatic start of purge nitrogen at the end of the combustor operation. When the oxygen valve closes, the pressure in the line to the combustor falls. Assuming that the nitrogen valve is open, as soon as the oxygen pressure in the line drops below the nitrogen supply pressure, the check valve will open and the oxygen line and combustor will be purged. Purge flow rate will be approximately 1/6 the oxygen flow rate or approximately 0.6 lbm/sec. An orifice in the oxygen supply line is used to monitor oxidizer flow rate during the operation. As a cross-check, the bottle pressures before and after a combustor firing are used to determine the total flow and mean flow rate as well.

The oxygen system as described worked well for initial checkout of the combustor as described in Section 4.1. However, the pipe volume upstream of the combustor proved to be too large. That is there was 0.326 cu ft. of volume between the control valve and combustor charged to 1200 psi when the control valve closed at the end of a run. This presented a safety hazard as it would bleed down through the combustor before the

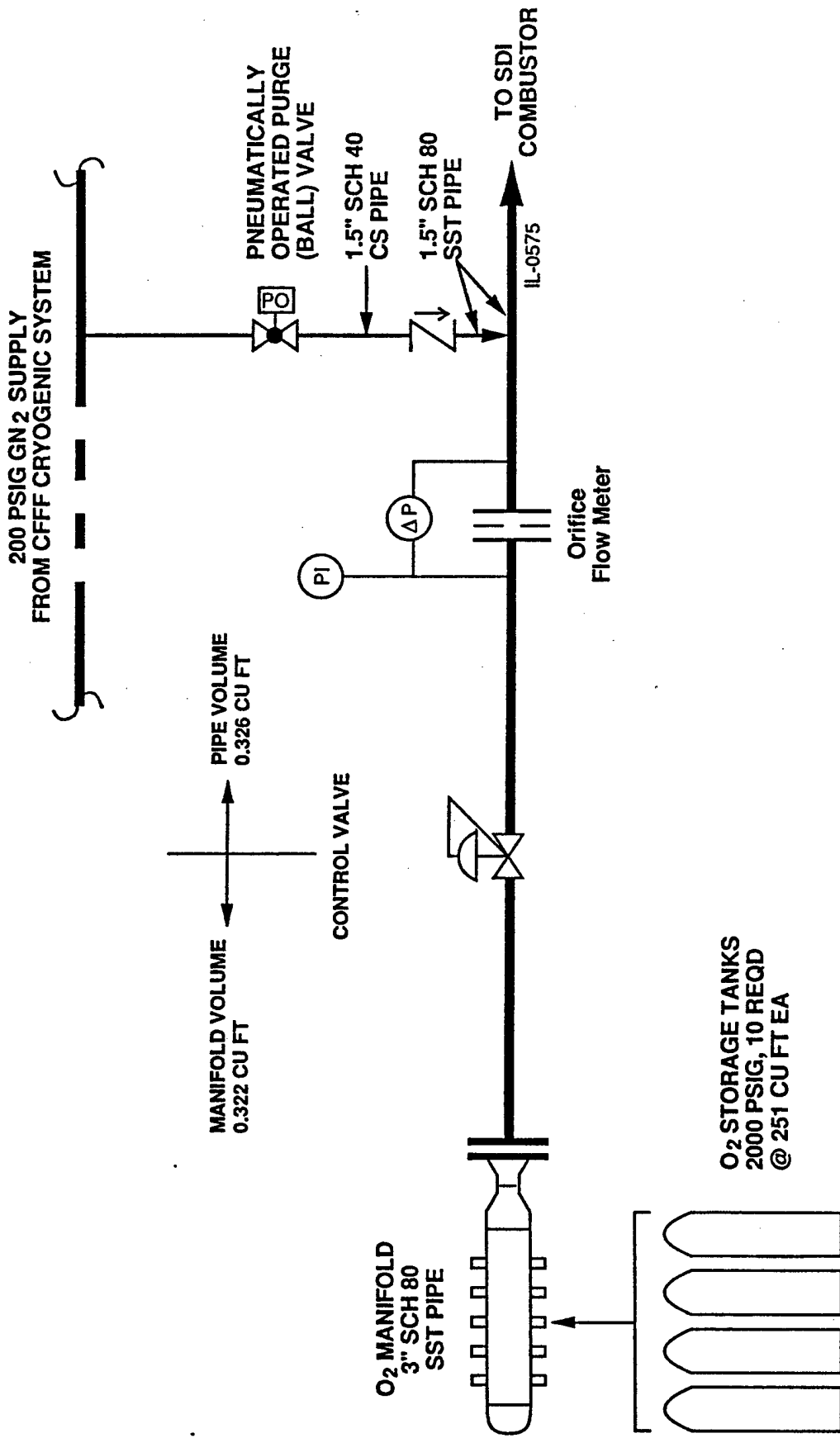


Figure 11. Schematic of the Gaseous Oxygen System for Combustor and Generator Testing in the CFFF Facility

purge gas could be introduced. To correct this problem a second open/closed valve was located closer to the combustor on the oxygen feed line and the purge connection moved just downstream of this valve. This valve used to terminate operation earlier by reducing the effective line volume upstream of the combustor. In operation, oxygen is trapped in the supply line between the valves but it can be bled off safely well after the operating sequence is over.

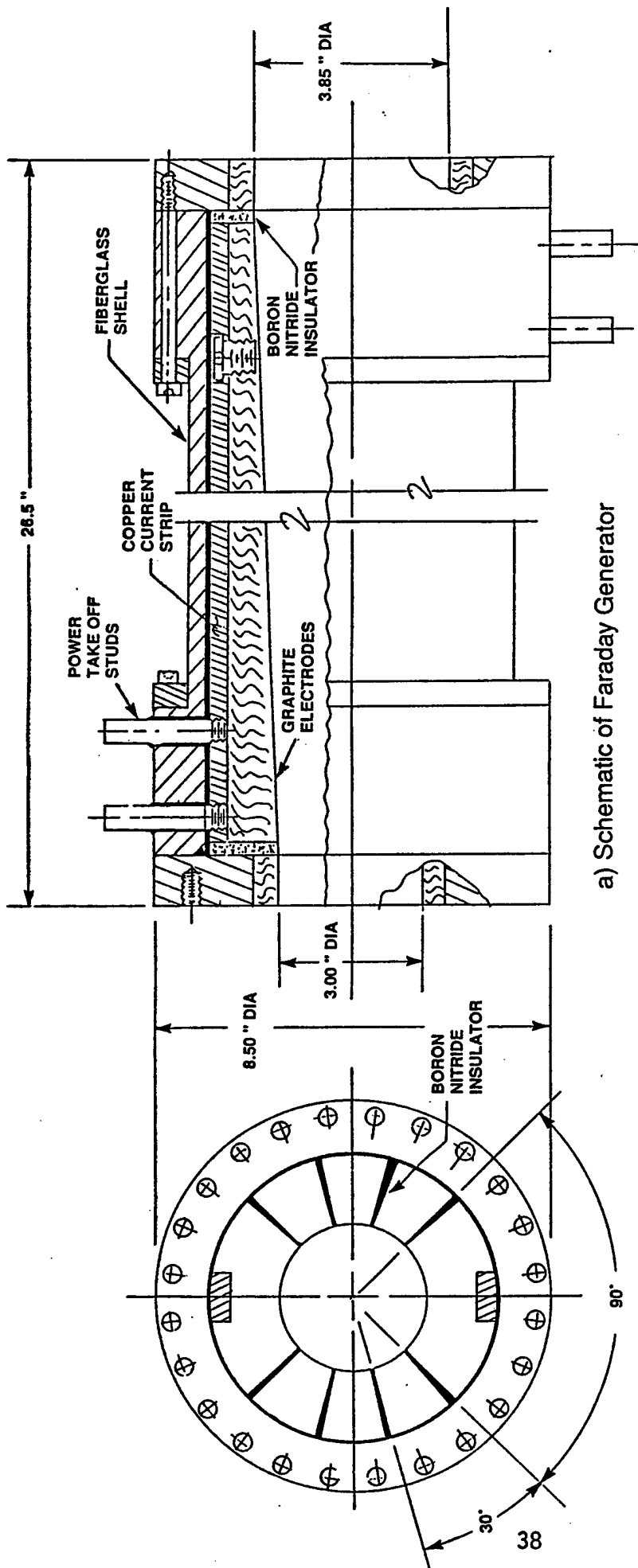
3.3 Faraday Channel

The Faraday configuration generator channel is depicted in Figure 12. It has an active length of 24 inches, has an inlet internal diameter of 3.00 inches which tapers to an exit diameter of 3.85 inches. The mean diameter is 3.42 inches and the mean distance between electrodes is 2.92 inches. The active internal volume of the Faraday generator is 224.5 in³ (0.00368m³). In cross-section the continuous electrodes each cover 90° of arc and are separated by eight longitudinal side wall insulators. The side wall insulators are boron nitride. The electrodes and longitudinal sidewall segments are graphite.

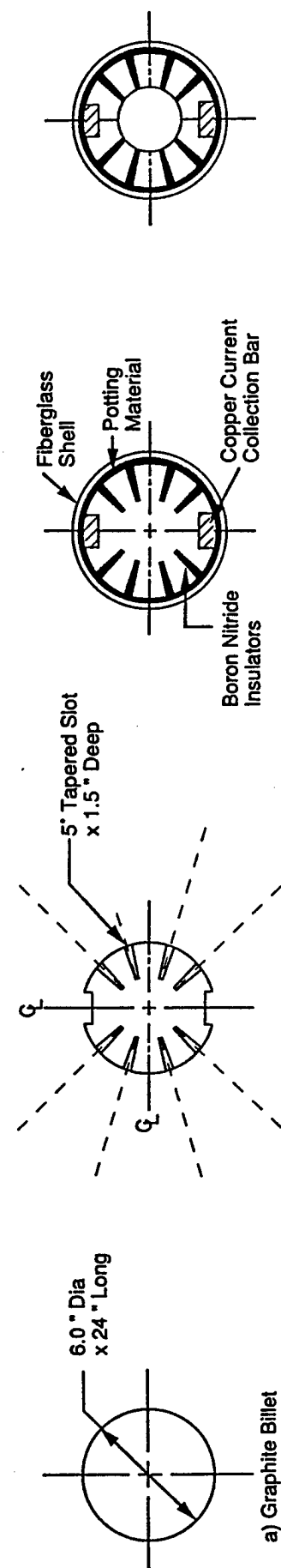
The graphite electrode material is not amenable to heavy duty mechanical or adhesive bonding and is strong primarily in compression. As a consequence, single point power take off can be a problem insofar as connection to the graphite is concerned. Current concentrations at a power takeoff point can lead to increased localized Ohmic heating as well as possibly arcs which in the presence of a magnetic field are highly undesirable. As a solution, a longitudinal copper current collecting bar was imbedded in the anode and cathode as shown in Figure 12. The bar served as a hard point to make the external connection for power take off. The bar also provided for multiple mechanical fastening points to the graphite thus distributing the mechanical and electrical loading.

The graphite electrode and insulator segments were potted within a flanged fiberglass pressure vessel as shown in Figure 12. The power take off studs passed through the flanges to connect with imbedded current collection bars.

The channel construction technique is believed to be unique and is inherently simple. The channel was built from the inside out. The starting point was a graphite cylindrical billet into which the longitudinal side wall insulator slots were milled. The boron-nitride



a) Schematic of Faraday Generator



b) Construction Sequence

Figure 12. Detail of Faraday Generator Construction with Construction Sequence

insulator strips were placed into the milled slots as well as the current collection bars. This completed assembly was then potted within the slightly oversize (1/8 inch on a radius) fiberglass pressure vessel. The fiberglass pressure vessel was comprised of commercially available fiberglass pipe modified with the flanges. After the inner assembly was potted within the outer pressure vessel, its internal bore was made, thus dividing the initial single piece of graphite into the two electrodes, six insulators, and eight inter-electrode insulators. The wedging action of the individual pieces hold them in their radial position. In addition, the end insulator disks could have steps incorporated to prevent inward motion of the pieces but this was not done for this small device.

A photograph of the completed Faraday channel is shown in Figure 13.

3.4 Diagonal Channel

The mechanical configuration of the diagonal generator channel is shown in Figure 14. The diagonal generator has the same internal radial dimensions - inlet diameter of 3.00 inches, exit diameter of 3.85 inches, mean diameter of 3.425 inches - but has an overall active length of 28.25 inches and an internal volume of 264.25 in³ (.00433 M³). There are seven inclined graphite frames having a 30° inclination angle and a 2 inch pitch between the truncated cylinder power take-off frames at either end. The insulators are 0.25 inch thick boron nitride.

The power take-off scheme is similar to the scheme used for the previously discussed Faraday channel. In the case of the diagonal channel a semi cylindrical copper plate is attached with multiple screws to the graphite of the power take-off frame. Studs passing through the fiberglass end flange attach to this copper current collection plate. Anode and cathode connections are identical in this regard. The steel end flanges which have an inside graphite liner are common to both the Faraday and diagonal channels.

Construction of the diagonal generator channel is completely analogous with the assembly of the Faraday channel in that they both were built inside out starting with a machined graphite billet. The billet insulator grooves in the diagonal channel have parallel sides for a uniform thickness insulator. Each complete interelectrode insulator was comprised of two c-shaped halves which joined at the top and bottom with a lap joint. The insulators were placed in the outside grooves of the graphite billet, the assembly was

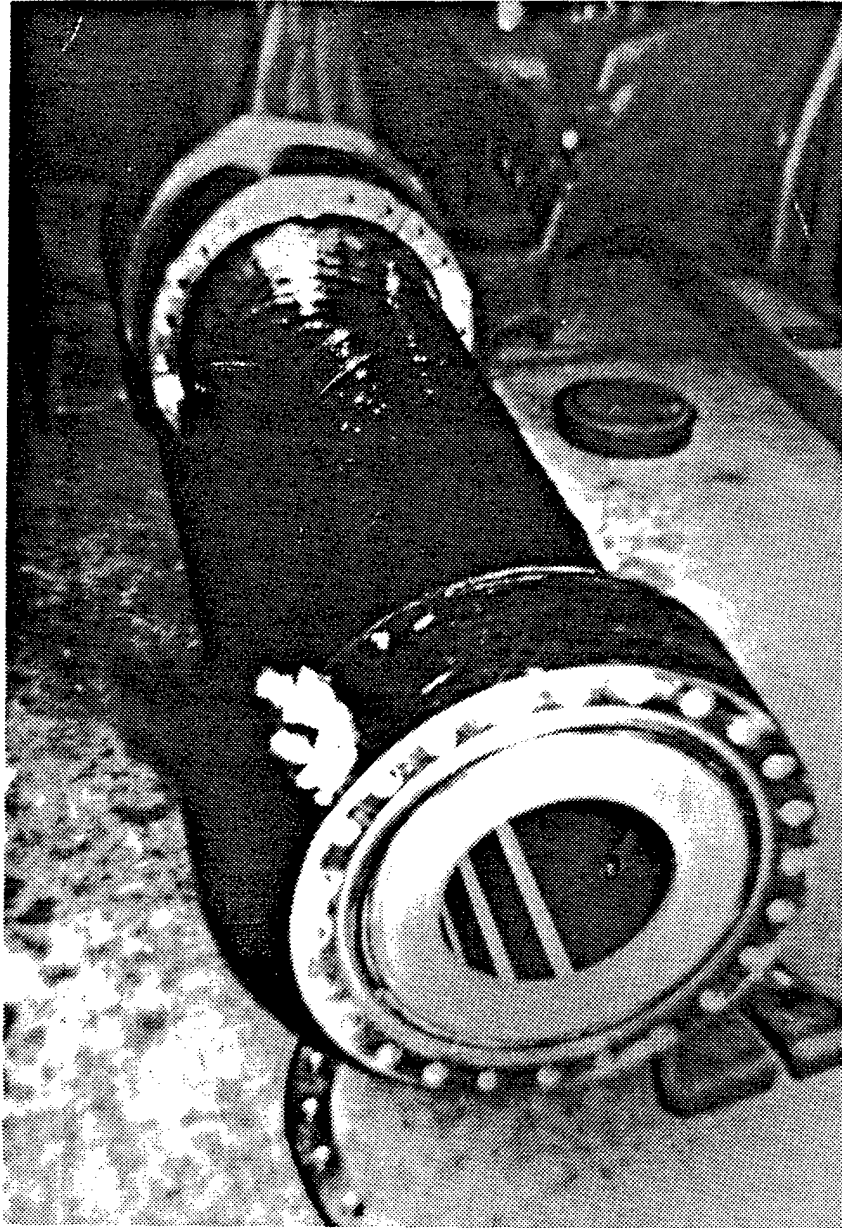


Figure 13. Photograph of the Faraday Channel

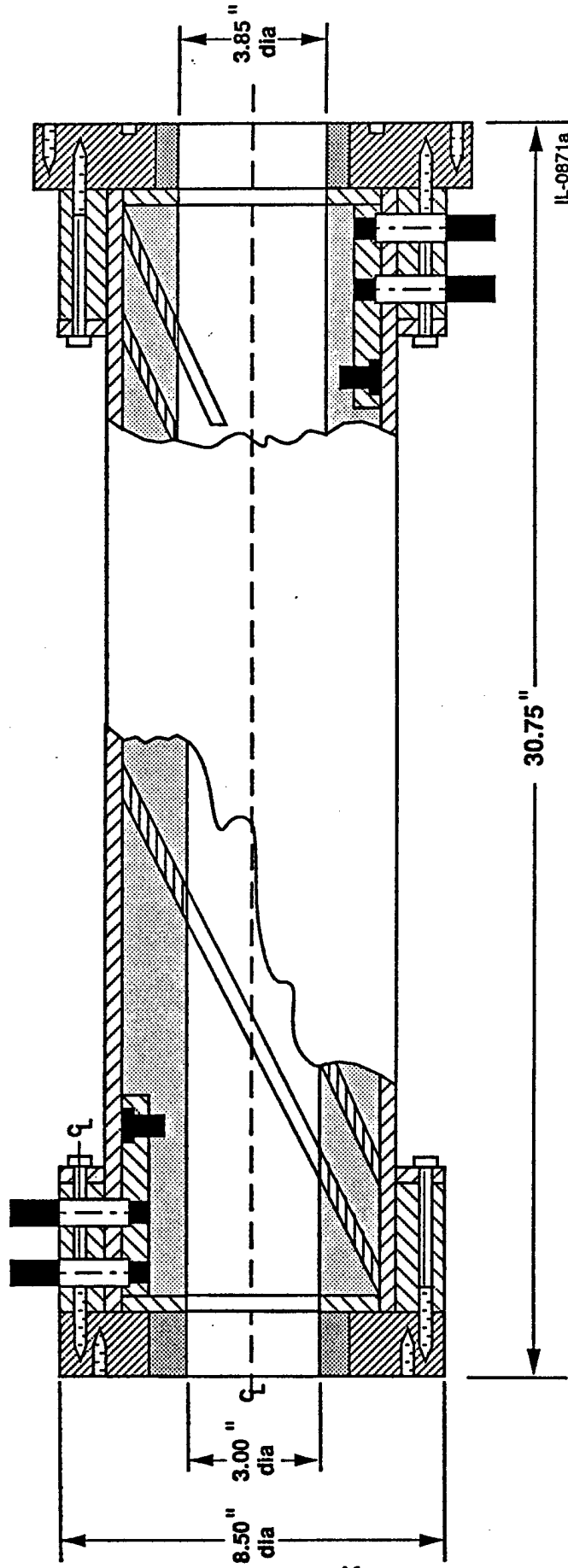


Figure 14. Assembly Drawing at the DCW Generator Channel

potted within the fiberglass outer shell and then bored out to complete the channel. A photograph of the completed diagonal generator is shown in Figure 15.

3.5 Load Bank

For powered generator channel testing a suitable load bank for the generated power is required. Table IV below presents the nominal theoretical peak power characteristics for the Faraday and diagonal conducting wall (DCW) generators at an applied field of 3.2 Tesla. The Faraday generator is a low impedance generator and is expected to produce approximately one half the power of the DCW generator. The currents and voltages given in Table IV are one half of the short circuit and open circuit values respectively and do not account for load line non-linearities and are conservative in this regard. Nevertheless the values illustrate that the internal impedance, and consequently the load for maximum power, differ by an order of magnitude between the two configurations.

Table IV. Nominal Load Requirements

	Faraday Channel	DCW Channel
Load Current, KA	5.2	2.675
Load Voltage, V	162	787
Load Resistance, Ω	0.031	0.294
Dissipated Power, MW	0.84	2.10
Power Density, MW/M ³	228.	485.

The load bank is comprised of ten 3.81 cm o.d. stainless steel tubes each of 7.46 m



Figure 15. Photograph of DCW Generator Being Assembled

length. Copper 1000MCM cables having a cross-sectional area of 5.06 cm² and twelve meters in length are used to connect the generator to the load bank. The connective cables do not connect directly to the generator power take off studs but rather connect to copper straps outside of the magnet bore which in turn connect to generator power take off studs. These straps which are 2.25 x .25 inches in cross section, have a conductive area of 3.62 cm² and are sufficiently rigid that they can be mechanically held to counteract the Lorentz forces acting on them within the magnet bore.

The thermal and electrical properties of the copper and stainless steel are given in Table V for reference.

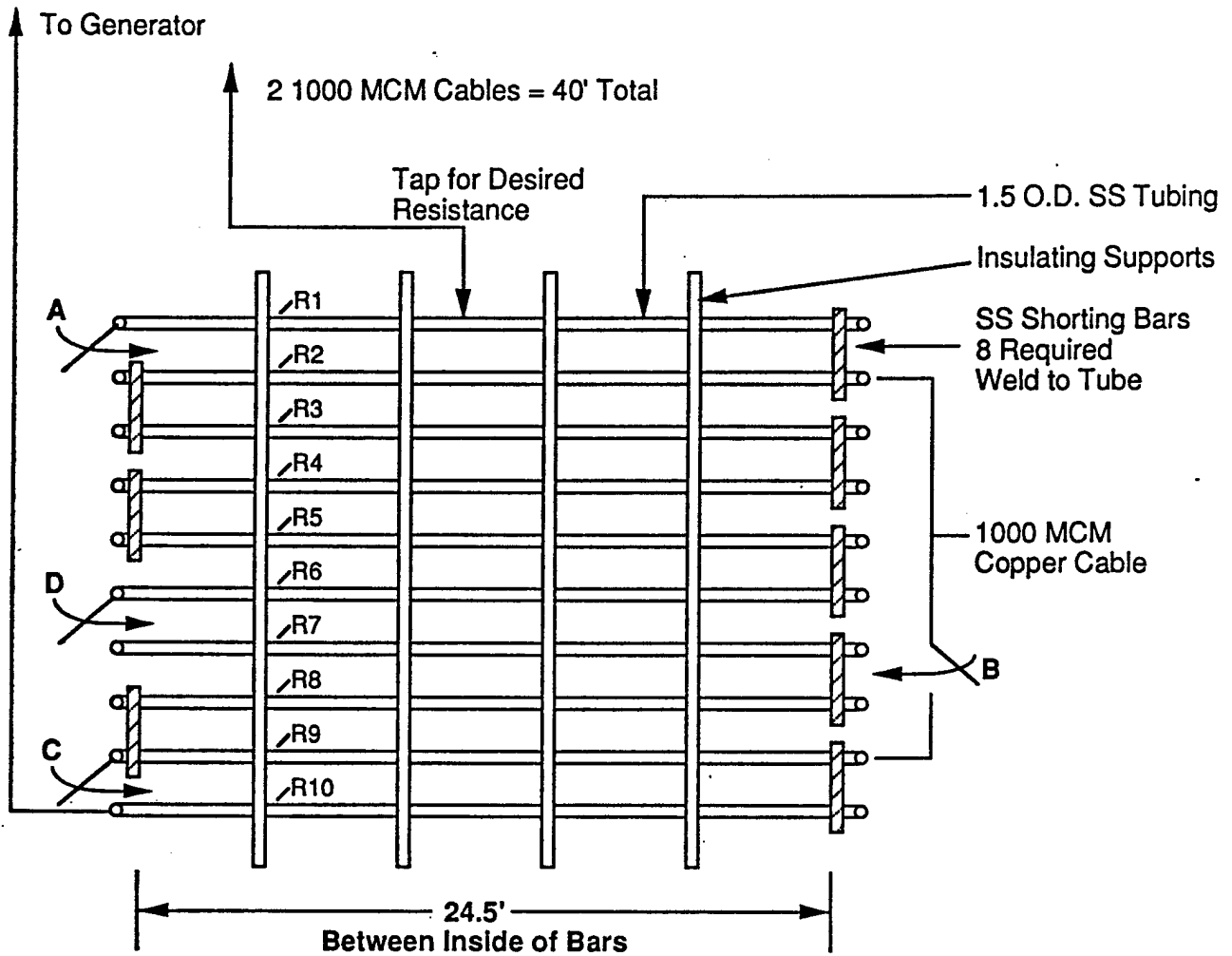
Table V. Load Bank Material Properties

	Copper	Stainless Steel
Volume Resistivity, δ , Ω -cm	1.673×10^{-6}	7.3×10^{-5}
Density, ρ , kg/m ³	8960	8020
Specific heat, C_p , cal/gm°C	.092	0.12
Cross Sectional Area, cm ²	5.06	1.748
Weight per unit length, kg/m	4.53	1.402
Resistance per unit length, Ω /m	$.33 \times 10^{-4}$	$.417 \times 10^{-2}$

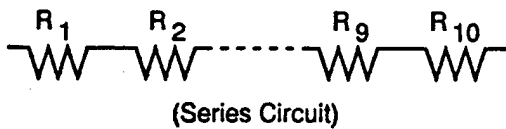
The cables and channel straps were designed to have a negligible resistance in comparison with the actual load resistance. As indicated in the Table V above the copper cable resistance per unit length is approximately 2 orders of magnitude less than that of the stainless steel used for the load element.

A schematic of the load bank is shown in Figure 16. For the DCW load configuration the ten resistor tubes are in a series connection which provides the maximum resistance configuration. The order of magnitude reduction in resistance required for the Faraday configuration is achieved by a series parallel connection as shown in the figure.

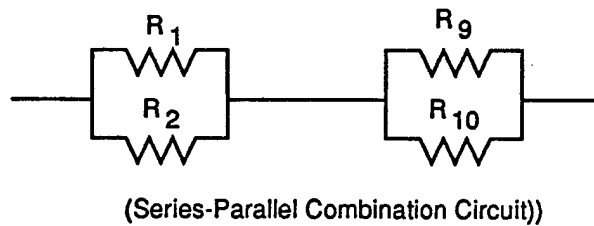
The load is also transient by virtue of the fact that it dissipates the applied energy as heat which for the short durations involved remains within the electrical conductors in the load bank and cable as well. The temperature rise rate in the conductors is independent of their length and depends only on the material properties and the square of the current density. The Faraday generator which has the higher current output is therefore the most critical for the cable connectors. For a peak current value of 5.2 KA from Table I and the copper material properties from Table V, the temperature rise in the cable is found to be 0.51° C/sec. For this same peak current and noting that in the Faraday configuration a load resistor element only carries half the load the load bank tube temperature rise is calculated to be approximately 40° C/sec. For the series connected diagonal generator configuration and a nominal load current of 2.68KA the calculated cable and load temperature rises are 0.13° C/sec and 42.5° C/sec respectively. These rates of increase are sufficient to permit 5 to 10 sec run durations. In addition, metals exhibit a strong positive functional dependence of their resistance with temperature. As the resistive tubing heats up its resistance increases thus shifting the load away from the peak power point in the open circuit (higher impedance) direction. The calculated temperature rise rates are consequently maximum values and thus conservative in this regard.



Equivalent Circuit For DCW Configuration With Jumpers A, B, & C Open, D Closed



Equivalent Circuit For Faraday Configuration With Jumpers A, B, & C Closed, D Open



IL-0682

Figure 16. Schematic of Load Bank Design for Generator Testing

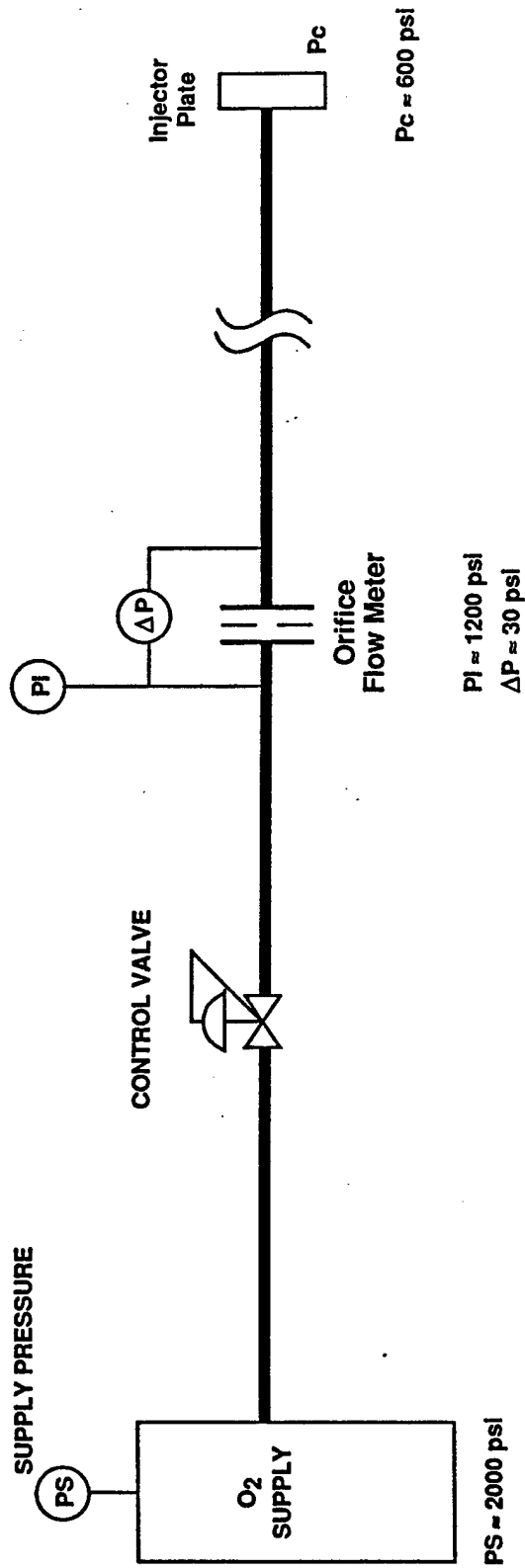
4.0 Test Results

During the course of the program the various components and systems were tested separately and in combination. The tests were performed to verify safe operation, expected performance, repeatability and adequacy of the instrumentation. The final tests of the entire flow train were, of course, the end result of the program. In the following sections the testing is described by component or system rather than chronologically for convenience.

4.1 Oxygen System

The oxygen supply system design was previously described in Section 3.2 with a complete schematic in Figure 12. Figure 17 is an abbreviated schematic of the oxygen system as initially used and it shows all of the measurements, control points and their locations. In particular, the purge system which is not relevant for its operation is not shown and the combustor manifold which is a primary flow control device is shown. As indicated in Figure 17 the oxygen system consists of four elements: the supply manifold, the control valve, the orifice flow meter and the injector plate, serially connected by low loss piping. Instrumentation is comprised of three pressure measurements: the manifold supply pressure, a static line pressure upstream of the orifice flow meter and a differential pressure across the flowmeter. The manifold supply pressure was read manually from an analog gauge before and after operation. The other pressures were connected to the high speed data acquisition system and continuously read. The actual control valve was operated in only fully open or fully closed configurations and while it was a controllable valve it in fact had no controller physically installed on it. Active regulation of the feedline pressure for the short duration runs was not deemed necessary and the selection of the control valve was solely on the basis of its suitability for oxygen service and its fail safe closure characteristics.

Typical operating pressures are shown in the figure with the supply and feedline pressures being 2000 and 1200 psi respectively. The control valve thus imposes an 800 psi pressure drop from the supply which is crucial to operation of the system. With a line pressure of 1200 psi and a combustion pressure of 600 psi the injection nozzles at the



IL-0575a

Figure 17. Simplified Schematic of Oxygen System Used Through Run #20

combustor are aerodynamically choked and prevent combustion pressure excursions from feeding back into the oxygen system. The lines and orifice meter were designed for minimal pressure drop and the orifice meter is dominant in this regard. The line pressure at the injectors can be approximated by subtracting the drop at the orifice meter from the upstream line pressure.

With fixed size injector nozzles as used in the combustor manifold one in fact has only two presettable controls on the system - the initial supply pressure and the supply volume. The oxygen bottles initially have a pressure of approximately 2200psi. By bleeding down full bottles any initial pressure below this value can be achieved. The number of bottles used sets the supply volume with the effect that the more bottles that are used the less the supply pressure will drop during operation. While some testing was performed with fewer bottles, all testing with oxygen when the combustor was fired was conducted with ten bottles which resulted in supply pressure drop of approximately 100psi for a 2 second duration.

Consider now the injector plate in further detail. For isentropic flow the relation between static and stagnation pressure is given as

$$\frac{P}{P_t} = \left(1 + \frac{\gamma-1}{2} M^2\right)^{-\frac{\gamma}{\gamma-1}} \quad (2)$$

where P and P_t are the static and stagnation pressures, respectively, γ is the ratio of specific heats and M is flow Mach number. For aerodynamic choking, M=1 and for diatomic gases γ=1.4. Further identifying the static pressure as the combustor design pressure, P_c, and the feedline pressure as the total pressure, the oxygen injector orifices will be choked if

$$\frac{P_c}{P_t - \Delta P} < 0.528 \quad (3)$$

Neglecting the orifice drop, ΔP, the injectors will be choked if the combustor pressure is less than 633 psi at a feedline pressure of 1200 psi. Conversely for a combustor pressure of 600psi the feedline pressure must be greater than 1136 psi. It should be noted that these conditions depend solely on the specific heat ratio, γ, and are independent of the gas molecular weight being equally valid for oxygen, nitrogen and air.

When choked, the mass flow rate through the nozzles in the injector plate is given

as

$$w = k \frac{PtA}{\sqrt{Tt}} \quad (4)$$

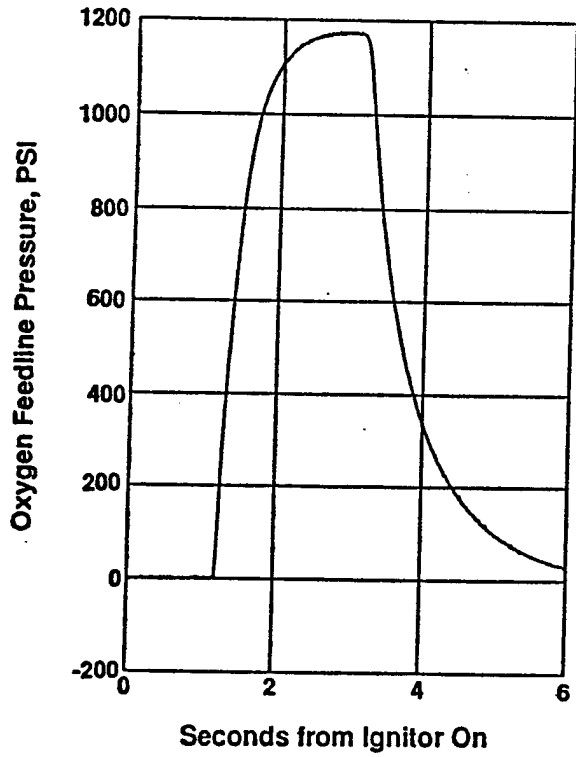
where w is the flow rate in lb/sec., Pt is the total pressure in lb/ft², Tt is the total temperature in °R, A is the combined flow cross sectional area of the six injector nozzles and k is a constant given by

$$k = Cw \sqrt{\frac{\gamma g}{R} \left(\frac{2}{\gamma + 1} \right)^{\frac{\gamma + 1}{\gamma - 1}}} \quad (5)$$

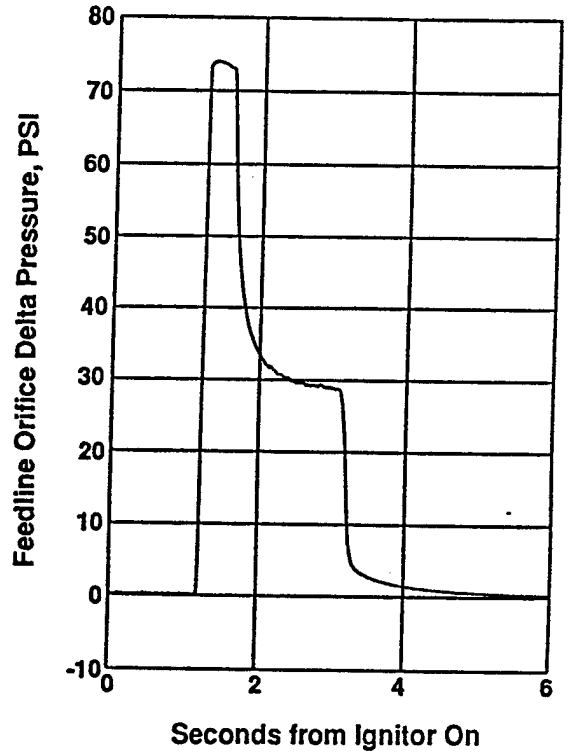
In this expression Cw is the nozzle discharge coefficient, R is the gas constant and γ is the ratio of specific heats. For a discharge coefficient of unity, k has the values of 0.523, 0.559 and 0.532 for nitrogen, oxygen and air respectively. In particular, it should be noted that for safety and prevention of contamination the checkout and calibration of the oxygen system used nitrogen gas exclusively for which different gas constants, R , had to be taken into account.

To initially checkout the oxygen system five tests runs were made using one to ten bottles of nitrogen. Nitrogen was used for safety considerations and necessitated accounting for the different gas constants of the nitrogen test gas and intended oxygen use gas. For these tests the burner was in place, but no fuel grain was installed. Initial tests resulted in disagreement between the calculated mass flows. In particular, the orifice plate data did not agree with loss in bottle weights or injection orifice calculations. The latter, however, were in agreement. The orifice plate inner diameter was reduced from 3.11cm to 2.10cm which resulted in a greater differential pressure drop and closer agreement between the three methods. The initial tests also revealed that the combustor nozzle orifices were sized too small to pass the desired mass flow at the nominal supply pressure of 1200psi. To correct this the injection orifices were increased from the nominal 2.79mm (0.110 in.) to 4.03mm (0.159 in.).

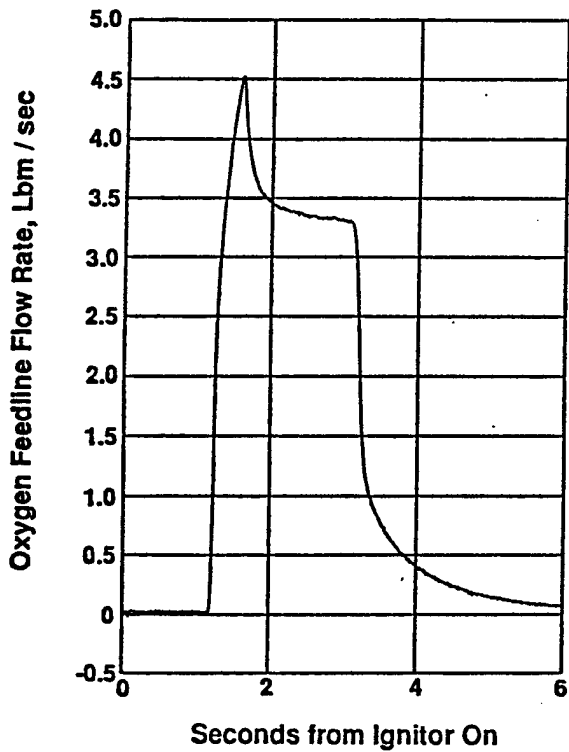
Typical oxygen system flow data are given in Figure 18 which illustrated the measured line pressures and the derived instantaneous flow rates. The particular data is for the second combustor test, Run #10. The initial supply pressure was preset to 2150 psi for this test. In Figure 18a the oxygen feedline pressure is given. For this test the oxygen control valve opening and closure was set at 1 and 3 seconds respectively after the igniter was fired. As observed in Figure 18 there are short delays at both valve



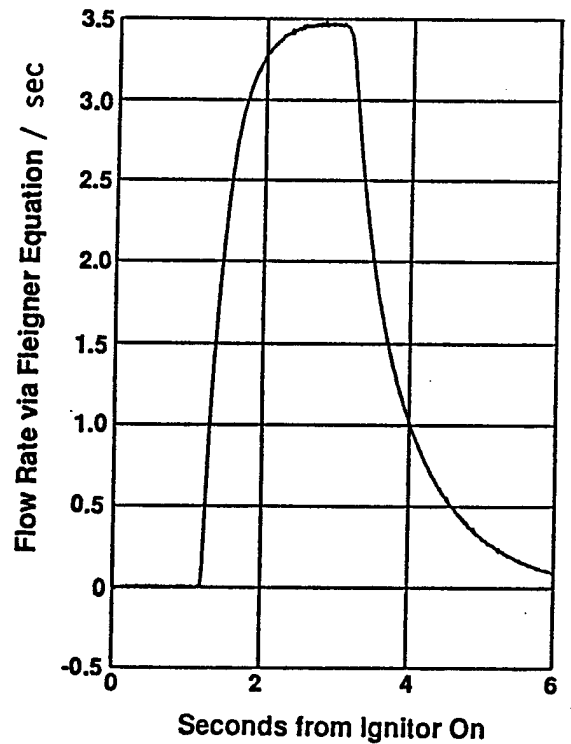
a) Upstream Feedline Pressure, P_1



b) Orifice Differential Pressure, Δp



c) Orifice Measured Flow Rate



d) Aerodynamically Choked Flow Rate

CG-1812

Figure 18. Typical Oxygen System Flow Data for Combustor Run #10.

opening and closure resulting from mechanical inertia of the valve. The feedline pressure in Figure 18a monotonically rises to a near steady value after the valve is opened and drops similarly after valve closure. In contrast, the differential pressure across the orifice meter given in Figure 18b abruptly rises to a high steady value and then monotonically decreases to a near level value after and while the valve is opened. On valve closure an abrupt drop followed by a slower decay results. The initial rise and level peak in Figure 18b indicate that the control valve is initially aerodynamically choked. With the supply pressure initially at 2150 psi it is observed that choking can be expected to occur as long as the line pressure is below 1135 psi. The data indicates that the choking occurs while the line pressure is below approximately 1000 psi. Thus, neglecting the small drop in supply pressure as mass is lost from the volume of the 10 supply bottles, the choking of the control valve establishes an initial constant flow rate for charging the feedline. This initial flow rate limitation also governs the initial rate of rise in the feedline pressure in Figure 18a. Recognizing this, the actual valve movement time from the closed to open position is measured by the rise in Figure 18b, rather than 18a, and is noted to be quite rapid. After the line pressure increases above 1000 psi, the valve unchokes and the pressure differential and mass flow through the orifice meter both decrease toward quasi steady values.

While the feedline charges the orifice meter measures the mass flow through it. However, only a portion of the measured mass flow rate is actually going through the injectors to the combustor during this transient. Thus the orifice meter data is a reliable measure of the oxygen flow to the combustor only when the feedline conditions are quasi steady. The mass flow measurement with an orifice meter is functionally dependent on the product of the line pressure with the square root of the pressure drop across it. In other words the mass flow curve should appear as the product of the curve in 18a multiplied by the square root of the curve in 18b and as given in 18c it indeed does.

On the other hand, with the assumption of aerodynamic choking of the injection nozzles the mass flow rate of oxygen to the combustor is directly proportional to the feedline pressure and the mass flow rate will be the same as Figure 18a except for a scale factor. The oxygen flow rate calculated for choked injectors is given in Figure 18d. In contrast to the orifice meter data, the choked flow mass flow rate is accurate during the transient periods of line charging and discharging as long as the combustor pressure

is less than 52% of the feedline pressure. Comparing the rates calculated near valve closure (3 seconds) in Figures 18c and 18d it is noted that while being close, 3.30 and 3.46 lb/sec respectively, the latter is higher. The rate based on choked orifices was always in general higher than the orifice measured rate and is believed to be the more accurate of the two. The orifice calculation is more error prone since the pressure drop is small (30 psi) which is more prone to measurement error which can be amplified by the square root functional dependence in the calculation of mass flow.

As a gross check, the bottle weights are recorded prior to and after a run to determine the total oxygen consumption. One could integrate the areas under the curves in Figures 18c and 18d to calculate the total mass loss for comparison. Alternately, as was actually done, one can divide the weighed oxygen loss by the time the valve was open to get an average oxygen mass flow rate for comparison. This simpler comparison is shown in Table VI for all of the combustor tests.

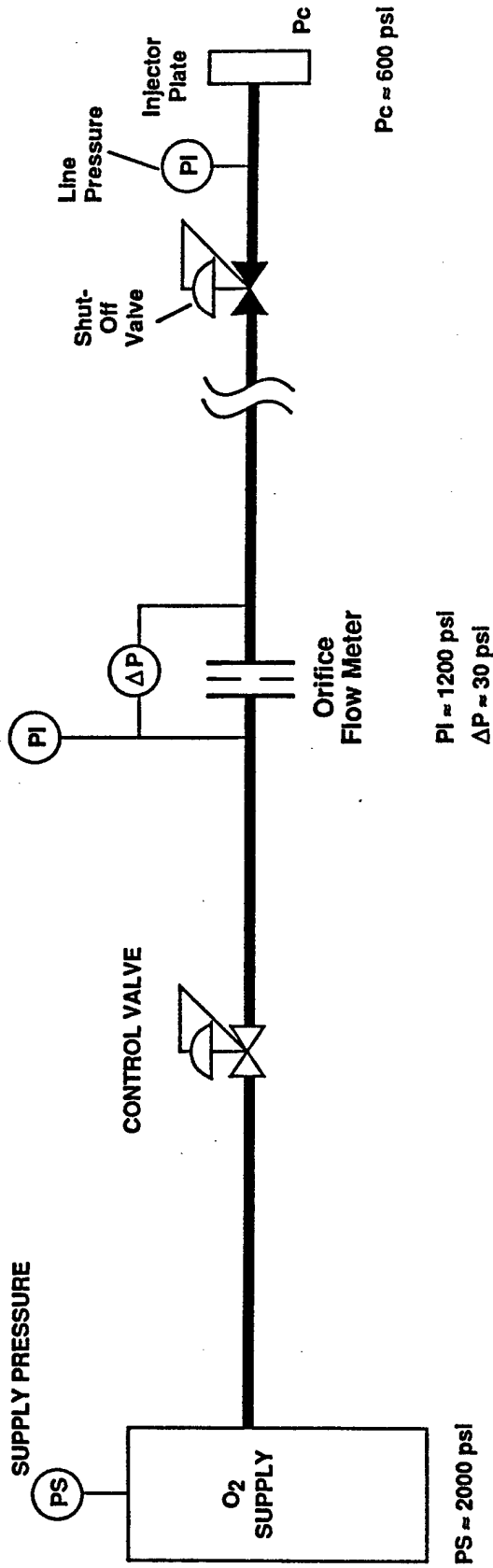
In performing the calculation it is necessary to correct the measured loss in bottle weights for the oxygen trapped in the feedline and manifold at the time of valve closure knowing the line pressure and volume. The thus-corrected weights are given in column 9 in the table rather than the actual bottle loss weights. Note also that in the last two runs, #32 and #35, the injector nozzles may have been unchoked as a consequence of the higher-than-design peak combustor pressures measured.

The oxygen system depicted in Figure 17 was modified after test #20. The modifications are depicted in Figure 19 and were comprised of the addition of a pressure transducer near the actual combustor manifold and a second valve near the combustor. The pressure transducer near the combustor yielded a truer measurement, without correction of the line pressure at the manifold. The valve effectively reduced the line volume involved in the bleed down and pressure decay at the end of a run. This necessitated the additional pressure measurement and shortened the time between valve closure and the onset of nitrogen purge when the feedline pressure decayed to 200 psi. Approximately one second of decay time was saved as indicated in Figure 20 where line pressure data from runs #20 and #35 are compared. In the figure the data for run #20 has been time shifted to the right by 2.0 seconds so that the valve closure events for these two runs coincide.

Table VI. Oxygen System Data for all Combustor Tests

Run #	Valve open time, sec	Supply Pressure, psi		Peak feedline Pressure, psi	Combustor Pressure, psi	Mass flow rate, lb/sec		Corrected O ₂ loss, lbs	Mass flow rate O ₂ loss, lb/sec
		Initial	Final			Orifice meter	Choked Flow		
7	1.38	2300	2200	1274	633	3.44	3.77	5.33	3.86
10	2.00	2150	2080	1171	570	3.30	3.46	6.92	3.46
20	2.00	2190	2090	1077	500	2.94		4.37	2.18
24	1.50	2000	1950	1111	537	3.09	3.30	8.19	5.46
28	1.50	2090	2020	1126	lost	3.28	3.47	14.09	9.39
32	1.50	2100	2050	1135	629*	3.30	3.38	5.15	3.43
35	4.00	2110	1980	1129	617*	3.23	3.36	12.66	3.16

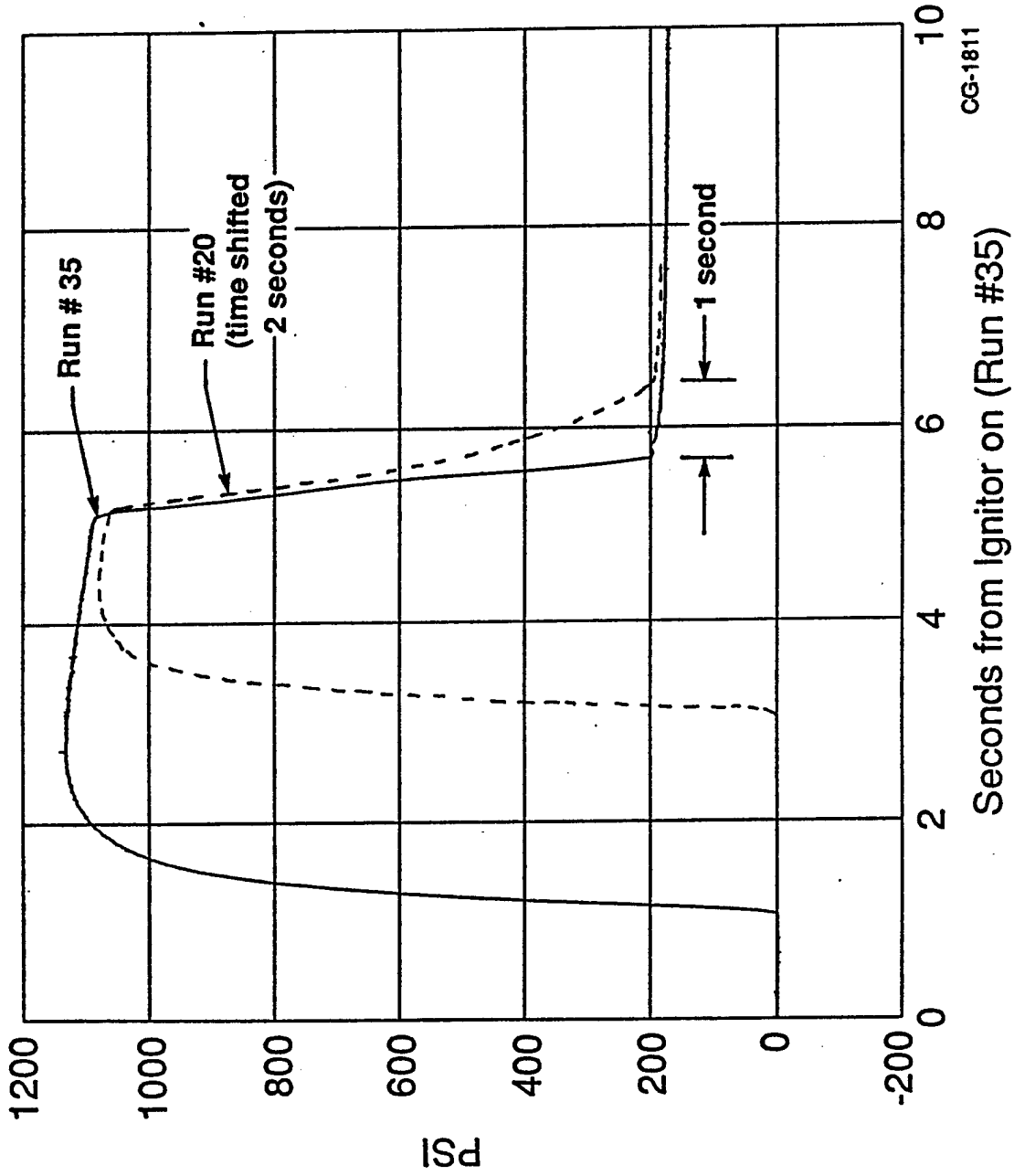
*Unchoked



IL-0575b

Figure 19. Simplified Schematic of Oxygen System Used For and After Combustor Test #24.

Oxygen Feedline Pressure at Combustor SDI TEST RUN 35



CG-1811

Figure 20. Comparison of Oxygen Line Bleed Down Times before and after Downstream Shut Off Valve was Installed.

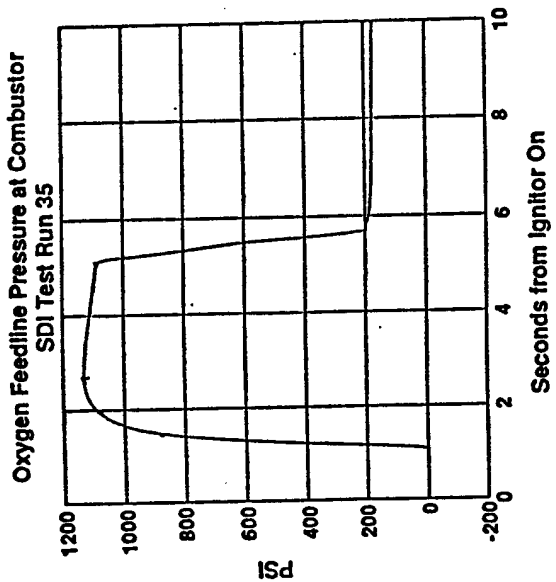
In Figure 21 the oxygen system performance in an extended duration run of 4.0 seconds is shown. In Figure 21a the peak feedline pressure at the combustor is 1129 psi. At this same time the line pressure and orifice meter differential pressures are 1161 and 28.3 psi respectively as given in Figures 21b and 21c. These three pressures are in agreement within a deficit of 3.7 psi which indicates that line pressure drops are indeed small and negligible. At the time of valve closure a line pressure of 600 psi was trapped between the control valve and combustor valve as shown in Figure 21b. This pressure was approximately half the line pressure when the valves were open and it can then be noted that the addition of the second valve reduced the tail off oxygen flow through the combustor to approximately half its prior value before the second valve was installed.

4.2 Igniter Test

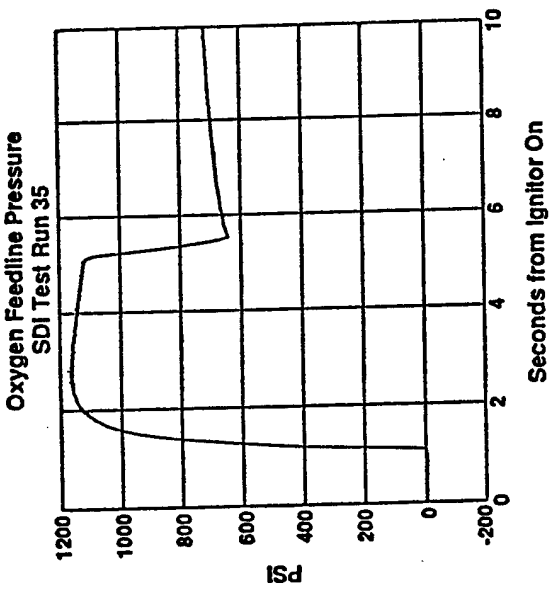
A free air igniter test was performed to witness its operation and verify its desired two second duration. Figure 22 is a photograph of the igniter prior to it firing. The igniter is comprised of a phenolic barrel with a graphite end cap into which six nozzles are drilled. The six nozzles direct the hot igniter gases into the six interspoke cavities of the fuel grain. The igniter uses an electric match for initiating the ignition. Potassium nitrate and boron pellets are in turn ignited by the electric match. The pellets are estimated to burn for approximately 50 msec. and in turn ignite the main propellant charge located on the inside wall of the phenolic barrel.

The photo in Figure 23 shows the flame pattern that results from the igniter. The igniter duration in free air was observed to be approximately 2.5 seconds. Its operation appeared to be reliable and smooth. While particulates appear in the photo, Figure 23, these are believed to be from the propellant. After firing, the graphite nozzle appeared to be in excellent condition with only minor wear in one of the nozzle holes.

Since the igniter propellant contains both fuel and oxidizer, it is in essence a small solid propellant rocket motor. As such, its burning rate should be highly pressure dependent. It is possible that when used in the combustor its duration may be shortened as combustor pressure rises. Thus, the free air test while indicative is not conclusive in this regard. The key is the pressure within the igniter during firing which was not measured. As long as the combustor pressure is sufficiently low to prevent unchoking

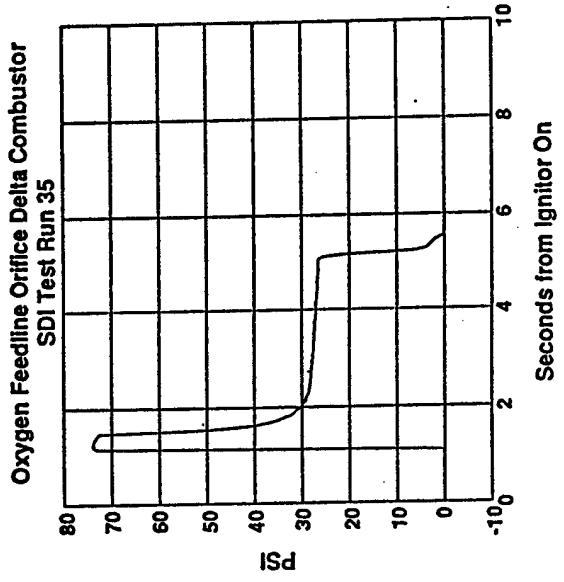


a) Oxygen Feedline Pressure at the Injection Manifold.



b) Oxygen System Feedline Pressure Upstream of the Orifice Meter.

CG-1813



c) Differential Pressure Across the Orifice Meter.

Figure 21. Oxygen System Performance during a Nominal 4.0 Second Duration Run.

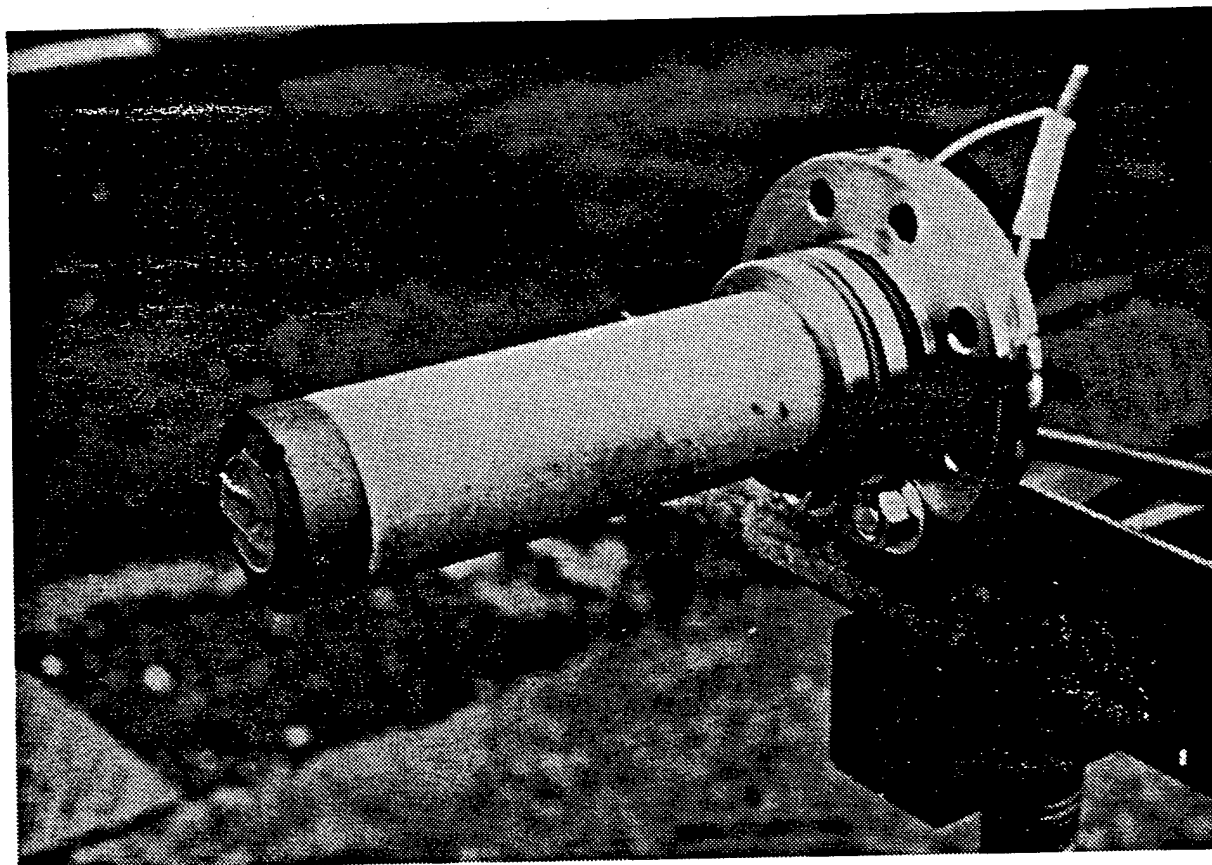


Figure 22. Photograph of Igniter Prior to Free Air Firing Test

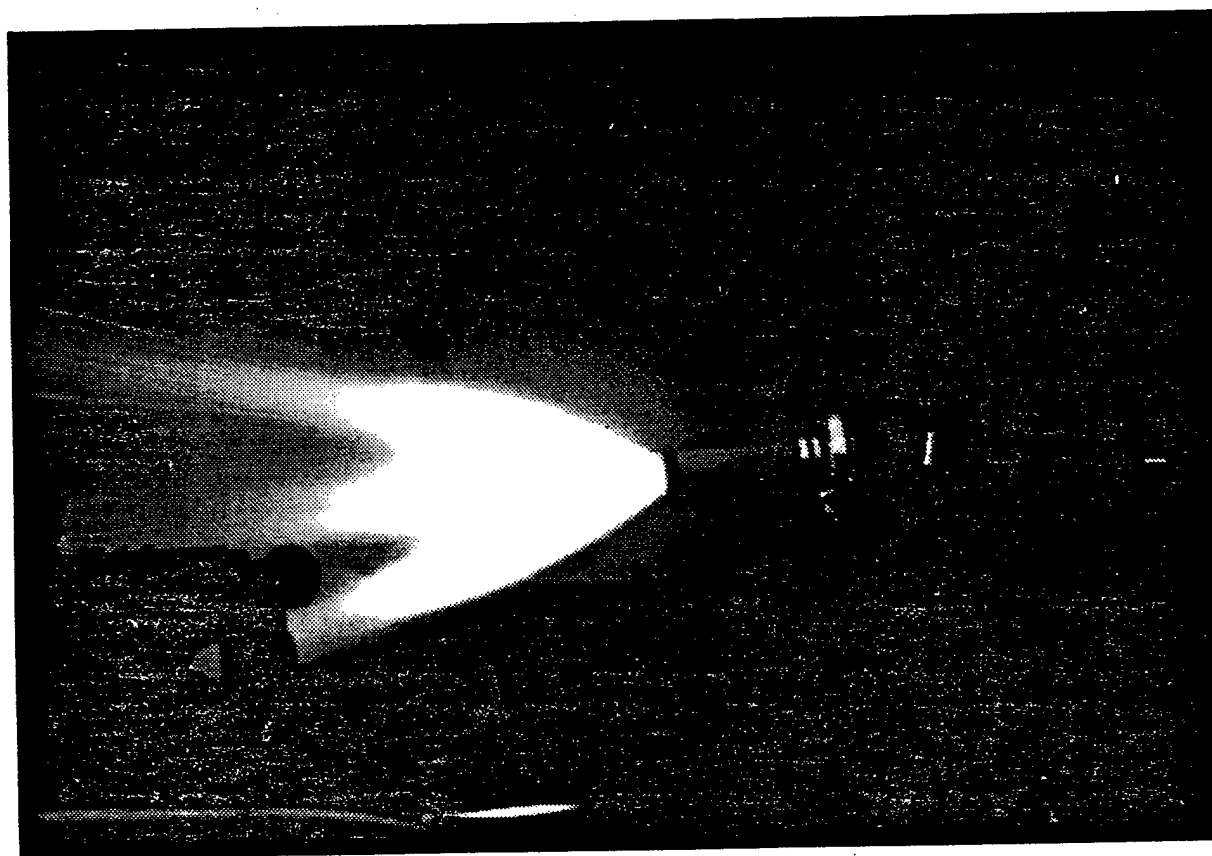


Figure 23. Photograph of Flame Pattern During Free Air Test of Igniter

of the igniter nozzles, the igniter burn rate and flame pattern will essentially be the same as observed in free air. On the other hand, if the combustor imposes a sufficiently high back pressure to unchoke the igniter nozzles the burning rate may be accelerated. For this to happen, however, the combustor fuel grain itself will have to be ignited, and it becomes a moot point.

4.3 Combustor Tests

Seven firings of the combustor using five fuel loads with a cumulative run time of 13.9 seconds were performed during the program. The first three firings were with the combustor and exhaust ducts mounted on the facility floor as shown in the photograph in Figure 24. The fourth firing was performed on a test stand mounted between the open magnet halves with the Faraday configuration channel in the flow train. The last three firings were with the magnet closed about the flow train and energized. The first of the last three firings had the Faraday channel in the flow train while the last two had the diagonal channel in the flow train. The photograph in Figure 25 shows a typical configuration for a powered channel test.

Before proceeding to a discussion of the combustor quantitative test data it is instructive to review the problems, solutions and successes which were encountered during the seven firings. The following paragraphs individually summarize these tests by test number. All facility testing was identified by a sequential numbering system which included oxidizer system check out initially and prior to each run. As a consequence the resulting firing tests bear sequential but nonuniformly increasing numerical designations.

4.3.1 Combustor Test - Run #7

The initial firing, designated test Run #7, was performed with the configuration as depicted in Figure 24. This was a planned 3-second test but automatically terminated at 1.38 seconds into the run when the innerface of the oxygen manifold was burned up. This in turn, allowed the oxygen feedline to dump into the combustor, resulting in an over pressure which was sensed and precipitated the shutdown. In addition to this failure, the seal on the electric match leads of the igniter failed as soon as the combustor came up to pressure, resulting in a supersonic jet out of the backside of igniter. This jet impinged on strain relief loop of the combustor pressure sensing line (see Figure 24) and resulted in a loss of signal late in the run. These two failures were unrelated and the latter did not

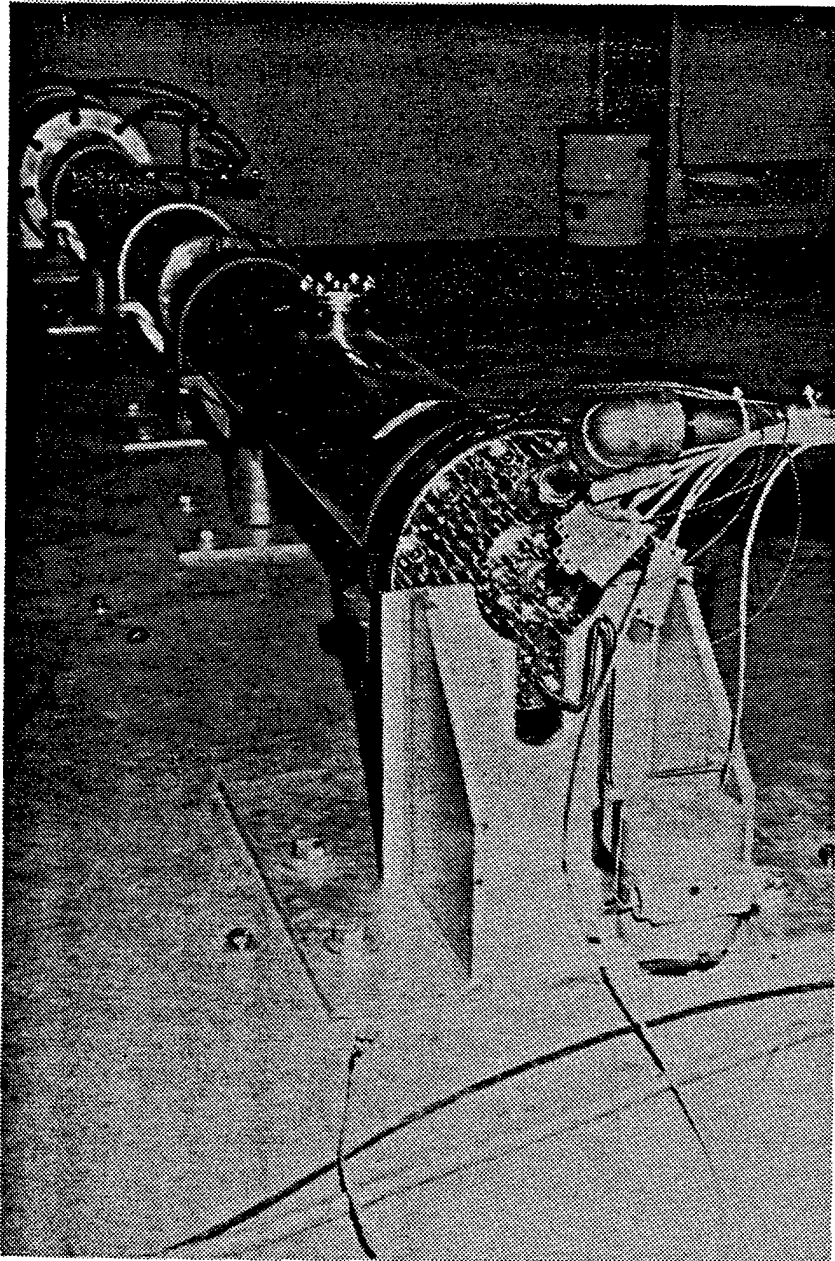


Figure 24. Floor Mounting of Combustor for Combustor Tests #9, 10, and 20

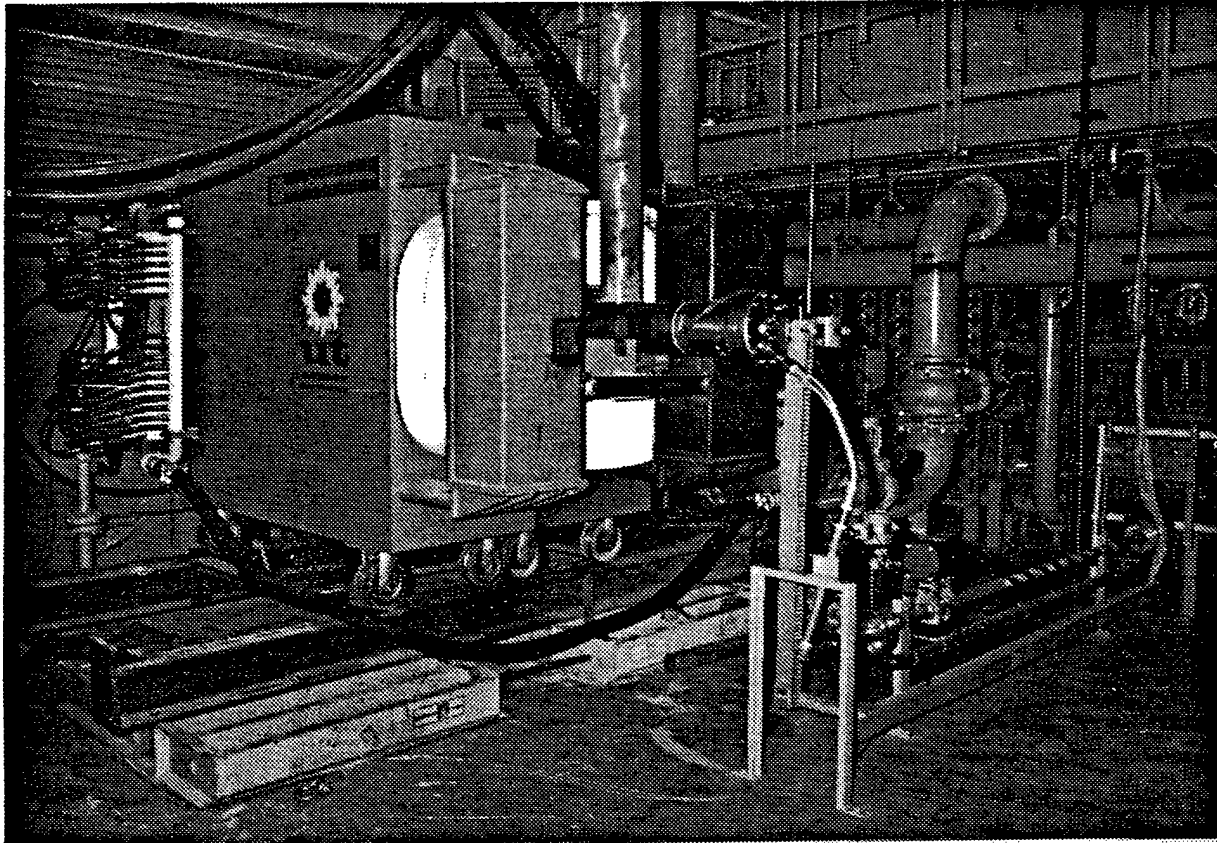


Figure 25. Photograph of Flow Train Configuration for Powered Generator Testing

precipitate the former.

The sequence of events can be clearly seen in Figures 26, 27 and 28 which show the oxygen feedline pressure, oxygen flow rate and the combustor pressure respectively. In the figures key event times are depicted. All times are referenced to the igniter match firing. The oxygen valve is opened after a one second delay from the match ignition. As indicated in Figures 26 and 27 a short additional delay is incurred before one actually senses a rise in the line pressure and flow rate. An additional delay incurred before the combustor pressure rises as noted by comparing Figure 28 with 26 and 27.

The combustor pressure and oxygen feedline pressure monotonically increase in a normal manner while the flow rate increases and then decreases as the line charges as discussed in Section 4.1. The traces appear normal until event t_2 in the figures occurs. At this point a glitch occurs in which feedline pressure increases, drops and recovers while the oxygen flow and chamber pressure drop, increase and recover. Since the injection nozzles are aerodynamically choked, the source of the glitch is in the oxygen feed system and it appears that a partial blockage of one of the six nozzles occurred with a machining chip or foreign particle which subsequently cleared. Normality was reestablished until time t_3 at which time the oxygen manifold cover was lost as signified by a rapid drop in feedline pressure accompanied by increases in the oxygen flow rate and combustion pressure. As the combustion pressure rose through 700 psi the computer control system sensed the abnormality and initiated the shutdown with a closure of the oxygen valve. At event t_4 in the figures as the feedline dumps oxygen through the combustor, the combustor pressure/sensing line is severed by the leak through the igniter and the transducer correctly reads room pressure for approximately .25sec before the signal becomes erratic consequential to burning of the signal wires. Unrelated leakage of hot gas through the thermocouple wire lead out in the nozzle shell also resulted in loss of data but no damage. As indicated in Figure 28 the initial firing did achieve the nominal combustion pressure and oxygen flow rate for approximately 0.5 seconds before the failure.

Post test inspection revealed that the low density insulator, shown in Figure 9, was consumed in its entirety during the firing which led to the manifold failure. The failed manifold is shown in the photograph in Figure 29. The oxygen inlet is at the top and the

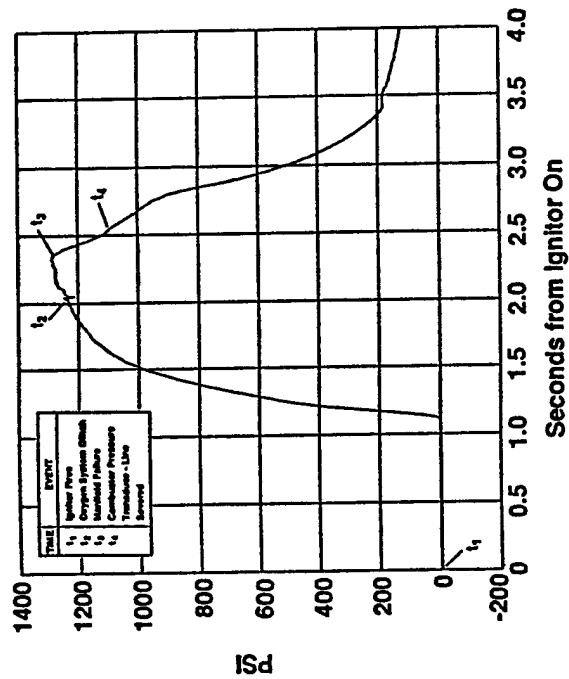


Figure 26. Oxygen Feedline Pressure during Combustor Run #7.

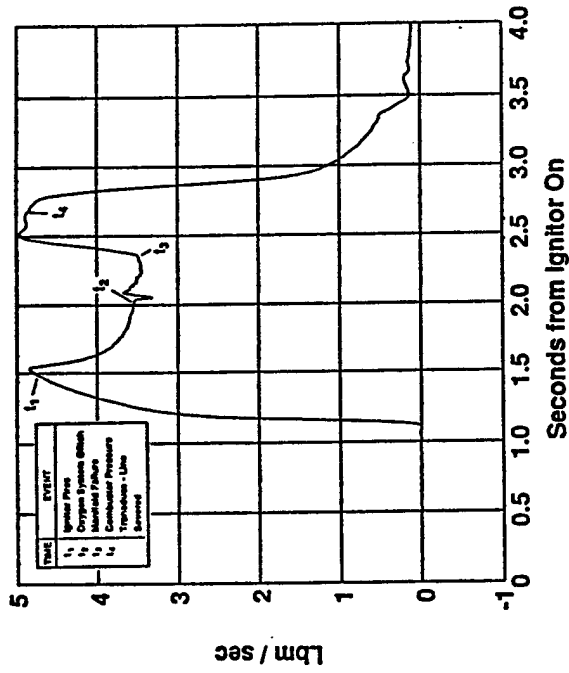


Figure 27. Oxygen Flowrate during Combustor Run #7.

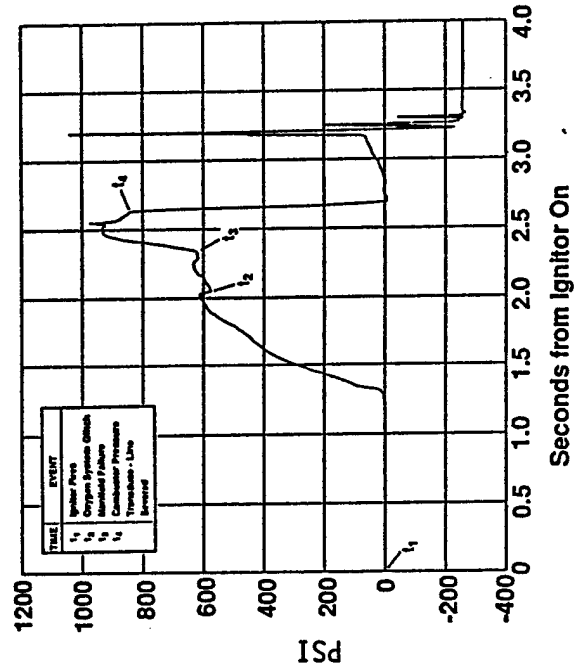


Figure 28. Combustor Pressure during Combustor Run #7.

CG-1820

combustor pressure port is at the bottom in the figure. As the photo shows a communicating path between the manifold and pressure port developed but the damage does not indicate that it precipitated the failure. This in conjunction with the combustor pressure data previously presented suggests that the igniter failure, which severed the pressure line and led to hot gases flowing out the pressure port opening, and the manifold failure were unrelated events. The igniter assembly was lost except for the metal flange which is shown in Figure 30 with the view looking at the combustor side of this flange. In the photo, the debris at the bottom, where the phenolic barrel would normally be, is deposited slag rather than damage. This slag probably came from erosion of the edge which was initially flat but eroded with an inside chamfer as shown in the photo. Again by observing the damage to the manifold cover in Figure 29 with the igniter damage, there does not appear to be any preferential damage indicative of the igniter failure triggering the manifold failure.

The loss of the insulating disk resulted in a 2.2 cm gap between the end of the fuel grain and the manifold cover (see Figure 9). This gap resulted in a hot gas path to the pressure relief port through the kaowool insulation between the fuel grain and the combustor shell. While a significant quantity of the kaowool was burned only superficial damage to the outside of the fuel grain and inside of the combustor shell resulted. The latter was in turn confined to the end position of the fuel grain directly under the heavy flange.

In addition to the achievement of desired combustion pressure, the initial test demonstrated a quite uniform recession of the fuel grain. In Figure 31, a photograph of the third fuel grain section after this firing is shown. The circular cut out in the outer shell is the hole under the pressure relief port which locates this fuel section midway along the length of the grain. The spokes in the fuel grain are all quite uniform and the spoke tips, which are initially small flats approximately 0.6 cm across appear more pointed.

4.3.2 Combustor Test - Run #10

For the second combustor firing, Run #10, a new combustor end flange, 1/4 inch thicker with the interior oxygen manifold corresponding further recessed, was used. An ATJ graphite disk replaced the low density ceramic insulator lost during the first firing. A new first section (oxygen injector end) fuel grain was mated with the three other

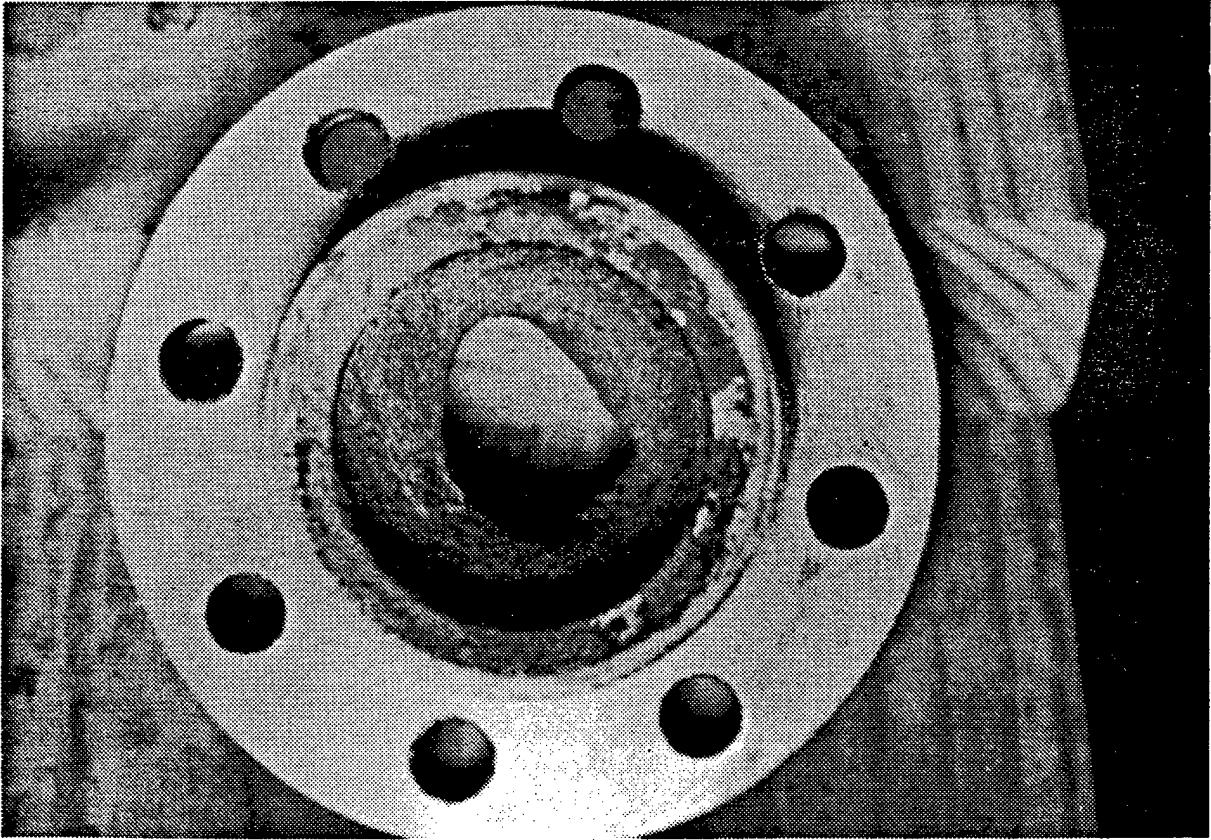


Figure 29. Photograph of the Damaged Oxygen Injection Manifold After First Firing

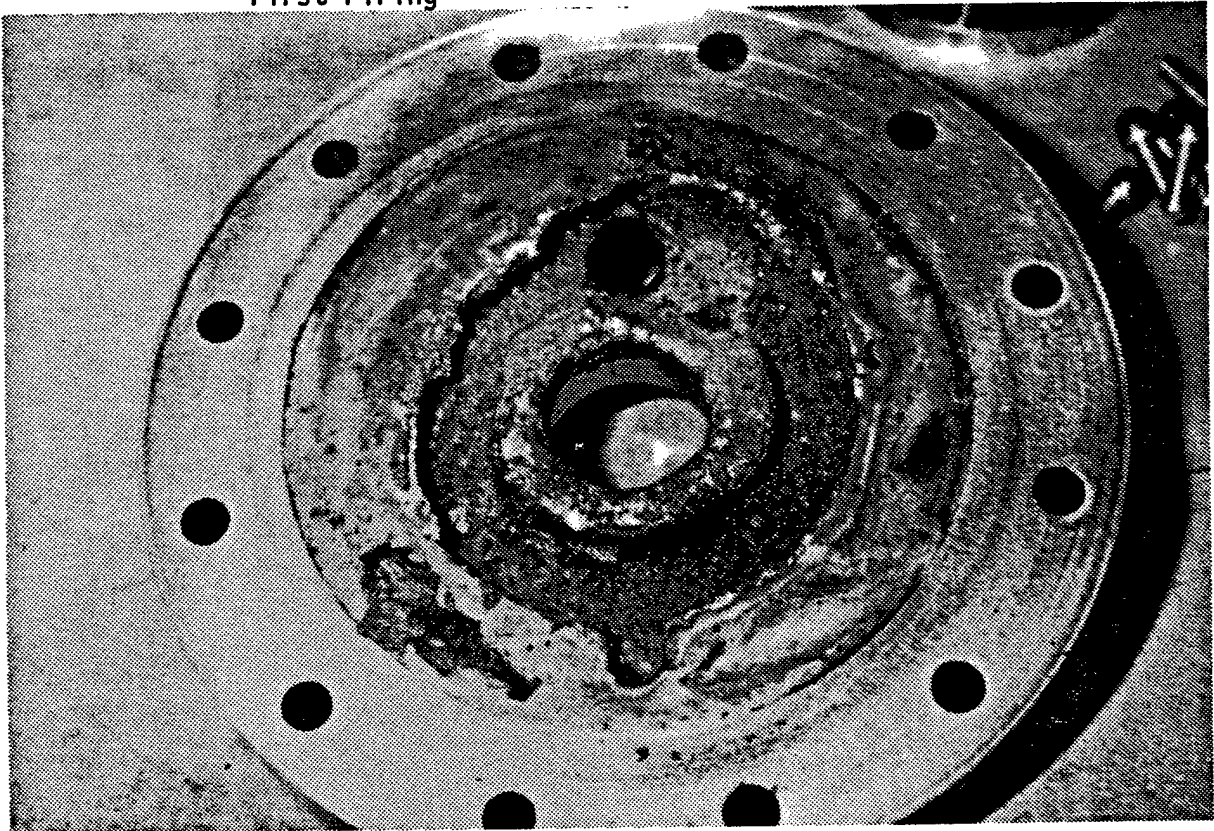


Figure 30. Photograph Showing Damage to Igniter. View is of the Combustor End of the Igniter Looking Outward



Figure 31. Photograph of Center Fuel Grain Section After First Combustor Firing

sections previously used in the first test. A new electric match lead out seal using a compressed elastomer seal around the leads was used on the igniter. This planned two second firing went full duration with no observed leakage of hot gas to the exterior of the igniter or the nozzle thermocouple lead penetration. Failure to precharge the nitrogen purge lines before the run resulted in no automatic purge at the end of the run. The delay in purge which was manually effected a short time after the run was over had no adverse effect and in fact provided a useful data point for comparison with runs which normally had purge after the run. Near design combustion conditions were again observed.

Post test inspection revealed that the internal igniter parts: the nozzle, the phenolic shell, and the center post with nozzle attachment screw, were all lost back to igniter attaching flange. Hot gas blow back was evidenced at the pressure relief port with some kaowool insulation burnt between the fuel grain and inner combustor wall. The graphite nozzle again appeared to be in excellent shape following the firing.

This test demonstrated the ability and ease of reignition of a partially used fuel grain as the downstream three sections had previously been used. The fuel grain appeared to be in good condition and was not removed from the combustor after the test.

4.3.3 Combustor Test - Run #20

The third combustor firing, Run #20, was a test designated to verify a new igniter design. It was clear that the exposed igniter components were being consumed and they required thermal protection. To accomplish this the igniter was moved back out of the combustor such that only the graphite nozzle at the end of the igniter projected beyond the graphite insulating disk at the injector head. The same fuel grain was used again and a 1.5 second planned duration run was completed. Again uniform recession of the fuel grain was observed and is shown in the photograph in Figure 32. The igniter assembly survived but the first section of the fuel grain which had been run once before was pocketed. These pockets formed where the oxygen inlet jets impinge on the igniter jets. The relevant geometry of the igniter jets and the oxygen jets can be envisioned by considering Figure 23 and imagining the oxygen jets to emanate from a plane initially located at the base of igniter nozzle. By solving the igniter problem the jet interactions were made much stronger which formed the pockets in first section fuel grain. The

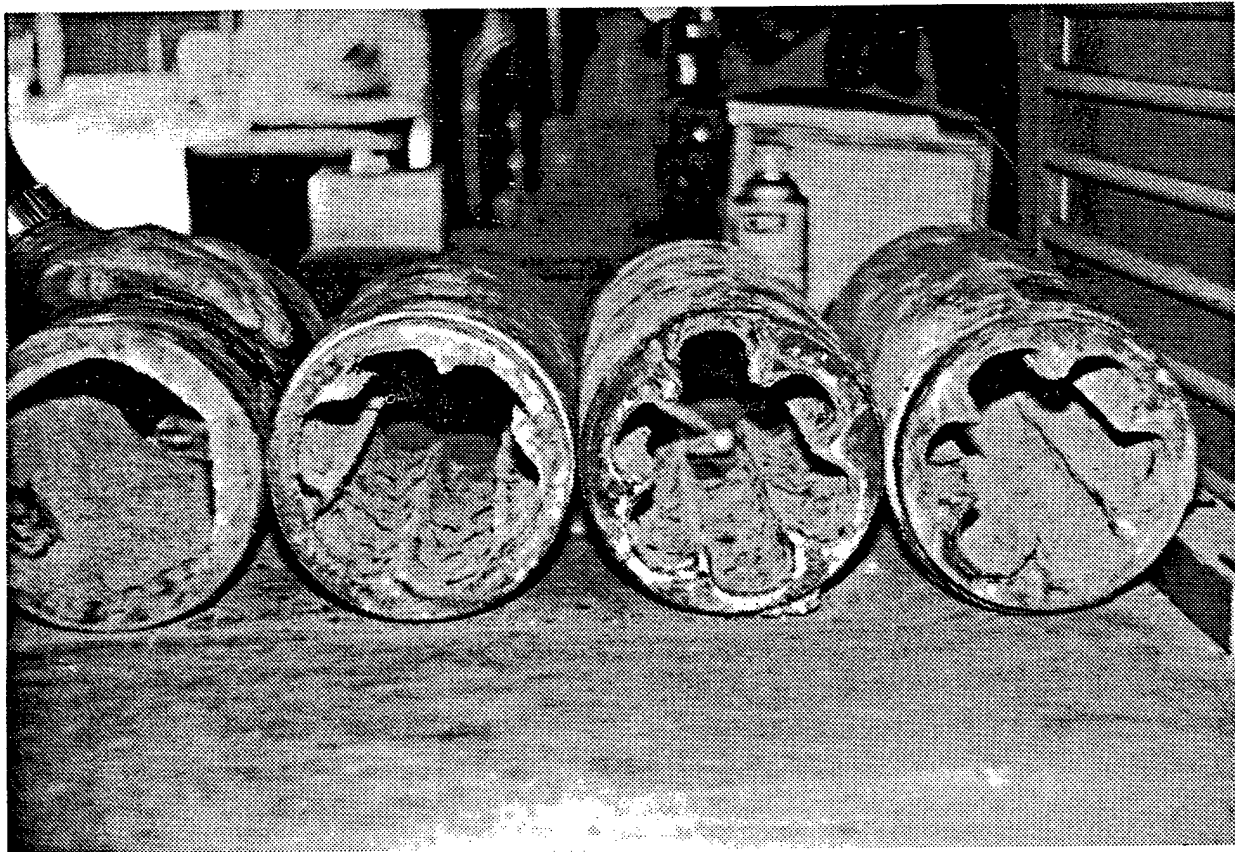


Figure 32. Fuel Grain Sections After Run #20 Showing Uniformity of Wear

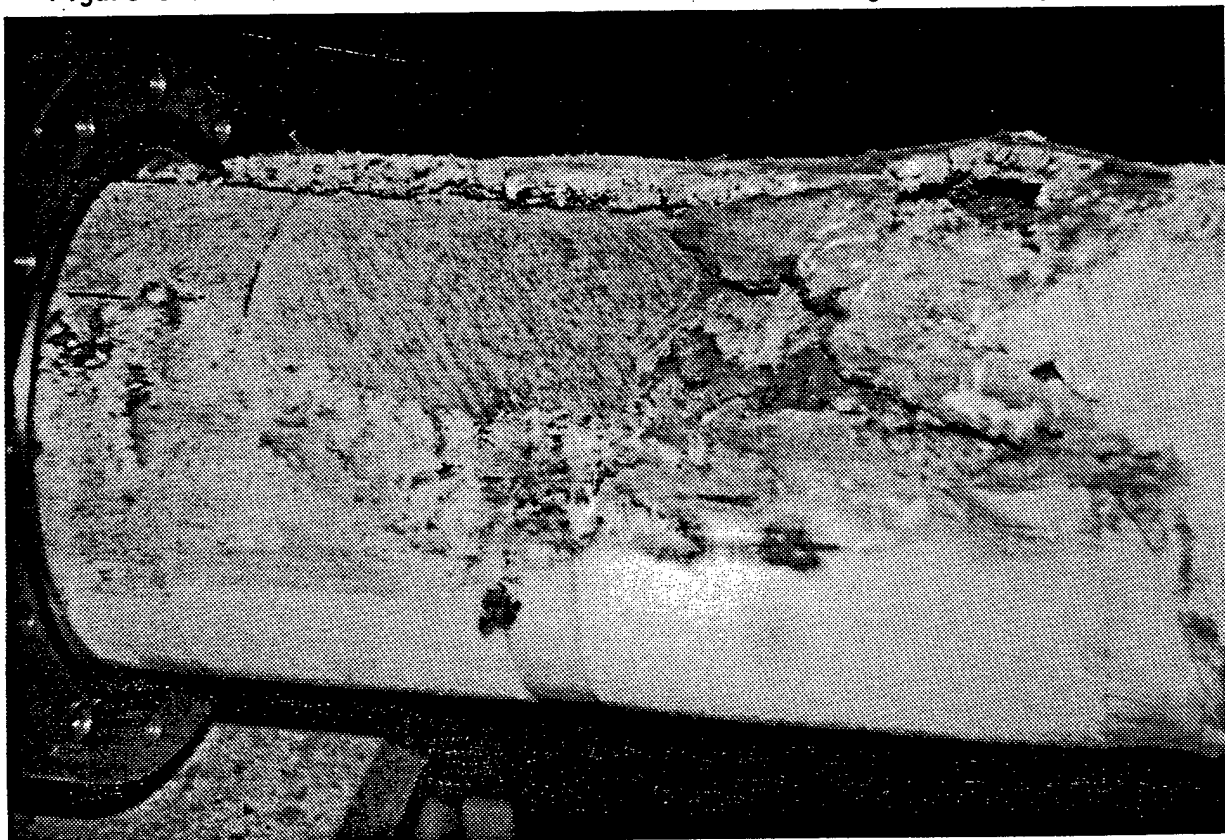


Figure 33. Photo Showing Insulation Damage Resulting from Blowby at Pressure Relief Port

pockets went all the way to the outer fiber glass shell of the fuel grain but did not compromise it. Again, hot gas blowby in the vicinity of the pressure relief port was evidenced when the grain was removed from the combustor. Figure 33 is a typical example of such damage and loss of the insulating kaowool.

4.3.4 Combustor Test - Run #24

The fourth combustor test, Run #24, was performed to thermally test the Faraday channel prior to its powered testing. A fresh fuel grain was used for this test and silicone rubber gaskets were installed on either side of the graphite disc to prevent backflow between the outer surface of the fuel grain and inner combustor wall.

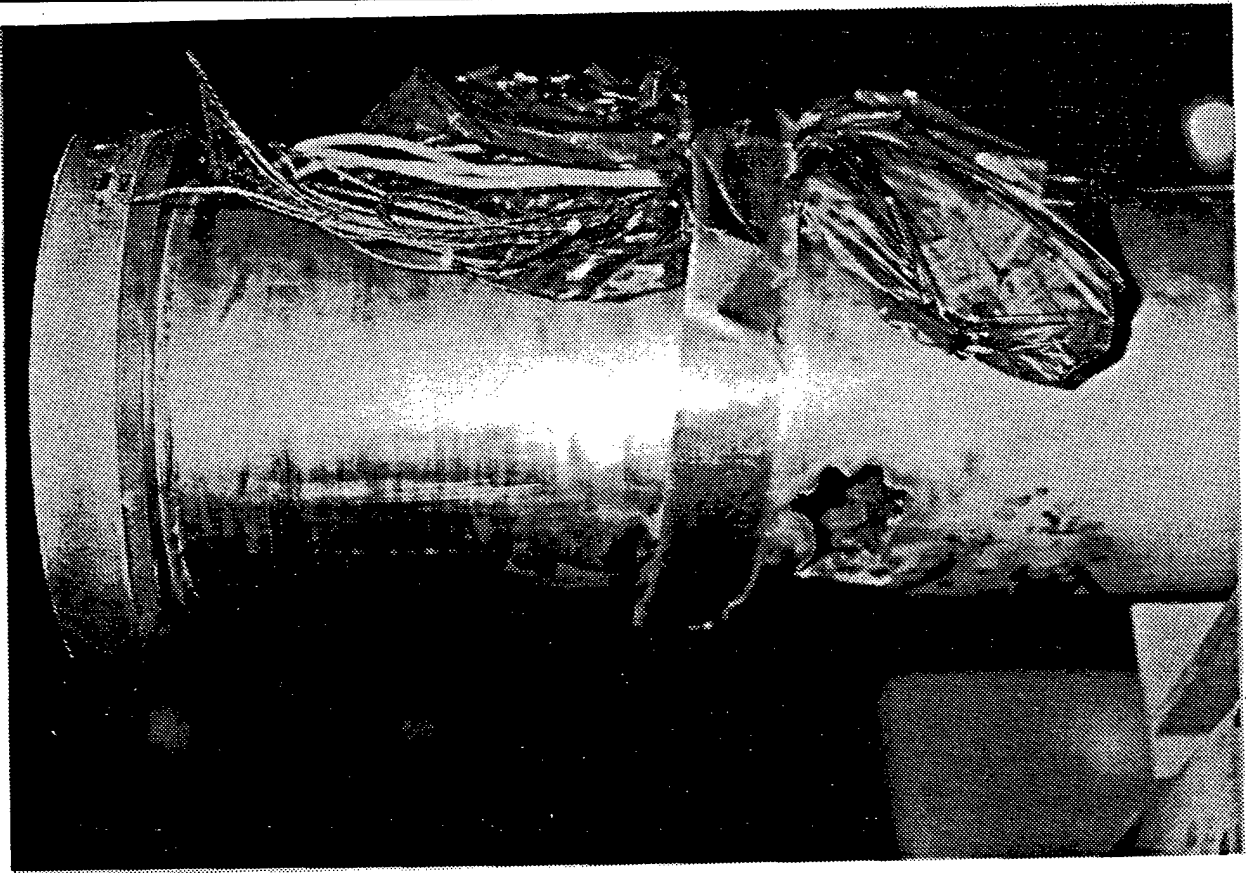
During this test, a dramatic and unexpected failure of the combustor barrel occurred near the end of the planned duration run. An extremely rapid, almost explosive, burn through of the combustor occurred at the junction of the first and second fuel grain sections. Figure 34 shows the combustor damage. In this photo, the hole burned through the combustor shell is visible. It is clearly evident that burning of the stainless steel with oxygen occurred, as if a cutting torch had been used.

The combustor failure appeared to be related to defects in the form of voids within the fuel grain as shown in Figures 35 and 36. In Figure 35 the burn through at mating surface of the fuel grain is shown while in Figure 36 the fuel grain, with its fiberglass case removed, is presented. Figure 36 shows a void that progressed to the case but did not penetrate it. Cracks in other fuel grain sections which occurred in the fuel casting but not in the fiberglass shell were also observed and are shown in Figure 37.

Figure 38 shows typical joints used with the fiberglass liner of the combustor. The fiberglass joint used with the fuel grain for Run #24 was a butt joint. The fuel itself had a lap joint between sections (that is the fiberglass overlapped the fuel) but the fiberglass was not lapped (Figure 38b). Previously used grain joints used fiberglass lap joints as well as shown in Figure 38a.

4.3.5 Generator Test - Run #28

The fifth test, Run #28 was conducted to measure Faraday channel power. For this test a fresh fuel grain with a modified joint design was used. The joint design, shown in Figure 38c, was comprised of a double lap joint of the fiberglass outer fuel liner with



a) Location



b) Detail

Figure 34. Photo of Combustor Burn Through at Joint Between 1st and 2nd Fuel Grain Sections During Run #24



Figure 35. Photograph of Fuel Grain Burn Through at the Joint with the Outer Fiberglass Casing Removed

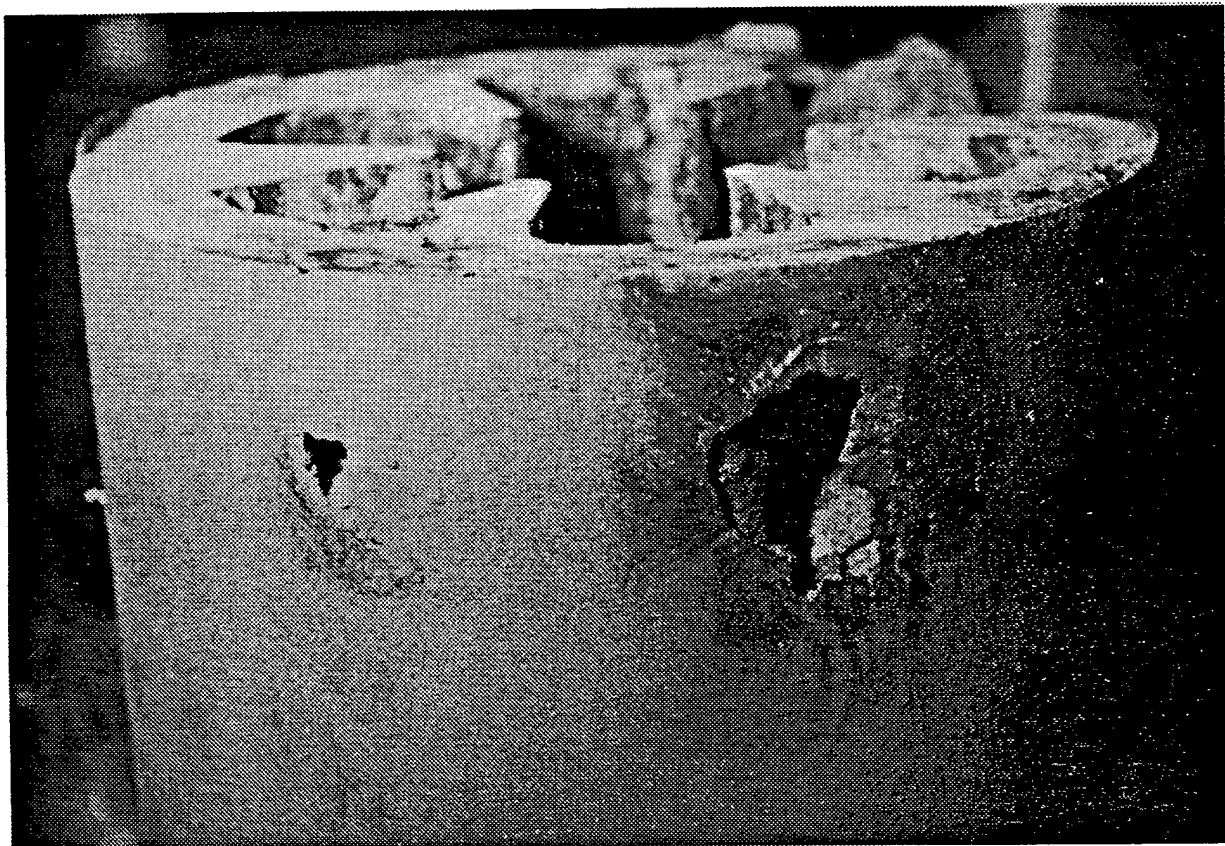
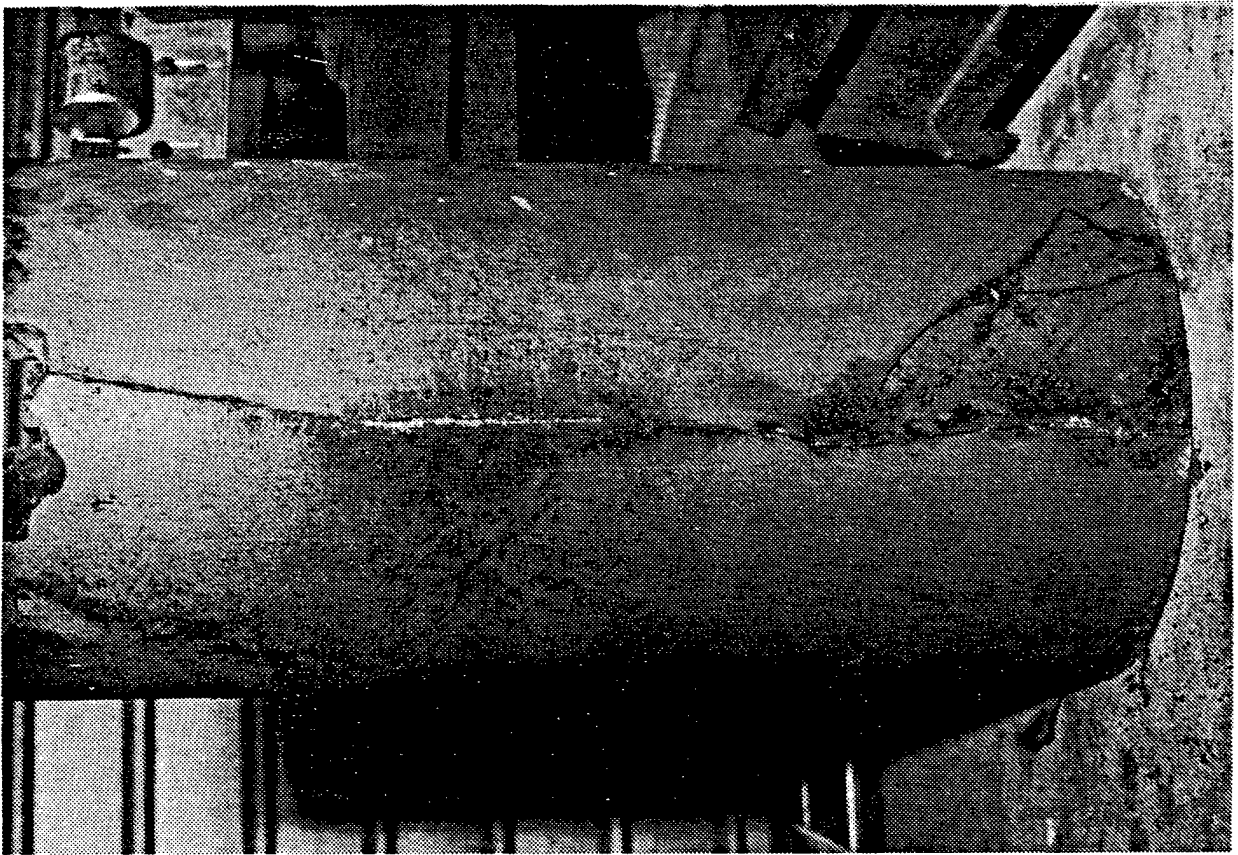
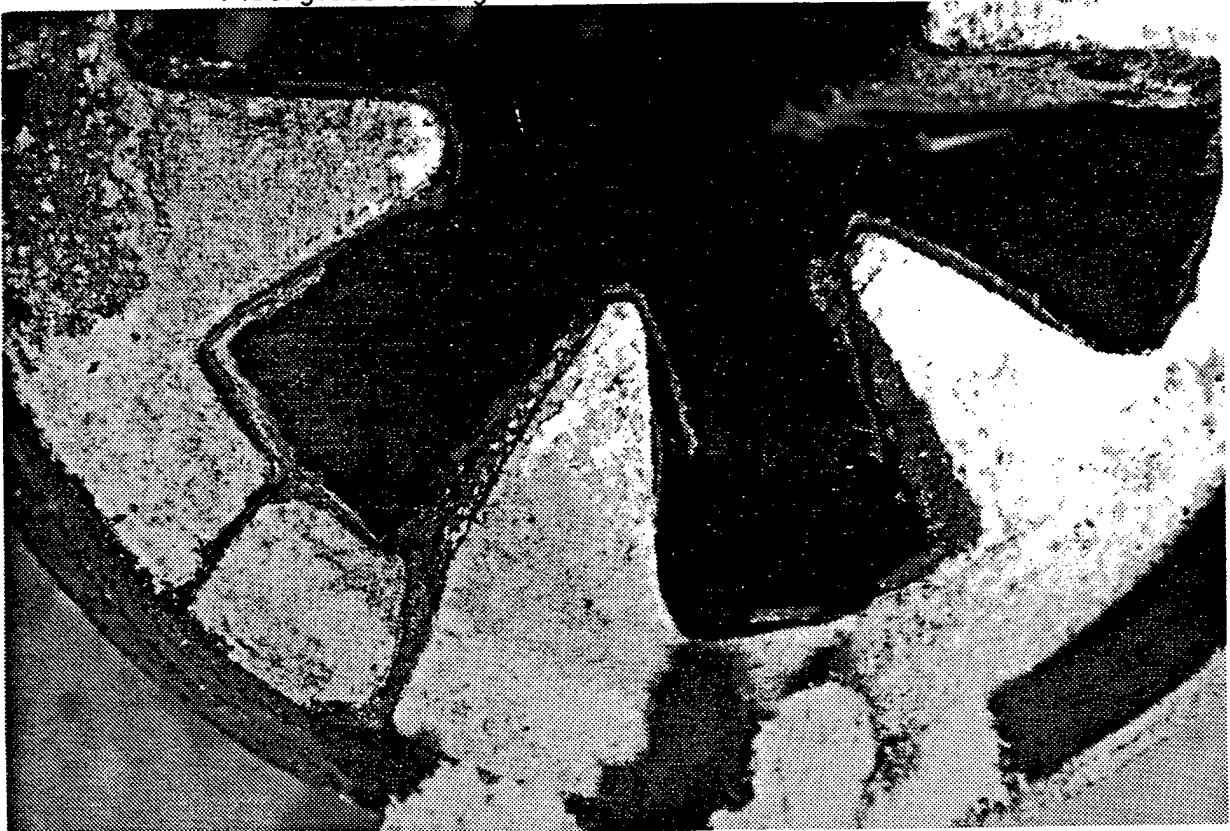


Figure 36. Photograph of the Fuel Grain with the Outer Fiberglass Casing Removed which shows additional voids which did not penetrate the casing.



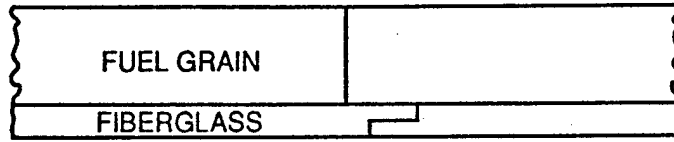
a) Longitudinal cracks in Fuel Grain Section #2 with Outer Fiberglass Casing Removed



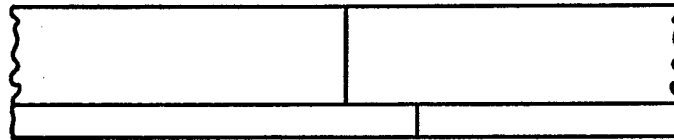
b) Cracks Evidenced in Fuel Grain Section #4 Following Test #24

Figure 37. Fuel Grain Cracks Following Combustor Test #24

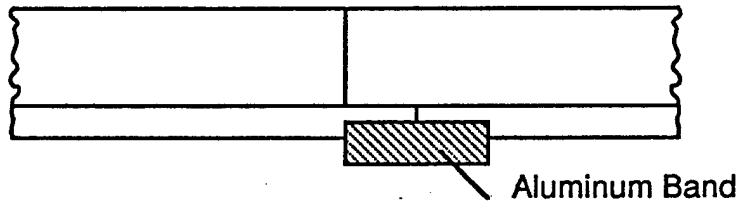
(A) FIBERGLASS LAP JOINT



(B) FIBERGLASS BUTT JOINT



(C) FIBERGLASS DOUBLE LAP JOINT



(D) FIBERGLASS DOUBLE LAP JOINT

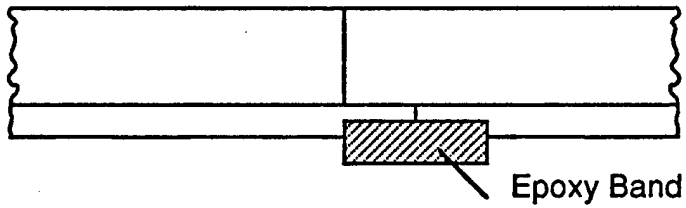


Fig. 38 Sketches of Various Fuel Grain Joints Used

IL-0870

an aluminum band. The joints were all epoxied at the time of assembly. The firing progressed as planned, however, blowby at the pressure relief port was evidenced. Approximately four inches of the aluminum band at the joint located under the port was consumed. Again loss of the kaowool insulator around the port and along the top of the fuel grain occurred. The burn path did not progress all the way to either end of the fuel grain.

Shallow pockets in the first section fuel grain were again seen in post test inspection. These appeared to result from the oxidizer igniter jet impingement. The consumption of the aluminum band under the pressure relief port resulted in the outer shell being very hot to the touch after the run. Nozzle erosion was again minimal. Combustor pressure data was lost during the run due to faulty wiring.

4.3.6 Generator Test - Run #32

The sixth test, Run #32, was a 1.5 second power test of the DCW generator channel and was also conducted with a fresh fuel grain. The aluminum bands were replaced with a fiberglass reinforced epoxy band. Essentially, the sections were fiberglassed together. Since combustor pressure is monitored for safety a redundant transducer was installed to preclude the total loss of data as was experienced on the prior firing. This firing lasted for its intended duration. Post test inspection of the combustor showed evidence that again blowby at the pressure relief port had occurred. Also, it was evident that blowby was present at the oxidizer injection end of the fuel grain. The latter occurred between the end of the fuel grain and the graphite thermal protective disk taking some of the silicone rubber gasket with it. The graphite disk showed no radial erosion. However, the end of the fuel grain did. After the run the combustor barrel temperature near the relief port appeared warm but considerably cooler than in the previous run.

4.3.7 Generator Test - Run #35

The seventh and final test of program, designated Run #35, was an extended duration repetition of Run #32. The DCW channel was used in the flow train, the magnet was powered and a fresh fuel load was used for the test. It differed from Test #32 only in that its intended duration was 4 seconds. The goal was to heat the inside wall of the generator as hot as possible without thermally destroying the potting material in the generator. The firing went its intended duration with no hardware problems encountered.

The oxygen feedline pressure, oxygen mass flowrate and combustion pressure traces for this run are given in Figures 21, 39, and 40 respectively. An anomaly in the combustor pressure was observed that was not evidenced in the shorter runs. The anomaly is a low frequency (approximately 6hz) oscillation which also appeared as a change in the luminosity of the exhaust gas in a frame by frame examination of the videotape. From the luminosity variation it could also be inferred that the combustion equivalence ratio and the fuel grain decomposition were unsteady as well. It is not known whether this is an acoustic phenomena of the combustor or not. Again desired combustion pressure was achieved.

As a consequence of the extended duration, temperatures recorded on the flow train were generally higher than observed before but all within tolerable bounds. The temperature of the combustor shell near the pressure relief port in particular remained within previously seen ranges indicating that the problems with hot gases in this area are not a flow problem per se but rather confined to the initial pressurization when infusion into the kaowool occurs.

Post test inspection of the combustor revealed it to be in good, reusable shape. The igniter survived as shown in Figure 41 but the head of the igniter nozzle retaining screw was burned away. The oxygen manifold insulating disk was cracked but intact with no significant erosion evidenced on it. The pockets in the fuel grain had burned all the way to the fiberglass fuel liner. While significant areas of the liner were exposed as shown in Figure 42, the liner was not compromised. Fuel grain recession again appeared quite uniform along its length.

To qualitatively summarize all the combustor tests, overall the combustor has performed very well with repeatable performance demonstrated. That is to say that its ignition was predictably reliable, the ramp up of the combustion pressure was fairly uniform, termination of combustion was smooth etc. The combustor had one notable shortcoming in that excess fuel consumption was observed as will be considered further in section 4.3.8. In this same regard the problems of the ignitor loss and fuel grain joint integrity were solved, though not optimally, but the problem of damaging the insulation between the fuel grain and combustor shell was never completely solved. Two unexpected surprises that resulted were that the nozzle erosion which had been

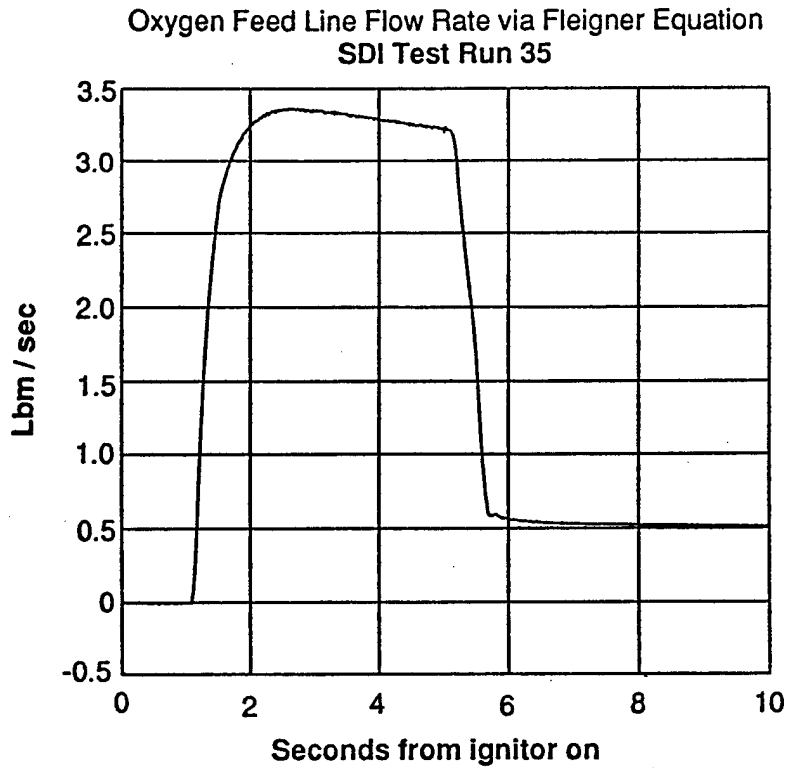


Figure 39. Oxygen Mass Flow Rate During Extended Duration Run #35.

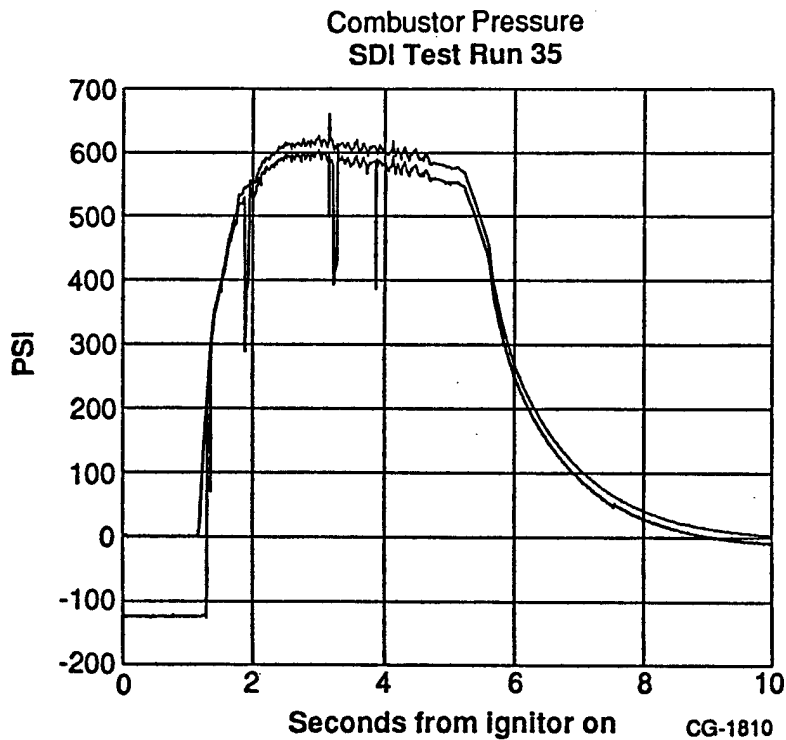


Figure 40. Combustor Pressure During Extended Duration Run #35.
Note use of redundant transducers one of which read only intermittently particularly at the start of the test.

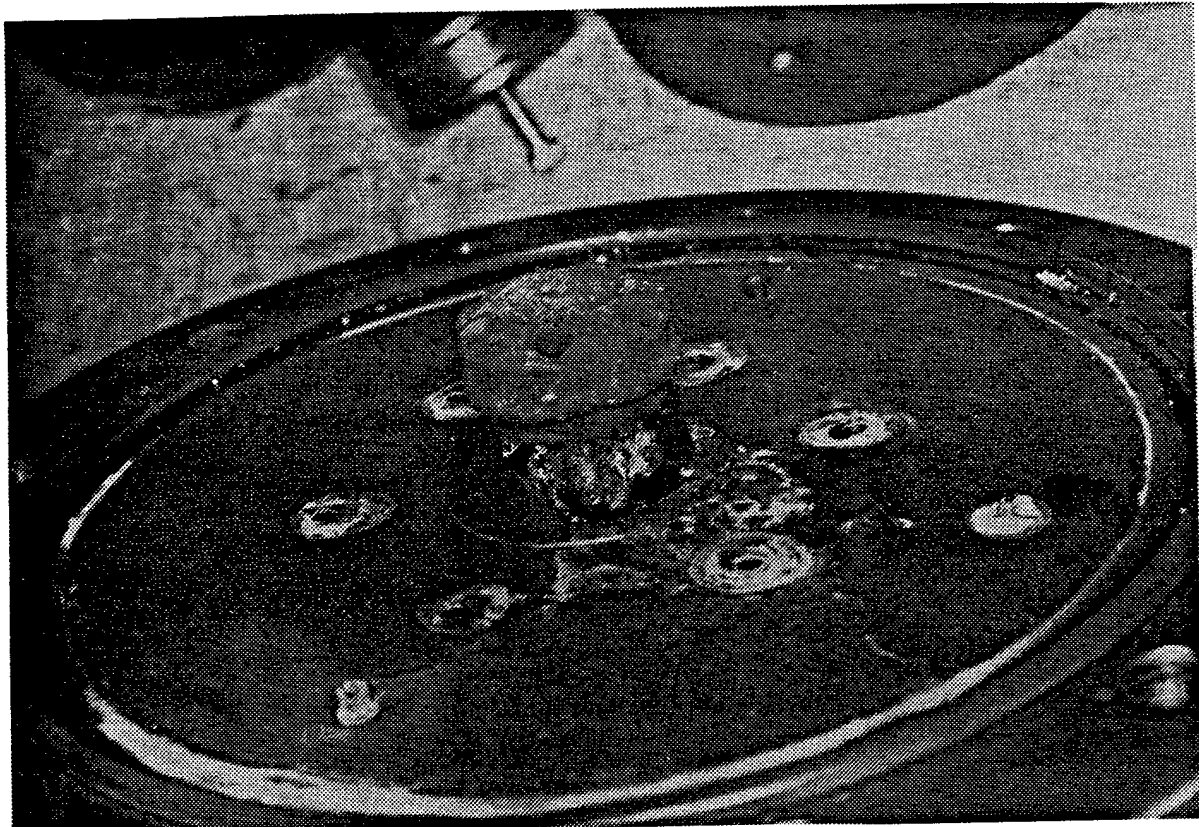


Figure 41. Photograph of Igniter Nozzle After Extended Duration Test #35. The graphite insulating disk is removed in the photo.

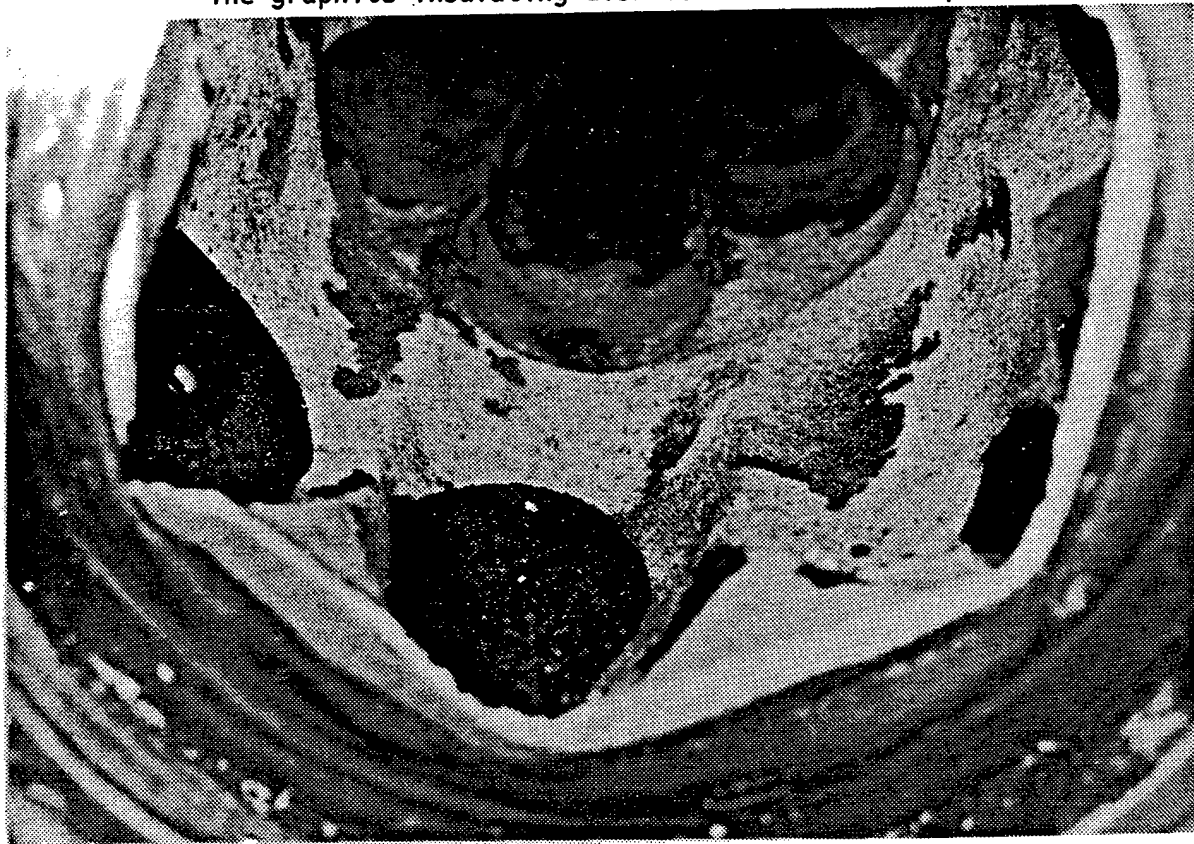


Figure 42. Photograph of Fuel Grain Pockets in First Grain Section Following Run #35

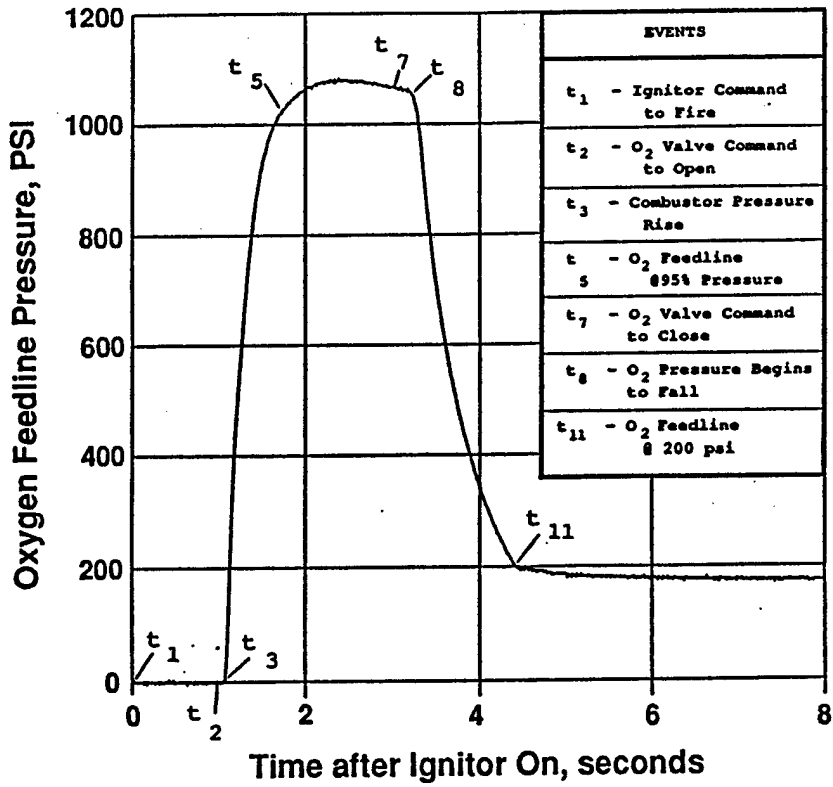
anticipated to be high proved to in fact be minimal. The same nozzle has been used for all tests with an observed throat diameter enlargement of only one mil per run. A second area that was of prior concern was the nonuniformity of fuel burning. It was anticipated that higher burn rates would occur with at the oxygen injection end. This also proved not to be the case. A very uniform burn of the fuel grain along the combustor length was observed after all tests. The burn through on Run #24 and the continual problem at the pressure relief port suggested that presence of free oxygen at these axial locations.

4.3.8 Combustion Data

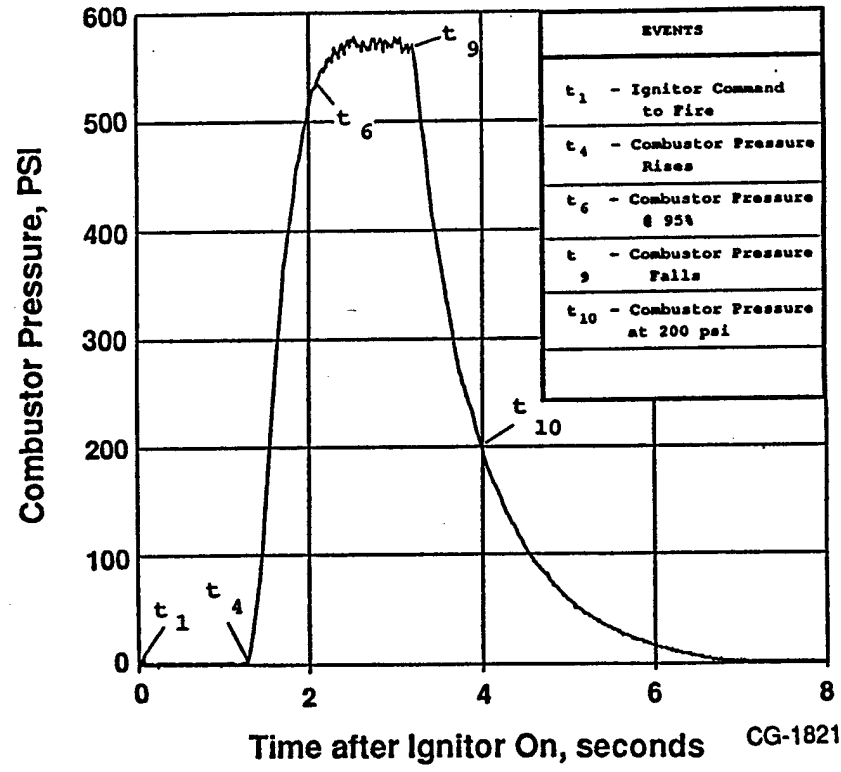
Instrumentation on the combustor was sparse. It included combustor pressure, oxygen feeding pressures, and external thermocouples. Examples of the pressure data are shown in Figure 43. In addition, the oxygen bottles and fuel grains used during the tests were weighed to determine their mass loss and infer flow rates to evaluate the combustion characteristics. Referring to the figures, the combustion is never truly a steady state but rather a transient which has a quasi steady state operating point.

In Figures 43a and 43b various event times can be used as means for comparison for the combustor performance. Such a compilation is shown in Table VII. The events are largely self explanatory with the exception of a few comments. Of the events given in part A of Table VII, events 1, 2, and 5 are preset computer controlled events. All times are referenced to the time at which the igniter command to fire was initiated by the computer controller. A one second delay is used before the command to open oxygen valve to the combustor is initiated. The run duration is programmed in the computer controller. This duration is set to the interval of time between when the oxygen valve is opened and closed. For three of the tests listed in Table VII some combustor pressure data was lost. In test #7, the transducer line was lost when the oxygen manifold failed, in test #24 combustor pressure was lost when the burn through occurred and in Run #28 the signal was lost through a failed wiring contact. A redundant pressure transducer was added after Run #28 for safety.

The combustor transient characteristics are readily discernible from these data. For example, there are relatively consistent delays in opening and closing the oxygen valve, rise time in the combustion pressure, etc. Of particular importance is the time duration for which the combustor is operating at a quasi steady state. This has arbitrarily been defined as the time during which the combustion pressure is greater than 95% of its peak value which is given by duration between events 9 and 6 and given in part B of Table VII as the test time. Combustion within the combustor commences as soon as oxygen is introduced and the average time for the combustor pressure to ramp up to its operating level is 0.92 seconds. Similarly at the termination of combustion, the downward ramp of the combustion pressure requires an average of 0.74 seconds. Adding these average values to the previous test time, the run times given in Table VII B result.



a) Oxygen Feedline Pressure



b) Combustor Pressure

Figure 43. Typical Combustor Pressure Data Showing Event Times.

TABLE VII
Combustor Testing Summary

A. Event Chronology

Time	Event	Run #	Time in Seconds						
			7	10	20	24	28	32	35
t ₁	Igniter command to fire		0	0	0	0	0	0	0
t ₂	O ₂ valve command to open		1.00	1.00	1.00	1.00	1.00	1.00	1.00
t ₃	O ₂ line pressure rises		1.11	1.17	1.06	1.10	1.10	1.08	1.08
t ₄	Combustor pressure rises		1.26	1.29	1.10	1.14	1.18	1.14	1.14
t ₅	O ₂ line @ 95% pressure		1.95	2.00	1.71	2.00	1.90	1.92	1.92
t ₆	Combustor @ 95% pressure		1.98	2.12	2.08	2.15	*	2.12	2.14
t ₇	O ₂ valve command to close		2.38	3.00	3.00	2.50	2.50	2.50	5.00
t ₈	O ₂ line pressure falls		2.38	3.14	3.22	3.18	2.61	2.69	5.10
t ₉	Combustor pressure falls		2.55	3.22	3.30	*	*	2.69	5.22
t ₁₀	Combustor pressure @ 200 psi		*	4.00	4.00	*	*	3.16	6.24
t ₁₁	O ₂ line pressure @ 200 psi		3.35	4.43	4.41	3.67	3.18	3.18	5.67

B. Measured and Derived Parameters

Test time, (t ₉ - t ₆) sec.	.57	1.10	1.22	1.15†	.57†	.57	3.08
Run time, sec.	2.23	2.76	2.88	2.81	2.23	2.23	4.74
Thermal time, ½ (t ₁₀ + t ₉ - t ₆ - t ₄), sec	1.65	1.90	2.06	2.00†	*	1.29	4.09
Peak combustion pressure, psi	633	570	500	537	*	629	617
Peak O ₂ line pressure, psi	1274	1171	1077	1111	1126	1135	1135
Oxygen flow rate kg/sec	1.71	1.57	1.34	1.50	1.58	1.54	1.53
Fuel weight loss, kg	4.20	5.00	3.98	4.34	6.36	5.51	9.51
Fuel flow rate kg/sec	1.88	1.81	1.38	1.54	2.85	2.47	2.00
Oxygen/Fuel ratio	.91	.87	.96	.97	.55	.62	.76
Fuel recession rate cm/sec	.133	.128	.098	.109	.202	.175	.142
Mass flow, kg/sec.	3.59	3.38	2.72	3.04	4.43	4.01	3.53

*Data lost

†Estimated

Similarly, for thermal analysis, the components are subject to heating during the combustor rise and fall as well. A thermal exposure time can be defined as the interval between the midpoints of ramp up and ramp down of combustor pressure and is more comparable with the average run time.

In Table VII, Part B, the oxygen and fuel consumption rates are also given. Of these the oxygen flow rate, calculated on the basis of the measured supply pressure and aerodynamically choked injection nozzles is quite accurate in comparison with the estimated fuel flow rates. In the case of the fuel consumption, the total weight loss of grain divided by an appropriate duration is the only available means of estimating the fuel consumption rate. The fuel flow rates given in Table VII G are based on the indicated weight losses and run times. In this regard they should be viewed as minimal values as the fuel rate may in actuality increase and decrease as combustion rises and falls at the start and end of a test as well. Based on the measured oxygen flow rate, and the indicated fuel consumption rate, the oxygen/fuel ratio, fuel recession rate and mass flow rate can be conservatively estimated. These are given in Table VII, Part B. In comparison with the design values of 1.37, .09 cm/sec and 2.8 kg/sec for the O/F ratio, recession rate and mass flow respectively it is apparent that the fuel consumption is extremely high, of the order of two to three times its design value. Since the design combustion is substoichiometric it can be expected that the excess fuel loss must be in the form of unburnt particulates. Solids in the combustion gases can lower the temperature but they are probably of insufficient loading to alter the gas dynamics and combustion pressure.

Increasing the oxygen flow rate to achieve a more favorable stoichiometry in compensation for the excess rate of fuel grain decomposition was not a viable alternative. To do so would result in increased combustion pressure and correspondingly changed plasma properties throughout the channel and flow train. The only viable methods of reducing the fuel consumption would be to reduce the recession rate by increasing the binder content thereby reducing its rate of decomposition or reducing the fuel grain exposed surface area. It is also interesting to note that the first four runs and the last three runs, as groups, exhibit a marked difference in their recession rates. The fuel was purchased in two lots where the first four runs were conducted with the first lot and the

second lot was used for the final three runs as well. There may have been some differences between the lots or it may just as well be coincidental.

During all runs thermocouples were used to measure outside surface temperatures on the combustor external skin. Three such thermocouples were mounted on the combustor at the oxygen injector plate, the barrel in front of the injector plate and approximately one inch from the pressure relief port on the barrel. The temperature transients measured by these thermocouples for Run #24 are shown in Figure 44. It is noted that for a 2.0 second run the rise in combustor shell temperature is minimal except the vicinity of the pressure relief port. This is the area reported to have blowby of hot gases around the fuel grain during the initial combustor pressurization.

In Figure 45, the combustor temperatures for the longest run, Run #35 are shown and while the temperatures were corresponding higher they remained well within tolerable bounds. As anticipated and pointed out previously the longer duration run had a significant influence on the pocket development in the first section of fuel grain. In the photo in Figure 46 spokes of the fuel grain after the 4 second run are shown. The wear on the spokes in Figure 46 is noted to be quite uniform and substantial. The spoke tops are quite sharply peaked in comparison with the photo in Figure 31 which was for a 1.38 second run.

In the nozzle assembly, three internal thermocouples were installed on the back or outside face of the graphite nozzle block. These thermocouples were axially located 2.5 cm from the entrance, at the throat location and 2.5 cm from the exit. Due to the difficulty of providing lead outs through the pressure vessel these were the only thermocouples mounted interior to the flow train components. By referring to Figure 9, these thermocouples were installed between the graphite and its outer ceramic insulator within the steel nozzle shell. The thermal response of the thermocouples for a typical run is shown in Figure 47 for the three locations. An unexpected behavior occurs in that in certain instances an immediate temperature rise at the onset of combustion is evident. Also, a longer period than anticipated after combustion is seen where the temperature continues to increase. It is believed that the initial temperature rise response may be due to combustion gas leakage through the porous insulator during initial pressurization. The long temperature rise time after firing is the characteristic thermal soak of the nozzle.

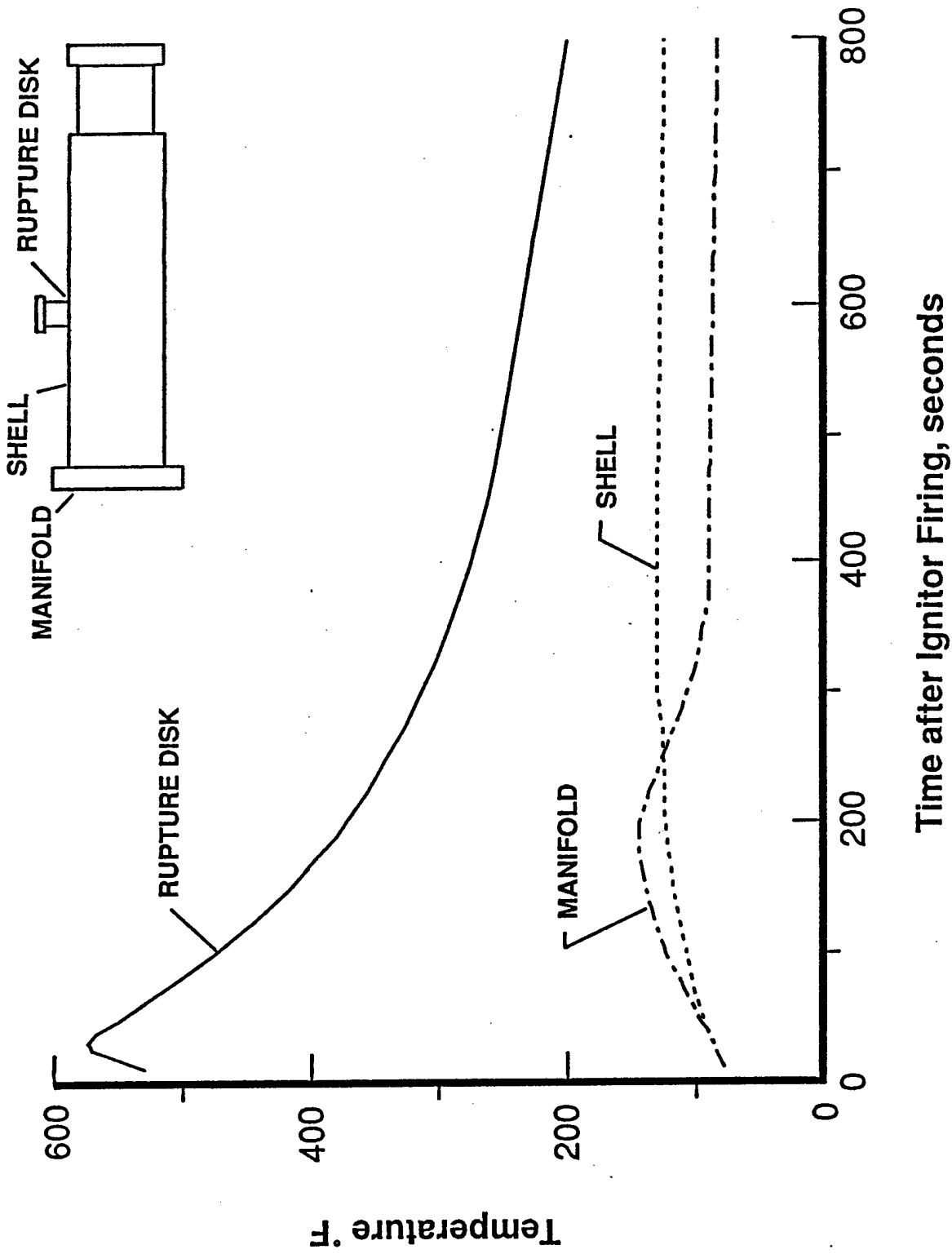


Figure 44. Combustor External Temperatures Following a Nominal 2.0 Second Run.
CG-1815

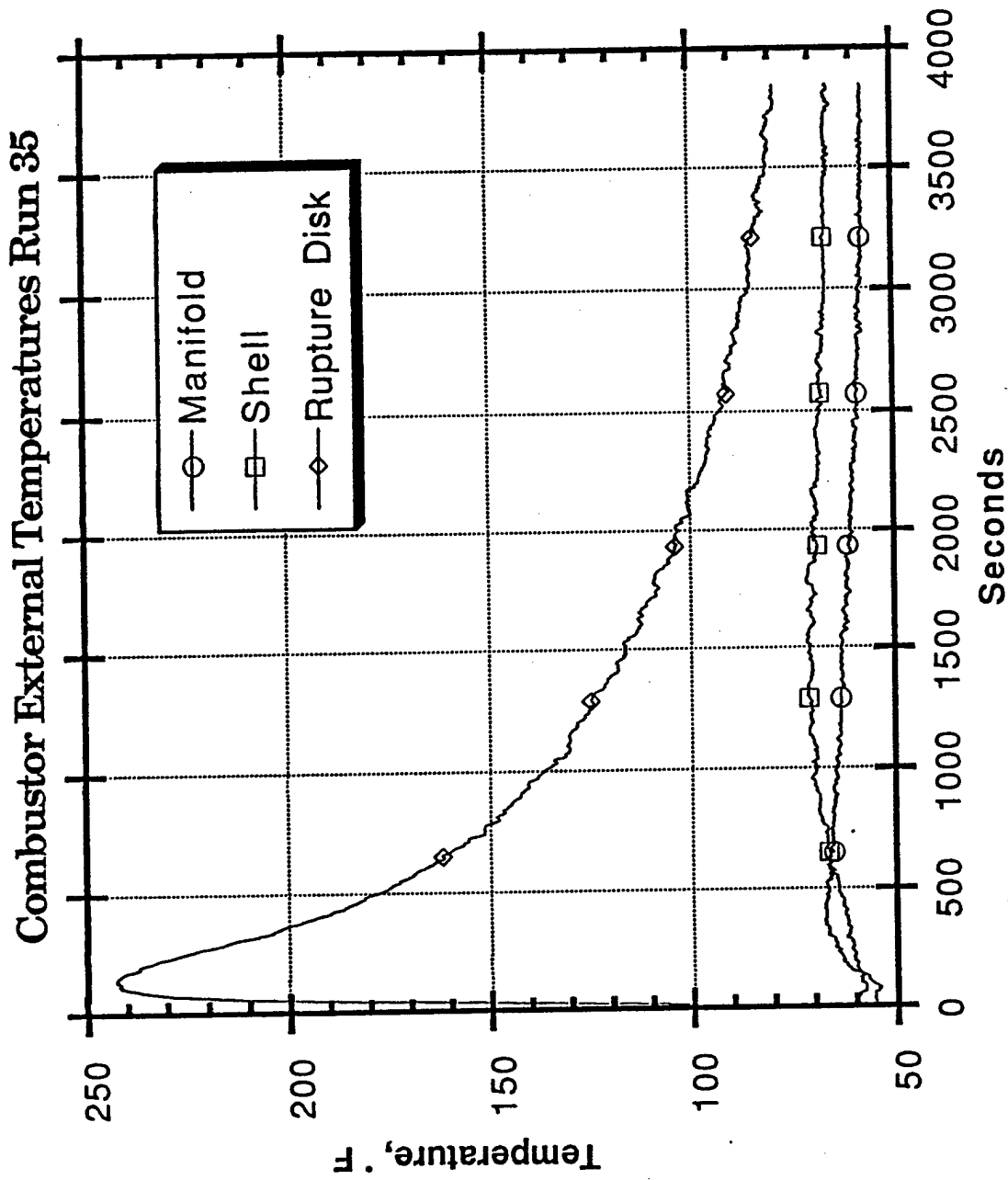


Figure 45. Combustor External Temperatures Following the Extended Duration Run #35.
CG-1814



Figure 46. Photograph Showing Sharply Peaked Fuel Grain Spokes Following Run #35

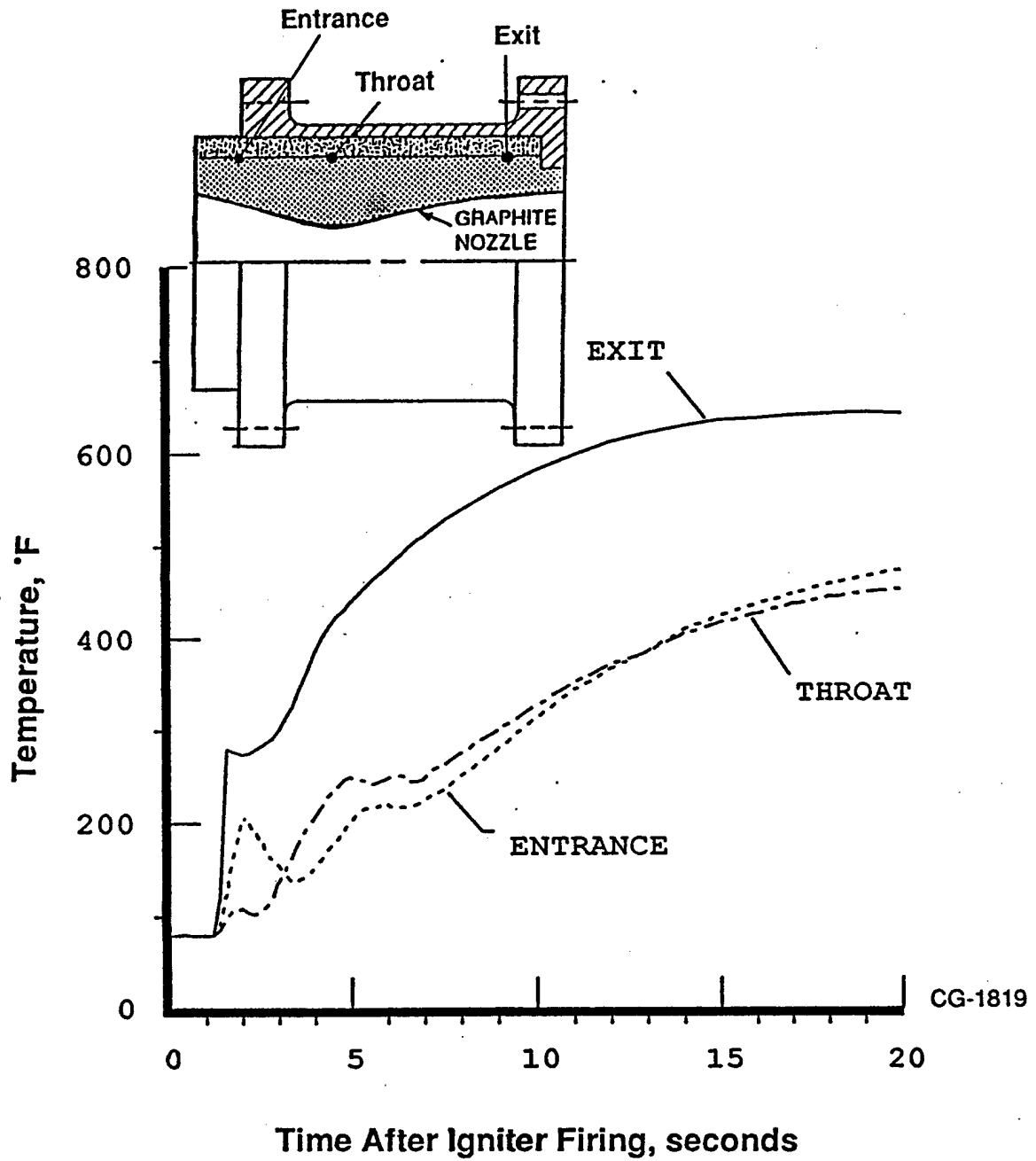


Figure 47. Nozzle Soak Temperature Following a Firing.
(Test Run #10)

4.3.9 Heat Transfer Analysis

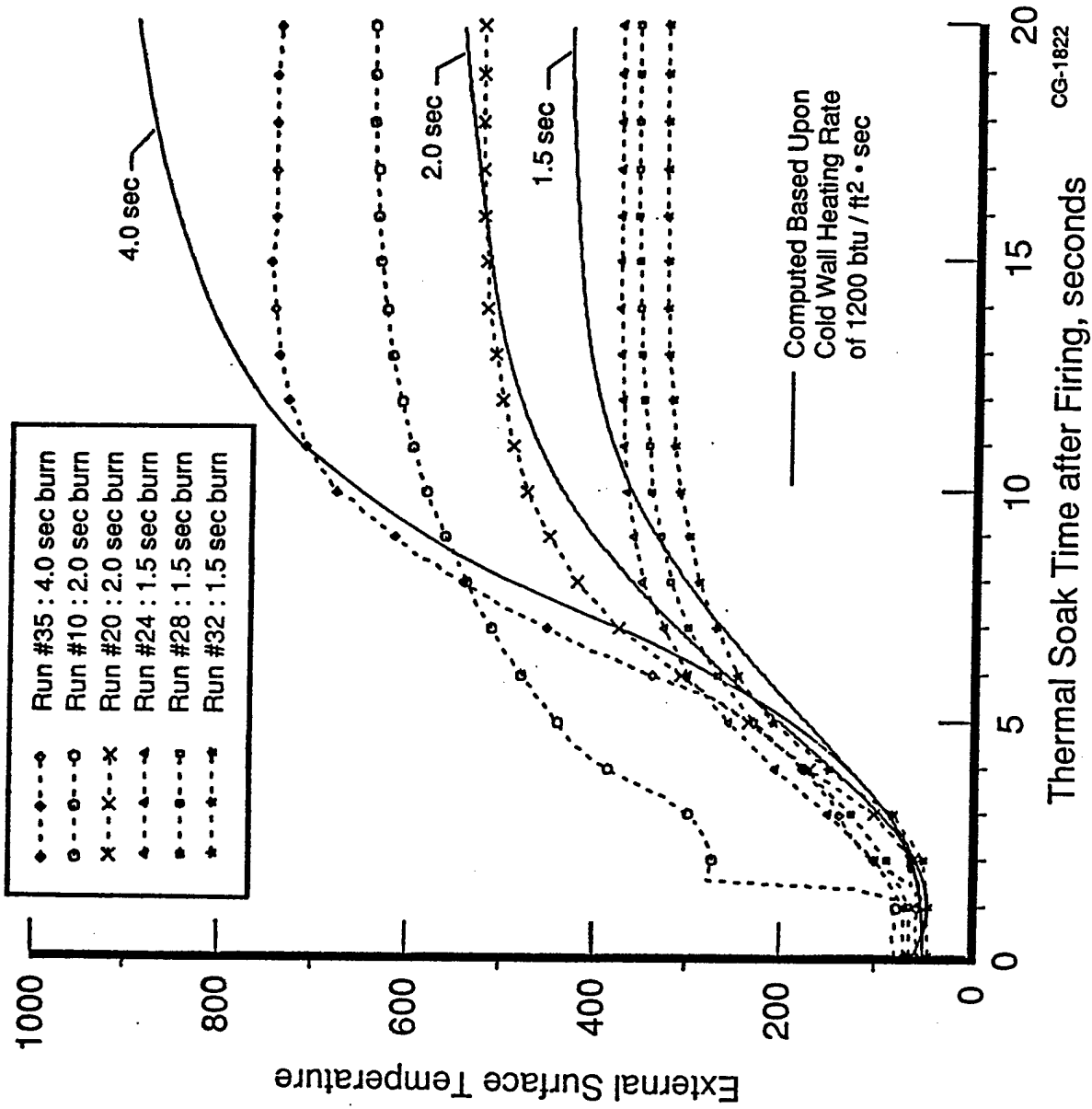
At the end of combustion, nitrogen is introduced to quench the fuel grain and cool the test train. The nitrogen flow rate is approximately 0.27 kg/sec which is about one sixth the oxygen flow. Thus, for a short period following firing the purge cooling is ineffectual. That is, the heat pulse will diffuse through the graphite faster than it can be removed at the inner surface by convection of the nitrogen purge. This fact is evident in the data and appears to be the case for the first twenty seconds.

Analytical calculations can be used to estimate the internal surface temperature of the nozzle at the end of the firing. One such calculation is shown in Figure 48 for a cold wall heating rate of 1200 BTU/ft²-sec. The cold wall heating rate is the initial heat transfer which in the computer model is related to the hot wall heat transfer through the expression

$$q_{hw} = q_{cw} \frac{(T_{rec} - T_w)}{(T_{rec} - T_{w_0})}$$

where q_{hw} and q_{cw} are the hot and cold wall heating rates respectively, T_{rec} is the wall recovery temperature, T_{w_0} is the initial wall temperature and T_w is the transient wall temperature.

This expression models the reduction in heat transfer at the hot surface as its temperature increases assuming a constant convective heat transfer coefficient. In comparing the calculated results with the data it is inferred that the heating rate in the nozzle near its exit location is near 1200 BTU/ft²-sec. For this heating rate, the peak inner surface temperatures predicted by theory are 2324°F for the 1.5 and 2.0 second cases respectively. The results of these transient calculations are to be representative of the actual situation but it is noted that at best this is an approximation since they are based on a one dimensional geometry. Axial conduction during the soak out period has been neglected. In reality, the nozzle is two dimensional and axial temperature gradients will exist.



CG-1822

Figure 48. Comparison of Measured with Theoretical Temperature Transients at the Nozzle Exit Location.

4.4 Magnet Checkout

Prior to committing to generator channel testing the magnet was calibrated using a Gauss meter placed within the bore at the location of peak field strength. The results of this calibration are shown in Figure 49 where the field strength as a function of the excitation current is given. A peak field strength of 2.89 Tesla at an applied voltage of 539 volts with 3.90 kA current was achieved. The magnet as initially built could achieve a peak field of 3.2 Tesla with 3.9 kA current but could not be continuously run at this level due to winding thermal limitations. The magnet has a total of six individual field coils arranged as two pair of saddle coils and one pair of race track coils. During powered MHD tests several years ago one of the saddle coils developed an internal short and this coil has been bypassed from further use. For short durations, the resulting loss in ampere turns could be compensated for by increasing the excitation amperage as long as the winding thermal limitations were not exceeded. It was expected that this could be accomplished and a peak field of 3.2 Tesla could be achieved. As it turned out the problem lies not with the magnet but rather with the current limitations in the magnet power supply. The curve generated and given in Figure 49 was used to infer the magnetic field from the current during tests requiring magnet energization. Three tests using the magnet were conducted and, as indicated in Table VIII, maximum field strengths were achieved in all three tests.

For powered generator testing the magnet was started well before the combustor was fired and it was shut off well after the combustor was shut down. This was done to minimize spurious transients in the instrumentation which can be induced by field changes in the environment of the instrumentation wires. The durations during which the magnet was on as given in Table VIII are correspondingly much longer than the combustor firing durations. The times required to ramp up the magnet at the start of the test and ramp it down at the end of the test were of the order of 20 and 40 seconds respectively. These times as well are long in comparison to the combustor test time and precluded changing the magnetic field strength during any of the generator tests.

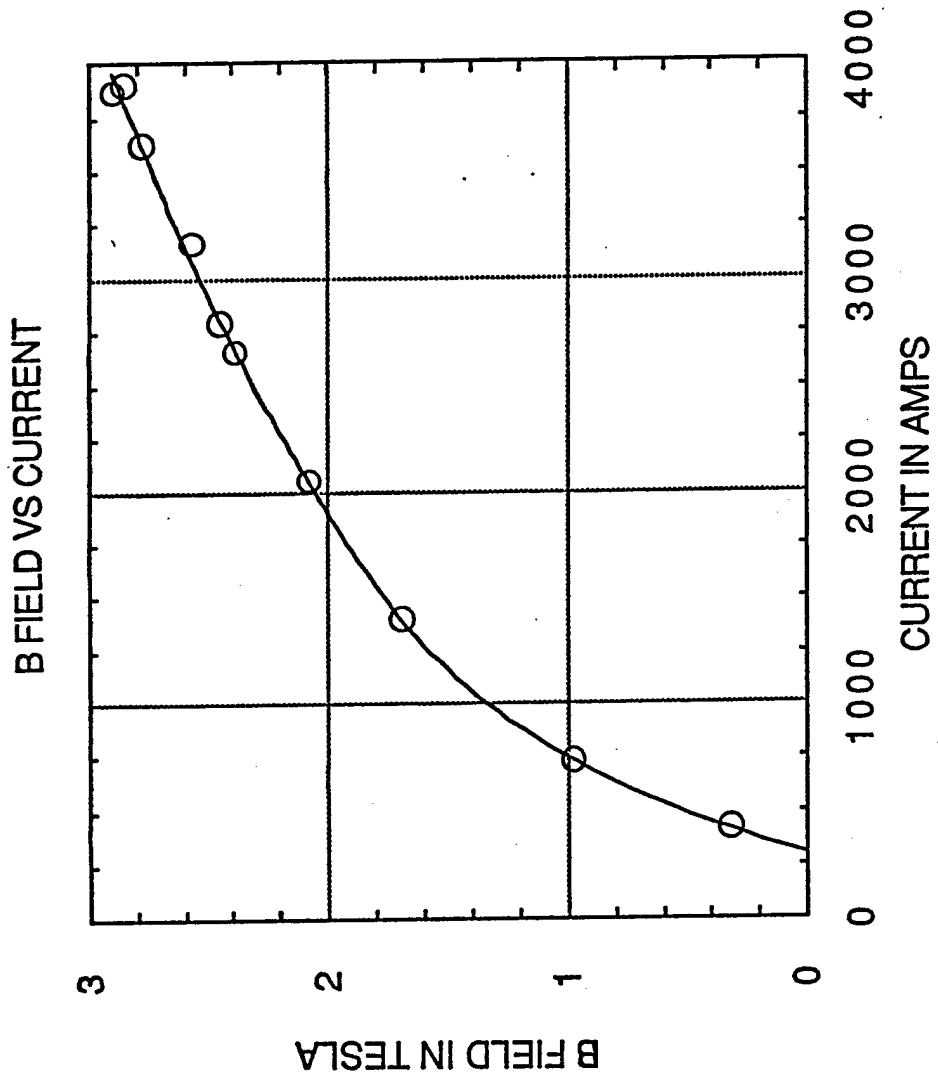


Figure 49. Calibration of CFFF Magnet Giving Field Strength as a Function at Excitation Current.

CG-1816

TABLE VIII. Magnet Field Strengths

Test #	Peak Magnet Current, kA	Peak Field Tesla	Time above 2.8T, sec
#28	3.905	2.89	156
#32	3.940	2.90	141
#35	3.976	2.91	233

4.5 Generator Tests

Four tests were performed with the MHD generator channels installed in the flowtrain. The first test was performed with the Faraday channel in the flowtrain but the magnet halves were separated and no magnetic field was applied. For this test the channel was powered by connecting it to a laboratory power supply. The principal objective of this first test was to proof test the channel construction prior to committing it to the magnet bore. The remaining three tests were power producing tests with one test of the Faraday channel and two tests of the DCW channel. Cumulative run times of 3.0 and 5.5 seconds on the Faraday and DCW channels respectively resulted in the four tests.

All generator testing was performed at the maximum available field strength commensurate with the overall program objective. Since this was the first known time that a combustor was operated within a significant magnetic field environment provision for testing at lower field strengths from 1.0 to 3.0 was planned for in the program should it have been necessary. Similarly at the high interactions anticipated boundary layer separation, particularly in the case of the Faraday channel where high current concentrations could result, could also be alleviated by testing at lower fields if necessary. This as well proved not to be necessary. In the case of the DCW channel its design was predicated on the single high field strength and as such no benefit would be derived from operating it at other than its design value.

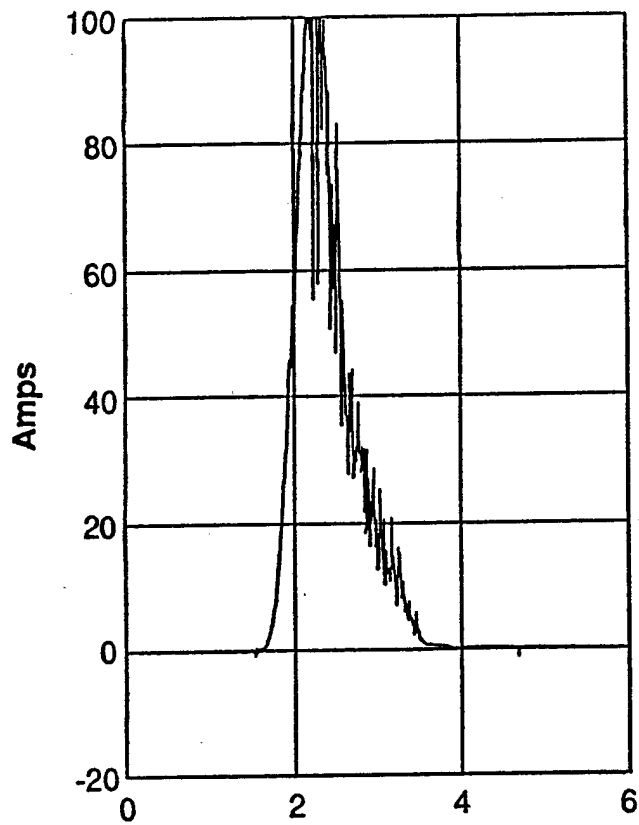
For generator testing the additional instrumentation was comprised of a voltage measurement on the load bank and a current measurement to the load bank. The latter was through a calibrated current shunt and was in effect a voltage measurement as well. The only instrumentation on the channels themselves were outer surface thermocouples

which were used to monitor surface temperatures as a precaution for over heating and resultant thermal damage. Since the power production of the channels was the primary goal of the program the power results from the four tests will be considered individually in the following.

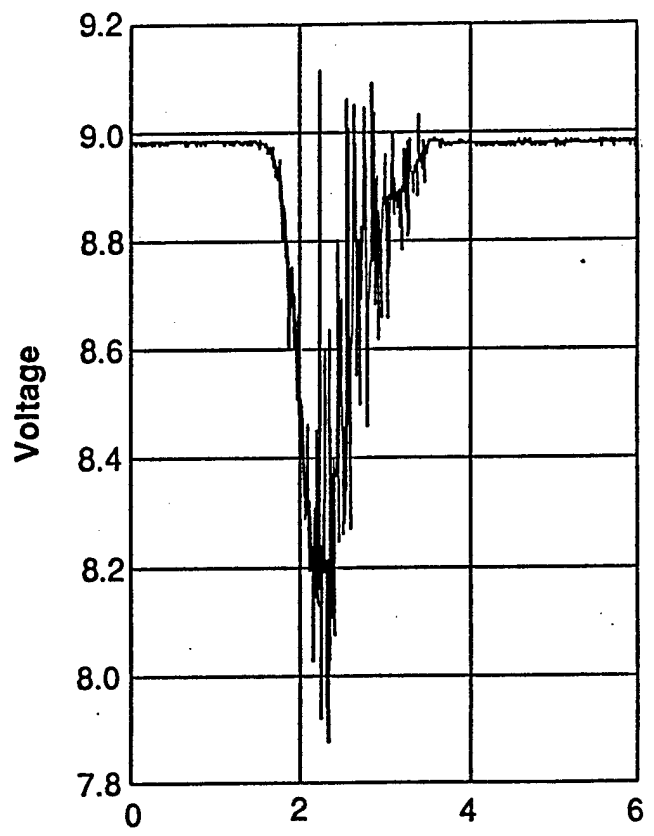
4.5.1 Generator Test #24

This test was performed with the Faraday channel in the flowtrain but with the magnet unpowered and its two halves separated. This test was intended to be a thermal proof test of the channel design. The test ran its intended duration of 1.5 seconds and the channel survivability was demonstrated. Near the end of the run the combustor suffered a burn through as previously described in Section 4.2.

For this test a laboratory power supply was connected to the Faraday channel for an indication of presence of plasma conductivity. That is the laboratory power supply replaced the load bank such that the load bank instrumentation could be used for measuring the applied voltage and resulting current. In essence, the arrangement was to measure the scalar impedance of the generator when the plasma was present. The power supply was current limited to 100 amps and voltage limited to 9 volts. In Figure 50 the resulting current and voltage delivered to the channel during operation are given. Note that as the plasma was introduced the current quickly rose to the 100 amp limitation and the power supply had to switch from voltage regulation to current regulation with a corresponding drop in the applied voltage. At the end of the run the power supply again switched back to voltage regulation. From the results in Figure 50 a peak current of approximately 100 amps at a voltage of 8.2 volts resulted. This would infer that the internal impedance of the generator was 82 milliohms. Recall that the load bank resistance for optimal power output should be the same as the generator internal impedance. The design impedance for the Faraday channel was 31 milliohms as previously given in Table I in Section 3.5. From these resistances one could then infer that the plasma conductivity was less than the design value by the ratio of 31/82 or approximately only 38% of the design value. The validity of such an interpretation, however, is obscured by the unknown electrode voltage drops. The peak occurs early in the run when the electrode surface temperatures should still be rising and the magnitude of applied voltage is very small in comparison to the expected value when operated as a generator. For example, if the voltage drop were in fact 5.1 volts then the



Time, Seconds
a) current



Time, Seconds
b) voltage

Figure 50. Measurement of the Faraday Channel Impedance During Generator Test #24.

CG-1809

design value of conductivity would result. It is equally invalid to assume that the actual drop was 0 volts as it would be to assume it was 5.1 and in reality it was probably somewhere between these limits. As a consequence, what this test showed was the plasma conductivity was unequivocally at least 38% of the theoretical design value.

4.5.2 Generator Test #28

Generator test #28 was performed with the magnet powered and used the Faraday configuration channel. The test ran its intended 1.5 second duration. Post test inspection of the channel revealed it to be in excellent condition with no adverse wear or evidence of arcing. The only noticeable damage was a tapered sliver of boron nitride insulator approximately .125 inch deep and 1" long that was lost at the entrance of the channel. The keystone design of the insulators and graphite electrodes in the Faraday channel suggests that this sliver was broken off as a result of thermal expansion and associated stresses.

Generated power results for this test are shown in Figure 51a, b, c, and d which show the current, voltage power, and power with mathematical smoothing, respectively. The current and voltage traces show considerable noise particularly in the current. In Figure 51a the current reading even shows a reversal prior to the rise in the voltage at the start of the run which is inexplicable. At the start of the run both the current and voltage appear to oscillate about steady values from 1.5 to 2 seconds in the figures. At about 2 seconds the current and voltage both increase in magnitude to the end of combustion at 2.5 seconds. During this run the combustor pressure signal was lost at approximately 1.5 seconds into the run. However, by referring to Table VII it can be noted that the combustor is at 95% of its peak pressure in the time period from 1.98 to 2.15 with regularity. The quasi steady region can then be taken to approximately start of 2.0 seconds in all of the power plots.

The power plot, Figure 51c, is the product of the current and voltage and thus shows noise as well primarily sourced in the current measurement. From the plots the mean peak current, voltage and power are taken to be 2kA, 60 volts and 120kw respectively. These in turn infer the load resistance to be 30 milliohms. The instantaneous peak current, voltage and power from the plots are 2.66kA, 66.5 volts, and 160kw respectively which are not coincident in time and thus incompatible but representative of the approximate noise levels. In Figure 51d the power data is presented

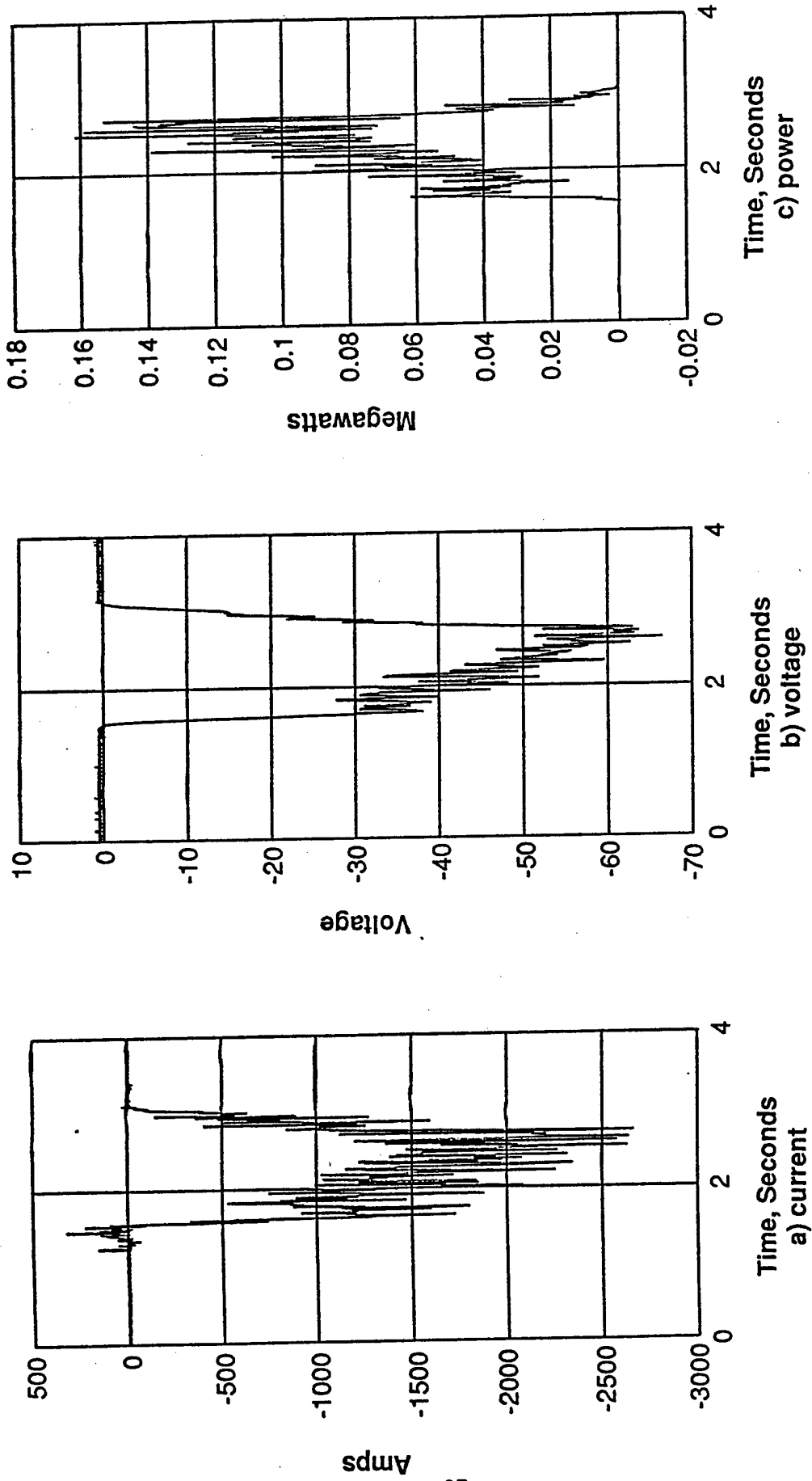
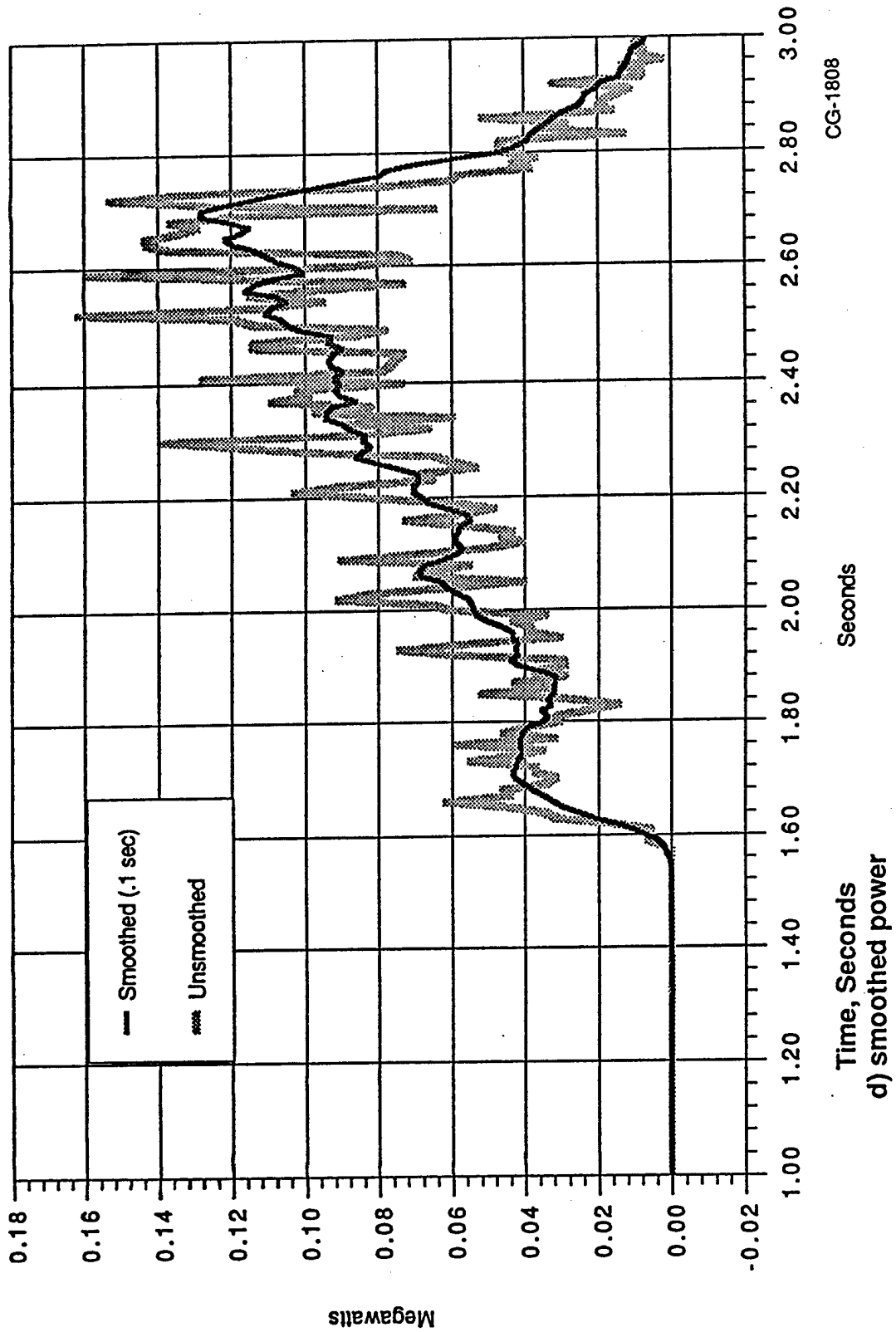


Figure 51. Power Characteristics of the Faraday Generator Channel During Generator Test #28. CG-1808

Faraday Power



CG-1808

Seconds

Time, Seconds

d) smoothed power

Figure 51. Power Characteristics of the Faraday Generator Channel During Generator Test #28. (continued)

after smoothing by 0.1 second interval averaging on an expanded time scale. Clearly the current voltage and power were rising during and at the end of the run.

4.5.3 Generator Test #32

Generator test #32 was the initial magnet powered test of the DCW channel. The test ran its intended 1.5 second duration. Post test visual inspection of the channel revealed no evidence of wear or breakage of internal parts. There was no evidence of arcing as well.

The current, voltage and power results from this test are shown in Figure 52. The plots are quite similar to the Faraday results previously given insofar as noise and apparent termination of the test before achieving peak power is concerned. Again the current noise appears dominant in that oppositely directed currents are recorded before the channel voltage rises at the start of the test. The DCW channel impedance is approximately ten times that of the Faraday channel. The peak mean current, voltage, and power are taken to be 0.75kA, 175 volts and 130kw respectively from Figure 52. These imply a load resistance of 230 milliohms. The maximum indicated values of current, voltage and power are 1.02kA, 226 volts and 229.8kw respectively. These time coincident points also infer a load resistance of 221 milliohms.

4.5.4 Generator Test #35

Generator test #35 was the final test of the program. The DCW channel was tested in a repetition of Test #32 with the test duration extended to 4.0 seconds. Previous tests #28 and 32 both indicated that extending the test duration would result in increased power. These prior tests also suggested that the inner electrode wall temperatures were not getting hot enough thus resulting in voltage drops which were decreasing as the test progressed as a plausible explanation for the observed power results. The test ran its full intended duration and post test visual inspection of the channel revealed it to be in excellent condition again with no evidence of arcing or superficial damage.

The current, voltage and power plots for this run are given in Figure 53. In the figure the pertinent time interval over which the combustor was in a quasi steady operation was from approximately 2.0 seconds to 5.0 seconds. As indicated in the figure the current, voltage and power ramped up initially, similar to the previous test 32 results in Figure 52. The increase in power continued to approximately 3.0 seconds from which

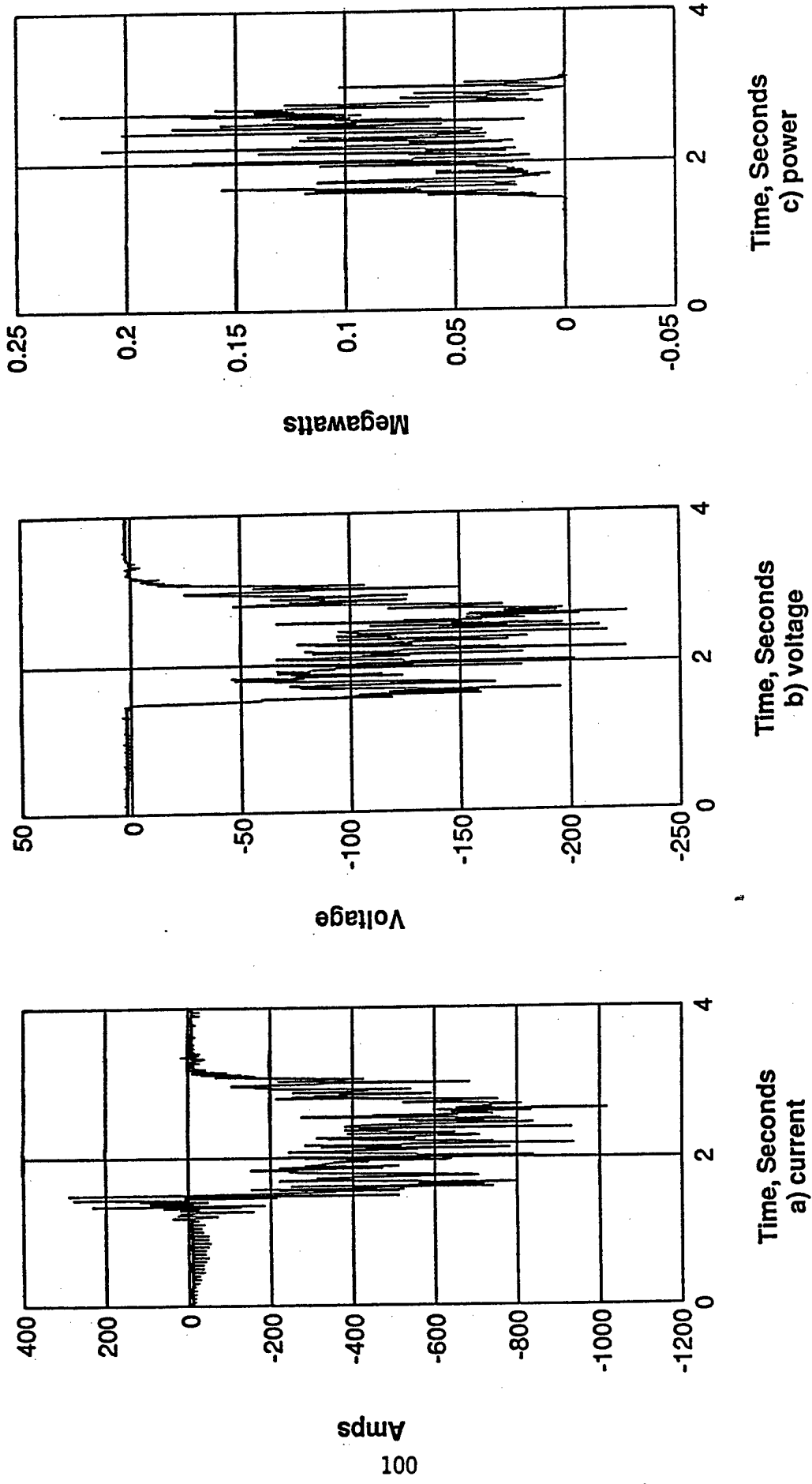


Figure 52. Power Characteristics of the DCW Generator Channel During Generator Test #32. CG-1805

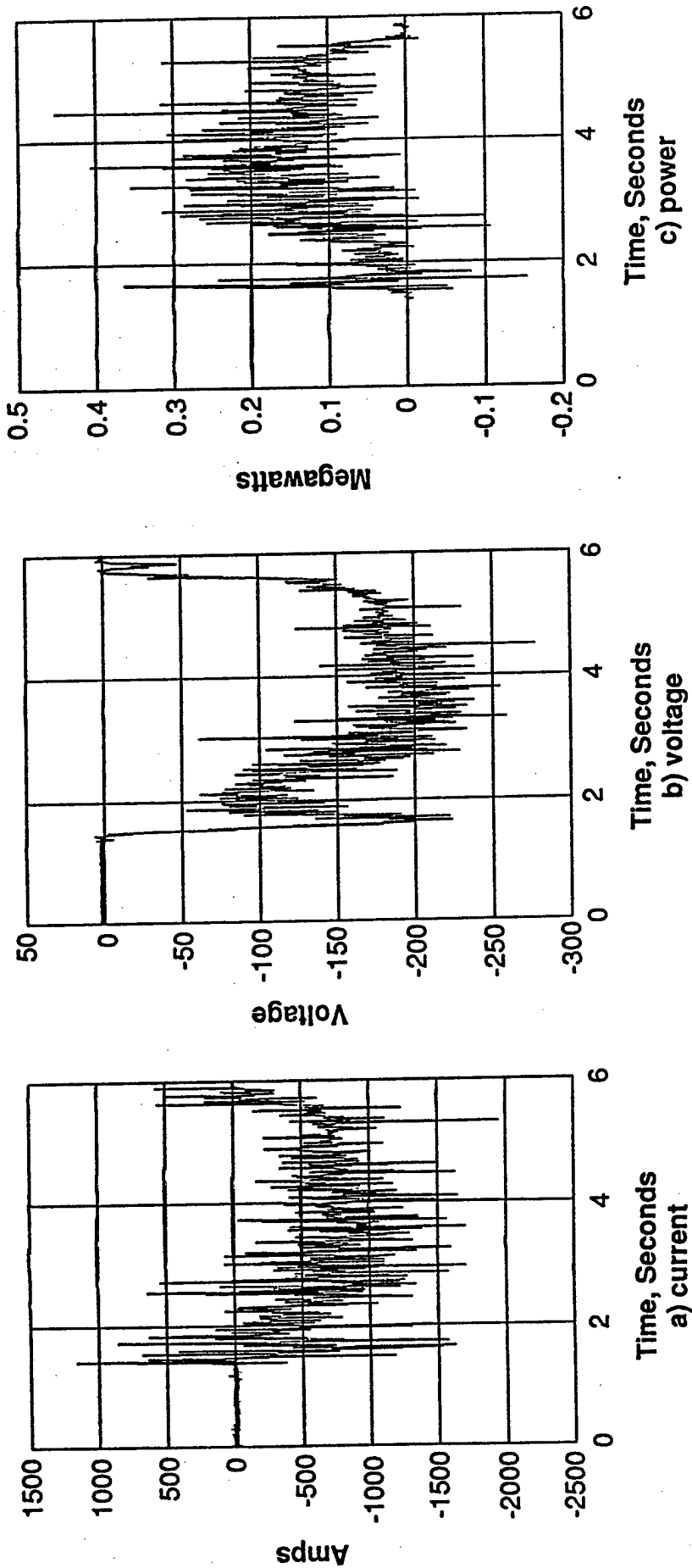


Figure 53. Power Characteristics of the DCW Generator Channel During Extended Duration Run #35.

CG-1806

it appeared to decrease toward the end of the run.

The high speed data for this run was further analyzed and is presented in the histogram plots given in Figures 54-57. In these plots the 2 second window starting at 2.5 seconds into the run was used. In Figure 54 the current data histogram, which gives the number of high speed data points falling within the indicated ranges, is given. The mean current is 950 amps as indicated with the peak value being approximately 1700 amps. In Figure 55 the similar voltage histogram is given and has a mean voltage of 210 volts with peak measured values as high as 285 measured. Again in comparing these plots the scatter in the current data appears to be dominant. That is the current peak value is 79% greater than the mean value while the peak measured voltage is 36% greater than the mean voltage. In Figure 56 the resulting power histogram as obtained from the produce of the time coincident current and voltage measurements is given. The mean power is 200kw which is 70kw greater than the power measured in the shorter duration test #32. Peak powers up to 400kw in the data resulted which is indicative of the current scatter as well. Finally in Figure 57 the load resistance calculated from the time coincident current and voltage measurements is shown. Load resistance should be constant and the indicated mean value of 227 milliohms is in agreement with the measured load resistance of 230 milliohms. As noted, however, considerable scatter is apparent and this scatter is in the high frequency components of the current primarily and to a lesser extent in the voltage data.

The power production parameters for the generator tests are summarized in Table IX and compared to the design values. In the case of the Faraday channel 37% of the expected voltage and 38% of the expected current were achieved which resulted in achieving only 14% of the theoretical design power. In the case of the diagonal conducting wall channel the corresponding percentages were 27%, 34% and 9% for the voltage, current and power respectively.

The observed power deficiency in the tests can result from four conditions. First, the attained magnetic field strength of 2.9 Tesla is 90% of the design value. Since the power is proportional to the square of the field strength this alone would account for a 20% reduction in the generated power. Second, there is insufficient data to determine the electrode voltage drops present in the channel. The extended duration run should have effected a reduction in the voltage drops to the extent possible and certainly longer duration runs in this regard would not be warranted.

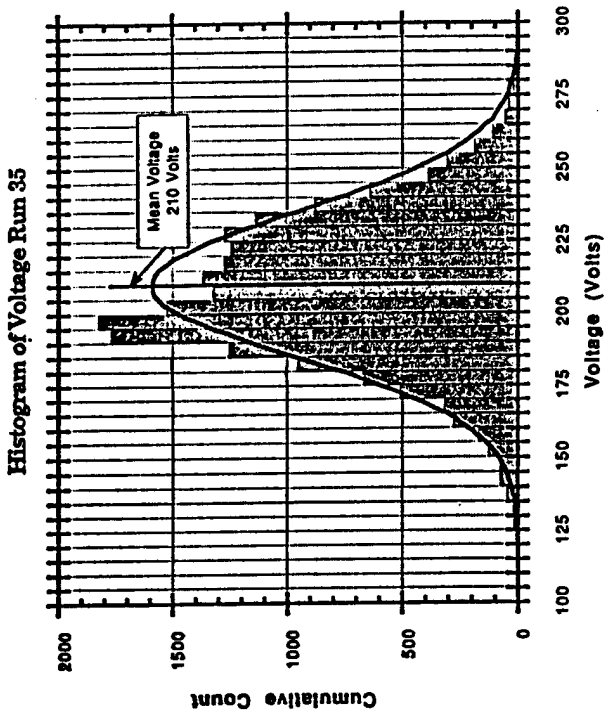


Figure 55. Run #35 Voltage Histogram

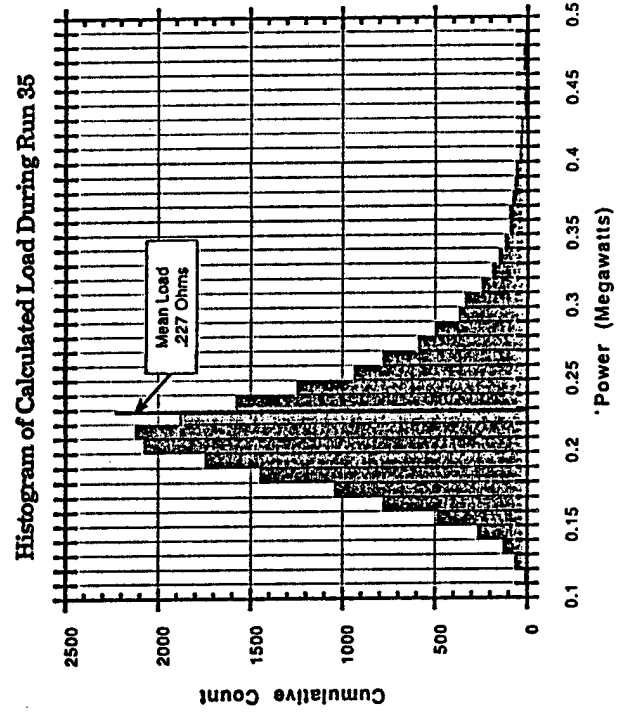


Figure 57. Run #35 Load Resistance Histogram
CG-1807

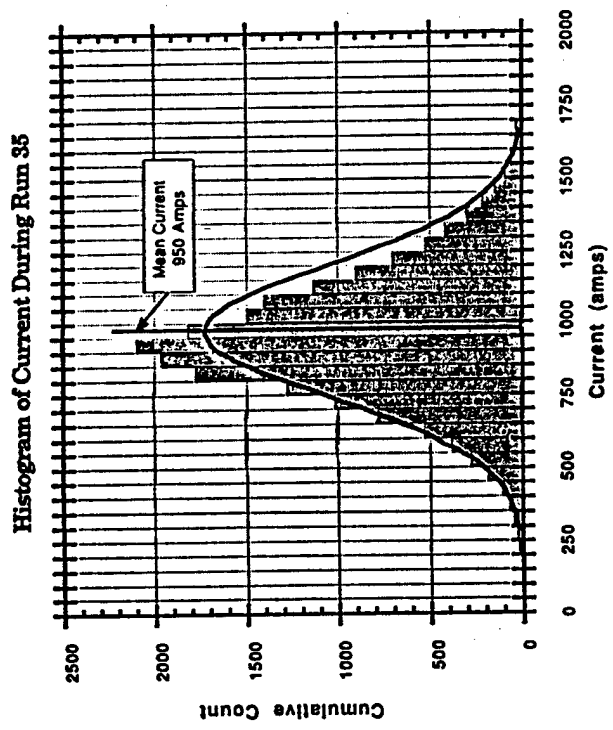


Figure 54. Run #35 Current Histogram

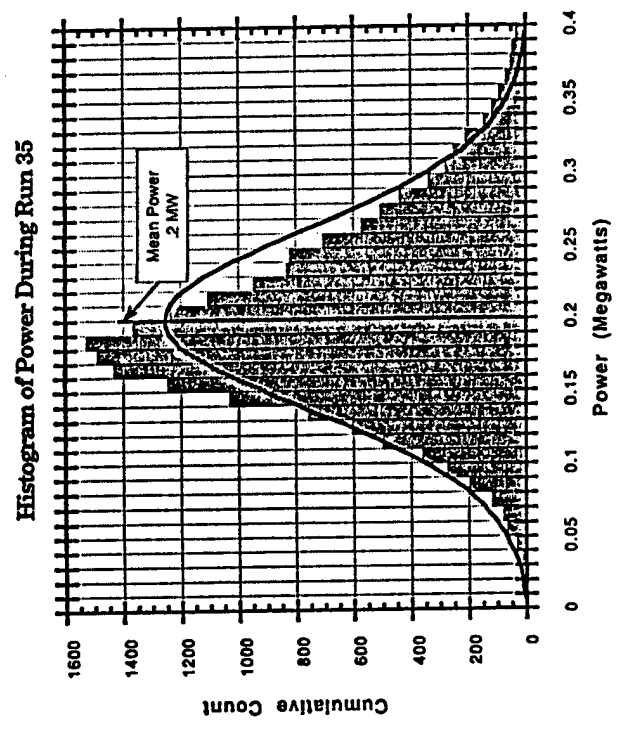


Figure 56. Run #35 Power Histogram

Table IX

**Summary of Generator Performance
(design valves are in parentheses)**

Parameter	Faraday Channel (Run #28)	Diagonal Channel (Run #32) / (Run #35)
Magnetic Field, T	2.9 (3.2)	2.9/2.9 (3.2)
Load Voltage, V	60. (162)	175/210 (787)
Load Resistance, r	.03 (.03)	.23/.23 (.29)
Load Current, KA	2.0 (5.2)	.75/.95 (2.8)
Power, MWe	.12 (.84)	.13/.20 (2.2)
Power Density, MW/m ³	.32 (228)	30/46 (485)

Third, the conductivity of the plasma may be substantially less than the theoretical value. Fourth, if the plasma conductivity is substantially less than the design value, the generator impedance is corresponding greater which means the load bank would not be optimum. For lower than expected plasma conductivity the load bank settings user would be shifted to the short circuit side of the peak performance value.

Throughout all the testing the combustor has consumed fuel at a rate of two to three times its design value. Since the combustion is desired to substoichiometric this has little perceived effect on the combustion. However, the excess decomposed fuel, in the form of solid particulates, may be substantially lowering the resulting combustion temperature and hence conductivity. Figure 58 is a theoretical calculation performed for the excess fuel consumption experienced in the tests. As the figure indicates for excess fuel the conductivity falls off and in fact for the consumption rates experienced the power production should have been zero. Chemical analysis of the fuel grains used in test #32 was also performed. The potassium carbonate content was found to be 13.89% which was less than the design value of 21% required at the design fuel loss rate of 1.18 kg/sec which would yield the desired 5% potassium equivalence at the design total flow rate of 2.8 kg/sec. The desired 5% potassium equivalence in the combustion products can result from the 13.99% potassium carbonate seeding level if the fuel loss rate is 2.84 kg/sec which is 240% of the design rate. This, however, is a somewhat moot point since the resulting plasma temperature in such an event is apparently too reduced to take

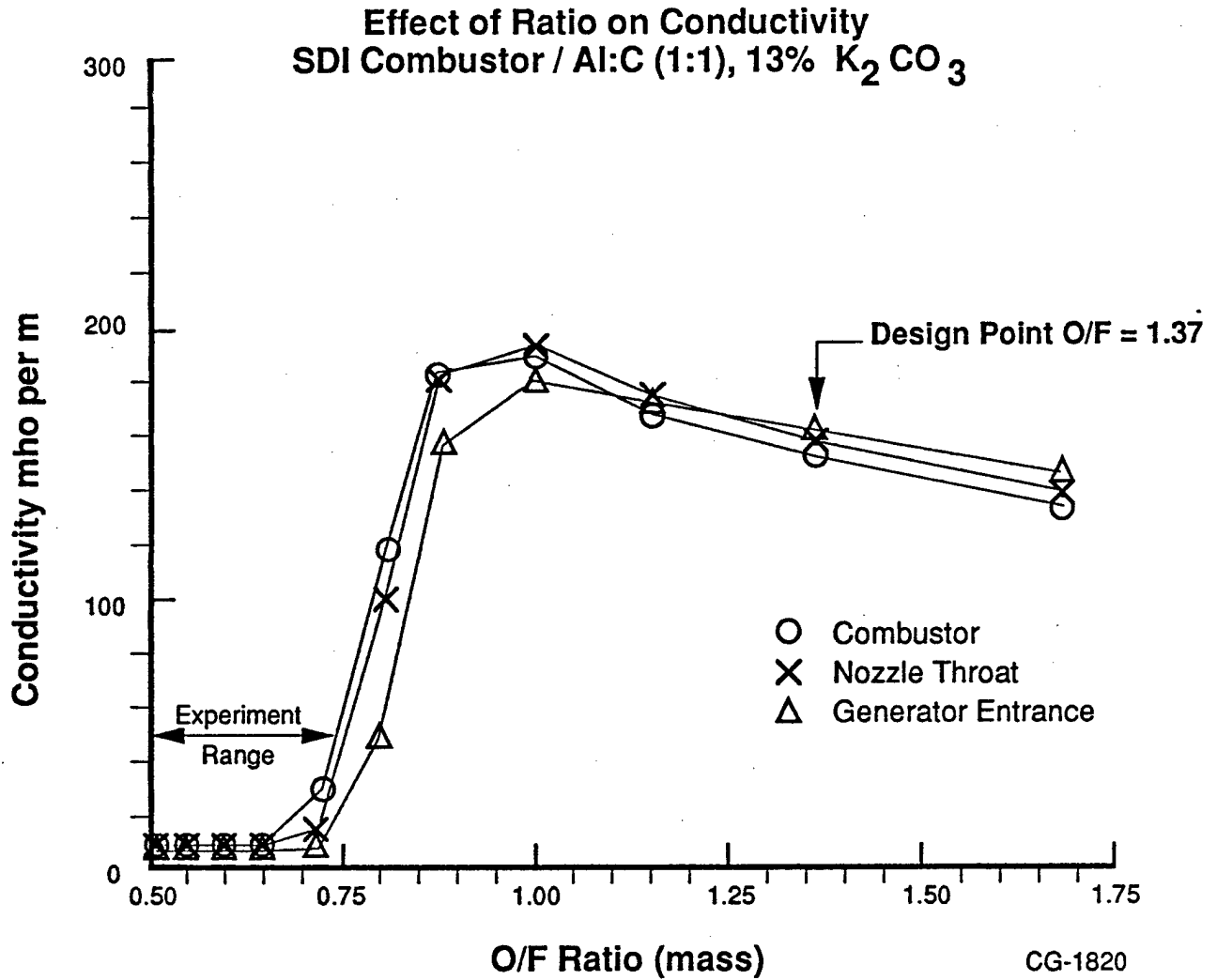
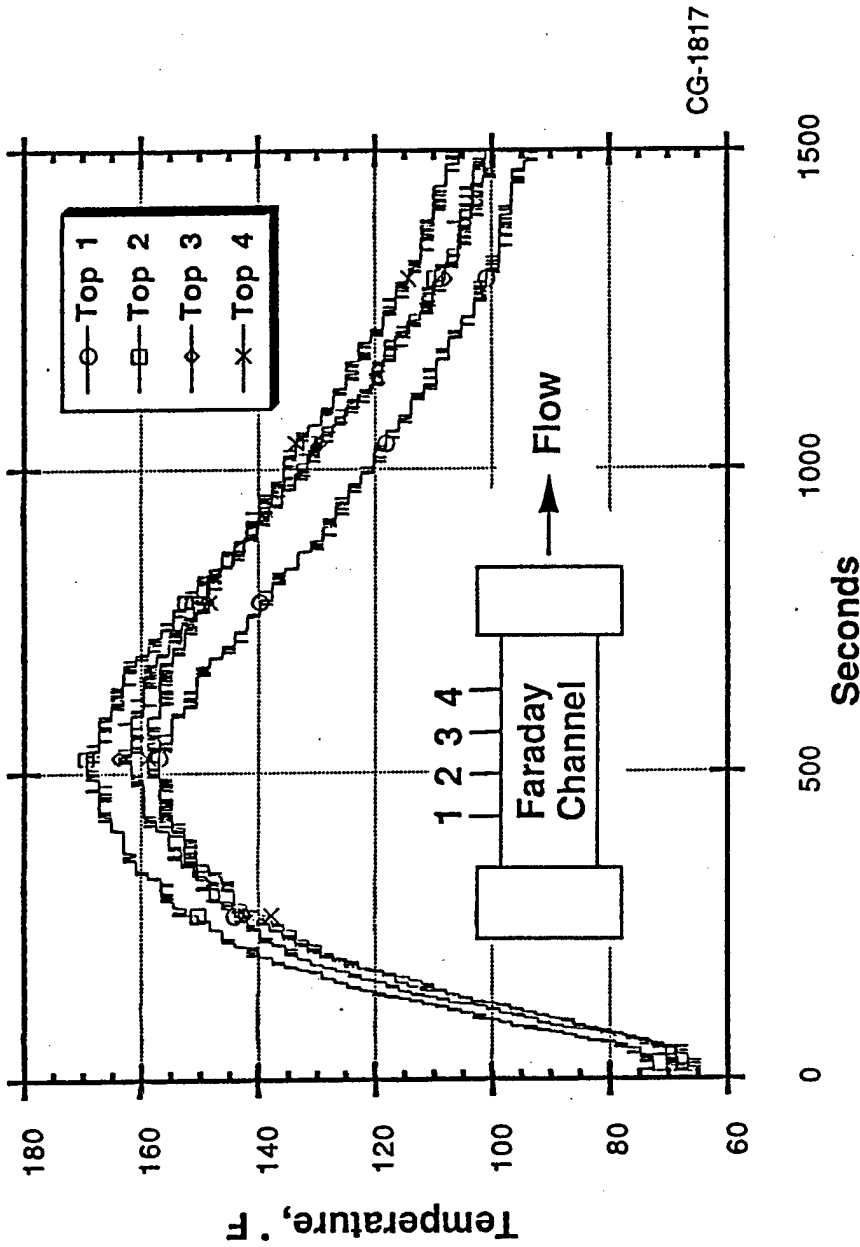


Figure 58 Theoretical Effect of Excess Fuel Consumption on Plasma Conductivity

advantage of it.

Thermocouples were mounted on the outer surface of the generator channels to monitor the thermal soak temperatures. Unlike the thermocouples in the nozzle, the channel thermocouples were separated from the inner graphite electrodes by an insulating layer of epoxy and fiberglass. Since the thermal conductivity of the epoxy and fiberglass is substantially lower than that of the graphite the response of these thermocouples is very long and axial conduction and the small purge flow after the run can not be neglected in analytical modelling. In Figure 59 the outer surface temperatures on the Faraday channel are shown. The five thermocouples were equally spaced between the flanges. There were five on the top, five on the bottom and four on the flanges but for clarity only the top five are shown in the figure. In Figure 60 the surface temperatures for the DCW channel following test #35, the 4.0 second test, are given. It is noted that the peak temperatures occur well after the test is over and the maximum value was 240°F. The epoxy used to pot the interior of the channel was tested and found to have a service limit of 400°F when it cracked, or more appropriately crazed, due to thermal stresses. From the results, it can be concluded that the simple heat sinked channel designs offer a viable alternative for short duration testing.

Channel Temperatures Run 28



CG-1817

Figure 59. Faraday Channel Outer Surface Temperature Following a Nominal 1.5 Second Firing.

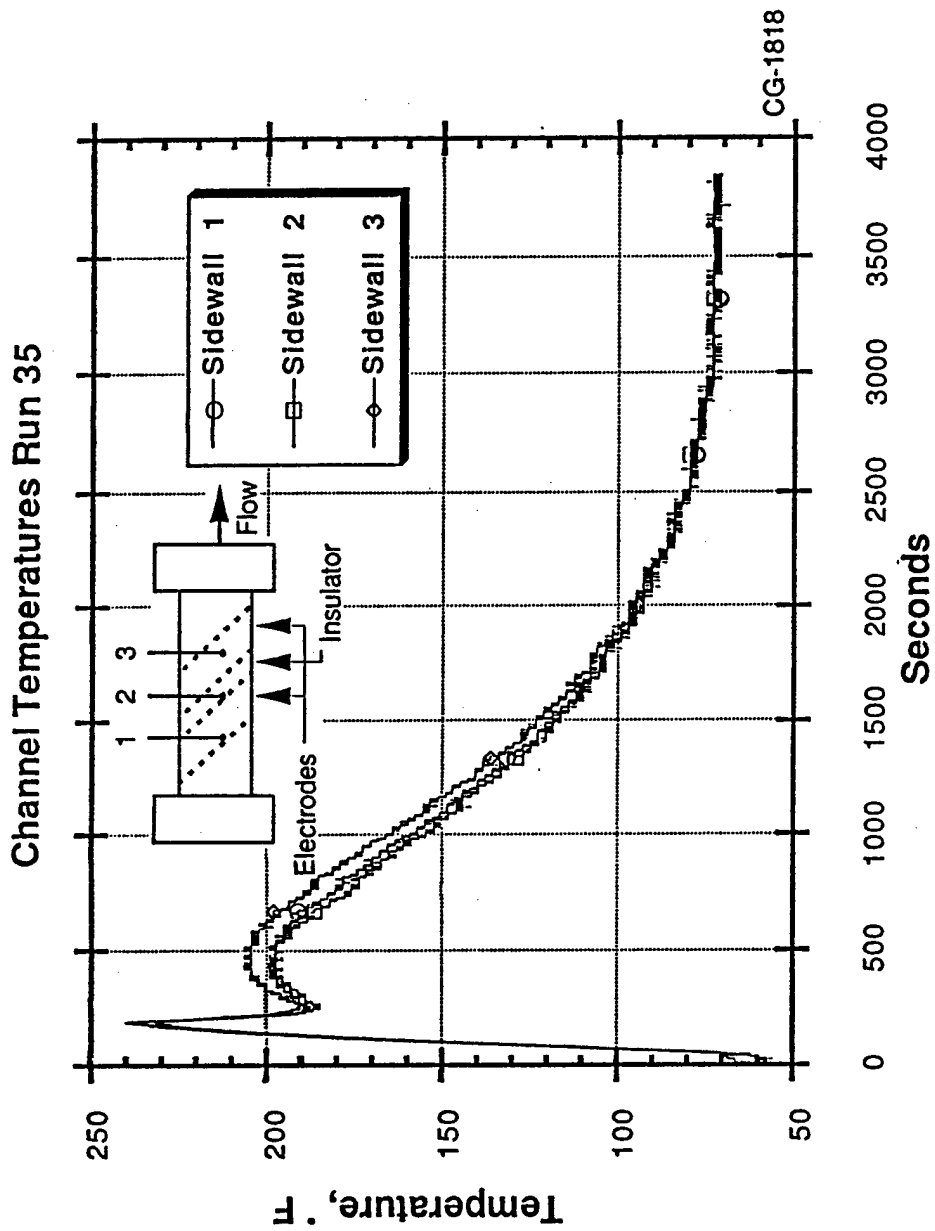


Figure 60. DCW Generator Channel Outer Surface Temperature Following a Nominal 4.0 Second Firing.

5.0 CONCLUSIONS

The program described was conceived as a high risk, low cost effort. It has not achieved its primary goal of demonstrating high power density in a small generator. However, several achievements have been accomplished.

1. An aluminum/carbon solid fuel has been successfully burned in a hybrid combustor and reignition demonstrated.
2. A novel technique for constructing small generator channels has been demonstrated. If a cheaper alternative insulation material can be found to substitute for boron nitride the channels would be relatively inexpensive.

(Note, the cost of the boron nitride was approximately half that for the entire generator channel.)

3. It has been demonstrated that short duration, heat sinked MHD flow trains can be inexpensively constructed.

It can also be concluded that:

1. The aluminum carbon fuel burns quite stably with a quite uniform recession rate.
2. System response times of one second are achievable but for full power longer times to heat the electrodes and lower wall losses may be required.
3. The aluminum/carbon fuel can be burned substoichiometrically with ease.
4. For short run times, the erosion of graphite components of the combustor and channels is insignificant.
5. The probable cause for the power shortfall is a reduced plasma conductivity consequential to excess fuel consumption.
6. Based on the recorded surface temperatures it would be feasible to construct a short duration system completely of fiberglass and graphite.
7. The hybrid combustor using aerodynamically choked injection nozzles is quite safe to operate and a pressure relief port as used on solid propellant rocket motors is not desirable.
8. Locating the combustor within the strong fringe field and bore region of magnet had no perceptible effect on its operation.

6.0 RECOMMENDATIONS

In view of the condition of the hardware after the testing it is recommended that additional testing to address the problem of the power shortfall and excess fuel consumption should be conducted. In such event the following specific recommendations would be applicable.

1. The existing combustor should be used at its present length as a consequence of its compatibility with the geometric constraints of the magnet. In one extended duration test an oscillation of low frequency was observed and the frequency may bear a relationship with the combustor geometry. However, it is equally probably that the oscillation is connected with the fuel grain decomposition which is excessive and of more primary concern of immediate attention. The oscillations were insignificant insofar as structural considerations are concerned.
2. A nitrogen bleed into the region of the pressure port prior to starting combustion should be used to minimize insulator damage consequential to the initial combustor pressurization. Such bleed would terminate as combustor pressure rises through use of a check valve in its supply.
3. Fuel grain sections should be built on site to insure quality control.
4. Off axis inclination of the igniter nozzles should be reduced and a short graphite collar used in the first fuel grain section to eliminate the propensity of pocket formation and extend grain useable life.
5. Of paramount importance, the excessive fuel consumption should be addressed. The simplest approach would be to reduce the exposed area of the grain. This could be accomplished by using dummy cylindrical (annular and unspoked) graphite sections at the nozzle end of the combustor. Removal of the spokes as a means for reducing the exposed area is not recommended. An alternative of varying the binder content to reduce the recession rate would be more beneficial in the long term as it would extend the duration for utility of a fuel load. This approach would require further detailed investigation of the fuel characteristics which was not in the scope of the present program.
6. Generator testing should be made with differing load resistances to establish the generator loadline. Tests of 3 seconds duration appear to be adequate for this purpose.

7.0 REFERENCES

1. Aleshin, M.H., et al, "Generator of Plasma on the Powder-Like Fuel of the Pulse Geophysical Installation," Proceedings of the 8th International Conference on MHD Electrical Power Generation, Moscow, 1983.
2. Volkov, Y.M., et al, "Investigation of Electrophysical Characteristics of the Combustion Products of the Metallized Powder-Like Carbon Fuels," Proceedings of the 8th International Conference on MHD Electrical Power Generation, Moscow, 1983.
3. Lineberry, J.T., Schmidt, H.J., Chapman, J.N., "Semi-Annual Report for An Innovative Demonstration of High Power Density in a Compact MHD Generator," University of Tennessee Space Institute, May 1988.
4. Crawford, L.W. and Lineberry, J.T., "Factors Affecting MHD Power Generation Using Powdered Aluminized Fuels," AIAA-86-1066, 4th Fluid Mechanics, Plasmadynamics Conference, Atlanta, GA, May 1986.